Liquid-film Coating on Rotating Discrete Objects

A THESIS
SUBMITTED TO THE FACULTY OF THE GRADUATE SCHOOL
OF THE UNIVERSITY OF MINNESOTA
BY

Weihua Li

IN PARTIAL FULFILLMENT OF THE REQUIREMENTS
FOR THE DEGREE OF
DOCTOR OF PHILOSOPHY IN MATERIALS SCIENCE AND ENGINEERING

Satish Kumar

January, 2018

Acknowledgements

There are many people that have earned my gratitude for their contributions to my time in graduate school. I would first like to thank my graduate research advisor Professor Satish Kumar, for his continuous support of my Ph.D research, for his patience, motivation, enthusiasm, and immense knowledge. He not only taught me how to do research, but also how to be a more organized person. I would have achieved nothing without him.

I was also fortunate to work with exceptional colleagues in my research group. Dr. Eric Vandre, Dr. Aruna Ramkrishnan, Dr. Akhilesh Sahu, Dr. Andrew Corbett, Dr. Chen-Yu Liu, Dr. Leonardo Espín, Chung-Hsuan Huang, Truong Pham, Gokul Hariharan, Jyun-Ting Wu, Chance Parrish, Panayiotis Kolliopoulos, and Vasileios Charitatos have at different times been much-appreciated sources of insights as well as enjoyable distraction.

My work was funded through the Industrial Partnership for Research in Interfacial Materials and Engineering (IPRIME program) at the University of Minnesota. I have been fortunate to actively participate in the Coatings Process Fundamentals Program (CPFP) and IPRIME for more than five years, through which I gained useful feedback and inputs from both academia and industry to direct my research. I am also grateful for resources from the University of Minnesota Supercomputing Institute, which I used throughout my doctoral work.

Finally, I would like to thank my friends and family for all of their support. Although I only had the chance to go back to China twice in the past five years, my parents, Yan Xie and Jian Li, were always supporting me spiritually and encouraging me with their best wishes. My wife, Sun Zu, was always there cheering me up and stood by me through the good times and bad and I am very excited for our times ahead. My dear

friends, Tianqi Wang and Tuoqi Li, made me miss home less and made my stay in the university fun and memorable. I am incredibly blessed to have such wonderful people in my life.

Abstract

The flow of liquid films on discrete objects is encountered in coating processes for a wide range of products such as biomedical devices, automobiles, and food. Describing the shape of liquid films as they flow over discrete objects is a challenging task due to the large number of forces at play. These include gravitational, inertial, viscous, surface-tension, and centrifugal forces, and the complex interplay among them may lead to the growth of instabilities that degrade the quality of the final product.

Motivated by the need to improve fundamental understanding of coating flows on discrete objects, we pick cylinders that rotate about their horizontal axes as model discrete objects and investigate four model problems highly relevant to industrial coating processes for rotating discrete objects. In each model problem, the interplay among all the forces is systematically examined to reveal the critical conditions for which a smooth coating can be obtained.

For coating of surfactant-laden liquids on rotating cylinders, we applied lubrication theory to derive coupled nonlinear evolution equations to describe the variation of the film thickness and surfactant concentration as a function of time, the angular coordinate, and the axial coordinate. In the absence of gravitational effects, linear stability analysis reveals that surfactant-induced Marangoni stresses suppress the growth rate of instabilities driven by centrifugal effects and hinder the leveling of perturbations to the film thickness in both the angular and axial directions.

When gravitational effects are present, Marangoni stresses lower the critical rotation rate needed to cause a liquid lobe to form and rotate in the angular direction. These stresses also lead to faster damping of this lobe, giving rise to a more axisymmetric coating. With the growth of axial instabilities at long times, Marangoni stresses significantly weaken the stabilizing effect of surface-tension forces, which are found to be responsible for keeping the coating axially uniform in a stable speed window. In addition, Marangoni stresses tend to reduce the spacing between droplets that form at low rotation rates, and suppress the growth rate of rings that form at high rotation grates. Flow visualization experiments yield observations that are qualitatively consistent with our simulation results.

For cylinders with complex surface geometries (i.e., topographically patterned cylinders and elliptical cylinders), the Galerkin finite-element method is used to solve the Stokes equations, augmented with a term accounting for centrifugal forces, in a rotating frame of reference. For rapidly rotating cylinders where gravitational forces are negligible, surface-tension forces tend to drive liquid to the low-surface-curvature areas (e.g., pattern troughs) leading to the formation of liquid pools, while centrifugal forces tend to drive liquid in the opposite direction, giving rise to liquid droplets. The number of droplets or pools at steady state depends on the rotation rate, strength of surface tension, pattern frequency, and cylinder aspect ratio.

When gravitational forces become significant, it is possible to obtain a coating that closely conforms to the cylinder surface in the patterned-cylinder case. With an increase in the pattern amplitude, recirculation regions start to form inside the troughs, which may strongly influence mixing, mass transport, and heat transport. These reciprocation regions can appear and vanish as the cylinder rotates due to the variation of gravitational forces around the cylinder surface. In the elliptical-cylinder case, simulation results show that smaller aspect ratio corresponds to less liquid that can be supported on the cylinder and also larger gradients in film thickness. A suitably chosen time-dependent rotation rate can greatly improve coating smoothness relative to the constant-rotation-rate case. For cylinders with sufficiently small aspect ratio, film rupture and liquid shedding may occur over the cylinder tips, so simultaneous drying and rotation along with the introduction of Marangoni stresses will likely be especially important for obtaining a smooth coating.

Contents

List of Tables

List of Figures

Chapter 1

Introduction

In a typical coating process, one or several liquid layers are deposited on a substrate (Fig. 1.1a) and are then dried to form solid films that serve specific functions. Examples of these functions include protecting the surface of the substrate from corrosion or abrasion (e.g. coating on boats), eliminating reflections of light (e.g. coating eyeglasses), and also controlling the wettability of solid surfaces (e.g. coating vehicle windshields).

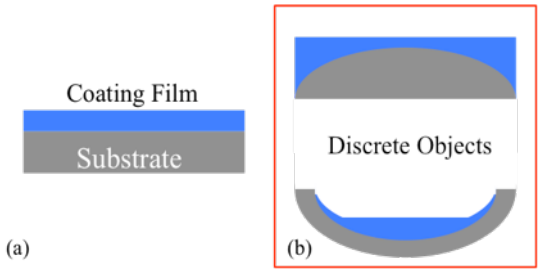

Figure 1.1: Liquid coating on (a) planar substrate and (b) non-flat substrate

For most of the coating products, film thickness needs to lie within a specified range for the product to exhibit the desired properties. For example, a thickness fluctuation that is greater than 5 μm in the color photographic film may result in a magnified flaw in the final projected image [1], while the tolerance for thickness fluctuation in the manufacturing of solar cells is only several tens of nanometres to ensure the solar cell efficiency [2]. Growing demands on thickness uniformity, as well as productivity and yield of the coating processes, requires a sound and basic understanding of flows over

the substrates before they are solidified. For this reason, these flows have attracted considerable attention in the literature [3]. Previous works in this area have focused primarily on the fluid dynamics on planar substrates due to their geometric simplicity, while still very little is known about the fundamentals of coating flows on objects with non-flat surfaces.

The flow of a thin liquid film on a discrete object is commonly encountered in coating processes for products including biomedical devices (contact lenses, stents), food (cereal, chocolate), and automobiles. Relative to the planar substrate case, obtaining a uniform coating on a highly curved substrate is a more challenging task. As shown in figure 1.1b, while substrates create coating shapes that are impressions of substrate shapes, the liquid-air interface tends to be flattened by interfacial tension, leading to a nonuniform coating.

One way to improve coating uniformity on a discrete object is by rotating the object. For example, if we dip a knife in a viscous liquid, such as honey or syrup, and then hold the knife horizontally, the liquid tends to drain off due to gravity. Our intuition suggests that more liquid can be made to remain on the knife by simply rotating it, which then gives rise to a more uniform "coating" on the knife, relative to the stationary case. This rotation effect has already been exploited in many practical coating processes for various purposes, and examples are given in Fig. 1.2.

A typical coating process can often be separated into three stages (Fig. 1.2). At the first stage, coating liquid is deposited onto a curved substrate through a curtain flow [4, 5], spay drops [6, 7], or a solution bath [8]. The object to be coated is then rotated to get ride of excess liquid [5], to redistribute liquid around the circumference of the object [8], or to create a specific pattern on the substrate [4], before the coating is dried to form a solid film at the final stage. The flow of thin liquid films in the second stage is susceptible to numerous disturbances [9], including concentration gradients in coating additives, uneven substrate thickness, and also thickness variation along the length of the objects, which often lead to failure of the process to deposit a uniform liquid layer. Due to the lack of knowledge about the mechanism involved in these phenomena, it is difficult to design and optimize the coating processes for discrete objects.

Motivated by this gap in fundamental knowledge, my thesis project involves the investigation of four model problems highly relevant to industrial coating processes for

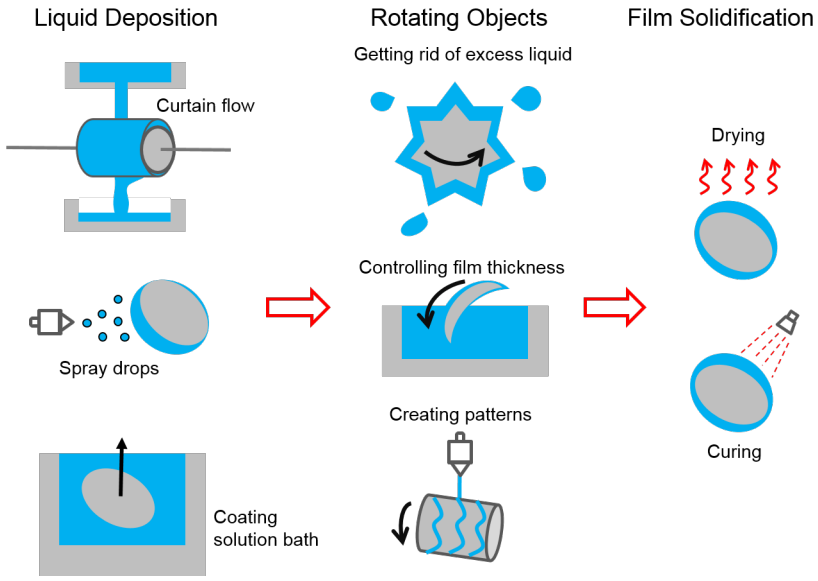

Figure 1.2: Typical processes for coating of discrete objects.

rotating discrete objects. Cylinders that rotate about their horizontal axes are chosen as model discrete objects due to their geometric simplicity. A combination of theoretical modelling and experiments are used to investigate the influence of surfactants (Chapter 2, 3), surface topography (Chapter 4), and non-circular cross sections (Chapter 5) on the flow of liquid films around rotating cylinders.

1.1 Background

1.1.1 Flows of Thin-Liquid Film on Rotating Cylinders

When a cylinder is coated with a liquid film, the film will tend to sag under the action of gravity, and would simply drain away in the absence of surface tension and cylinder rotation. Moffatt [9] discovered that by invoking the lubrication approximation and neglecting surface tension, inertia, and axial variations in the film thickness, it is possible to obtain an analytical expression for the maximum amount of liquid that can be supported when the cylinder rotates. In terms of a critical rotation rate Ω_c needed to

support a liquid film of mean thickness H, the condition is [10]

$$\Omega_c = \left(\frac{2\pi}{4.443}\right)^2 \left(\frac{H}{R}\right)^2 \frac{\rho g R}{\mu}. \tag{1.1}$$

Here, R is the cylinder radius, ρ is the liquid density, g is the magnitude of the gravitational acceleration, and μ is the liquid viscosity. When $\Omega > \Omega_c$, the liquid film is thicker on the upward-moving side and thinner on the downward-moving side. Such so-called Moffatt-type steady-state solutions or smooth coatings are unique for a given rotation rate [11].

When $\Omega < \Omega_c$, a solution can only be obtained when surface tension is restored [10]. This was discussed in detail by Evans *et al.*, who used lubrication theory to derive a nonlinear evolution equation for the film thickness which was then solved numerically [10]. In this case, a drop-like liquid bulge forms on the underside of the cylinder, and rises higher on the upward-moving side as the rotation rate approaches the critical value. The significant effects of surface tension are confined to the vicinity of the liquid bulge, where large changes in film thickness occur. Experimental investigations of the critical rotation rate have been undertaken by Kelmanson [12] and Preziosi and Joseph [13], and their results are in reasonable agreement with Moffatt's criterion.

Many other studies have also explored various aspects of thin-film flows on rotating cylinders. Kelmanson [12] proposed a refinement to Moffatt's criterion that selectively retains some higher-order terms and pointed out that Moffatt's criterion increasingly overestimates the critical rotation rate with a increase in the amount of liquid deposited onto the cylinder. Peterson *et al.*[14] used an adaptive finite-element scheme to solve the free-boundary problem involving the full Stokes equations, which allows them to overcome the restriction that film thickness needs to be much smaller than the cylinder radius. Their results reveal that the lubrication approximation works quite well even when the film thickness is a significant fraction (40%) of the cylinder radius. Campanella and Cerro [17] considered the case where the cylinder is partially submerged in a bath of liquid and Duffy and Wilson [18] considered the case where fluid is supplied continuously on to the cylinder as a 'curtain' from above. In both cases, a smooth coating can be obtained for all values of cylinder rotation rate. This thesis extends the works of Moffatt [9] and Evans *et al.* [10] to account for the influence of axial flows, surfactants, surface topography, and non-circular cross sections.

1.1.2 Axial Instabilities

In all of the works mentioned above, axial variation of the coating thickness are neglected to simplify the governing equations. However, flow along the axis of the cylinder triggered by various instabilities has the potential to adversely influence the coating uniformity, and thus the quality of the final coating [15].

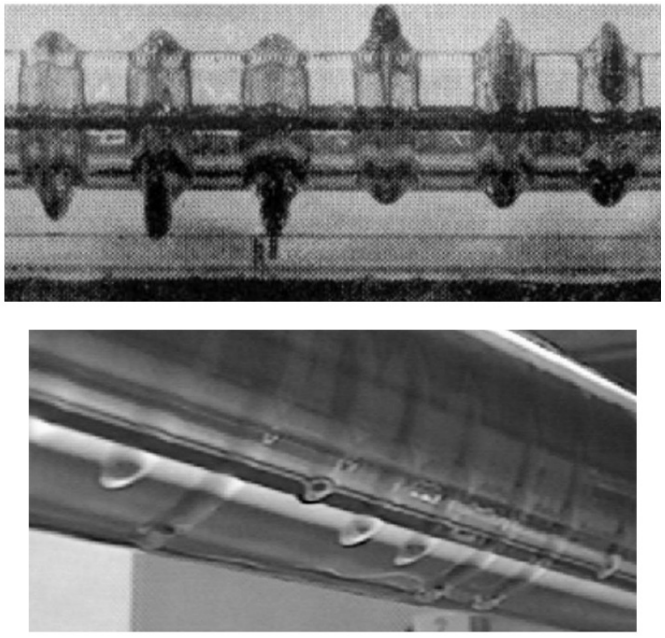

Figure 1.3: (a) Ring-type instability [9]. (b) Drop-type instability [15]

Liquid coatings on rotating cylinders are subject to two common types of instabilities [16]. One is analogous to the Rayleigh-Plateau instability of a liquid jet, and the other is the Rayleigh-Taylor instability. Evans *et al.*, who established a 3D lubrication-based model to study the stability of coating flows on rotating cylinders, reported a transition between these two types of instabilities with a decrease in the cylinder rotation rate [15]. At high rotation rates ($\Omega > \Omega_c$), the coating is unstable to the axial Rayleigh-Plateau instability, which arises due to the combined effects of surface-tension forces and centrifugal forces, leading to the formation of rings [9, 21] or bands [22] enveloping the cylinder (Fig. 1.3(a)). At low rotation rates ($\Omega > \Omega_c$), the film tend to sag under the action of gravity, which may result in a ridge of liquid aligned with the cylinder

axis. Axial perturbations with wavelength longer than the cylinder circumference will grow in amplitude, causing the liquid ridge to break into small droplets evenly spaced at the bottom of the cylinder (Fig. 1.3b) [16, 20].

At moderate rotation rates, there exists a range of rotation rates in which neither the Rayleigh-Plateau instability or the Rayleigh-Taylor instability have the tendency to grow [15], and thus the coating will stay axially uniform during the coating process. Despite the importance of this stable speed window for the coating of discrete objects, the mechanism underlying it is still unknown due to the complex interplay among cylinder rotation, centrifugal acceleration, and surface tension. To reveal this mechanism, we model the 3D coating flows on a rotating cylinder by applying lubrication theory in Chapter 3, and investigate the evolution of the coating for a wide range of cylinder rotation rate. Complementary flow visualization experiments are also performed to validate our numerical simulations.

1.1.3 Surfactant Effects

Surfactants are often present in coating liquids for various purposes including dispersion of solute particles [23], reduction of surface roughness [24], improving surface cleanliness [25], and surface-tension control [26]. The existence of surfactant at the liquid-air interface lowers the surface tension locally, and as a result, a surfactant concentration gradient will give rise to a surface-tension gradient. The resulting surface shear stress then drives flow from regions of high to low surfactant concentration, and this well-known Marangoni phenomenon further complicates coating behavior.

The influence of surfactants on thin-film behavior on planar substrates has been extensively studied in the literature. Jensen and Grotberg considered the spreading of monolayer of surfactant emplaced upon a pre-existing uncontaminated fluid film [29]. By applying lubrication theory, they derived two coupled evolution equations for the film thickness and surfactant concentration at the liquid-air interface. The numerical solutions of these two equations show that the monolayer develops sharp shocklike front at the leading edge under the action of Marangoni stresses, followed by a severely thinned region which is susceptible to film rupture. In addition to this potential rupture instability, surfactant-induced fingering instability that occurs just behind the shocklike front has also been identified in several experimental studies, as reviewed by Craster

and Matar [3]. These surfactant-covered fingers tend to spread in the direction of uncontaminated liquid, and thus lead to a non-uniform coating [30].

For thin-film coating of rotating discrete objects, still little is known about the influence of surfactant on coating behavior. Weidner investigated the stabilizing effect of insoluble surfactants on the coating flows on a stationary cylinder using lubrication theory [31]. It was found that the accumulation of surfactant at the cylinder bottom, induced by the initial drainage flow, leads to a surface shear stress toward the cylinder top. This stress tends to oppose or even reverse the drainage flow, resulting in a more uniform coating film around the cylinder. The work of Weidner [31] is extended in Chapter 2 to take into account the effects of cylinder rotation and surfactant solubility.

1.1.4 Effects of Surface Topography

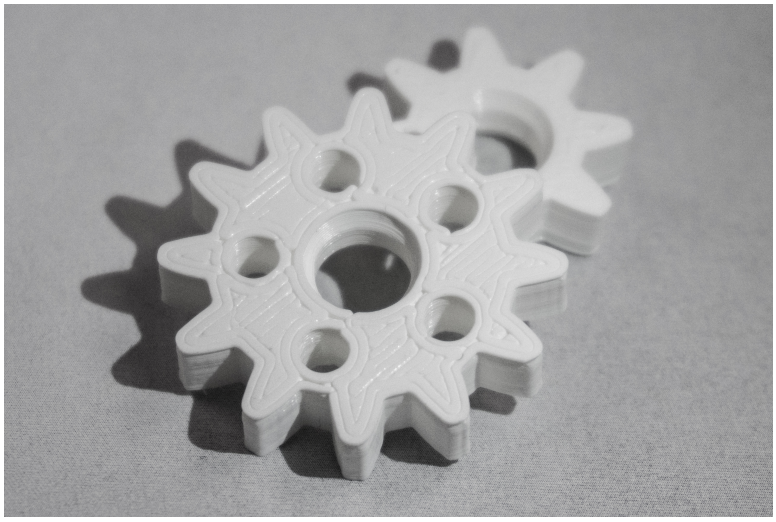

Figure 1.4: Photograph of 3D printed gears, an example of topographically patterned cylinders.

For coating flows on a rotating cylinder, all of the works mentioned above assume that the cylinder surface is perfectly smooth, however, in practice the cylinder surface may be uneven. This unevenness could be caused by surface imperfections or by imposed topographical patterns. The coating of substrates with topography occurs in the manufacturing of microelectronic devices [32], medical implants [33], and 3D printed

parts (Fig. 1.4) [34].

For planar substrates, the presence of topographical features can greatly modify film evolution and adversely influence the quality of the final coating [3]. Recirculation regions, for example, may form in topography valleys if both the topography waviness (the ratio of wave amplitude to wavelength) and film thickness are sufficiently large [35, 36, 37, 38]. These recirculation regions may strongly influence mixing, mass transport, and heat transport, and consequently, the quality of the final (dried) coating [35, 39, 40, 41].

The influence of topographical features on coating flows on rotating cylinders was first studied by Sahu and Kumar [42]. Applying the lubrication approximation, they derived and solved the governing equations for flow on a rotating cylinder patterned with sinusoidal topography. Their results reveal that when gravitational forces are negligible, steady states are reached where liquid tends to accumulate over the pattern troughs at low rotation rates and over the pattern crests at high rotation rates. When gravitational forces are significant, steady states cannot be attained, in contrast to the case of an unpatterned cylinder. In Chapter 4, we studied the more general case where the lubrication approximation is removed.

1.1.5 Effects of Non-Circular Cross Sections

In many applications, such as the production of orthopedic implants [43], metal tubes [44], and food bars [45], the objects to be coated do not have a circular cross section. For these products, curvature variations along the circumference may trigger capillary flows that drive liquid from areas of high to low curvature. The resulting phenomena, including film rupture near sharp corners and uneven liquid and solute distribution, have the potential to adversely influence the quality of the final coating. Limited knowledge about the complex interplay between surface tension, gravity, and rotation in liquid-film flow on objects with non-circular cross-sections hinders the design and optimization of coating processes for these objects.

The influence of non-circular cross sections on coating flows on rotating objects was first studied by Hunt [76]. He considered two-dimensional Stokes flow on the exterior of an elliptical cylinder rotating with uniform angular speed about the center of the ellipse. Neglecting the effects of centrifugal forces and surface tension, he solved the full

Stokes equations numerically and showed that the maximum amount of liquid that can be supported by an elliptical cylinder ($A_m^{\text{Elliptical}}$) is less than that in the circular case (A_m^{Circular}). In both cases, the maximum load decreases as the Stokes number increases (which corresponds to stronger effects of gravity), with approximately the same power-law dependence. Steady solutions were not found on an elliptical cylinder, in contrast to the circular-cylinder case. However, there exist periodic solutions when $A < A_m^{\text{Elliptical}}$, in which the solution is repeated after one full revolution of the cylinder. We extend the work of Hunt [76] in Chapter 5 to incorporate the effects of surface tension as well as centrifugal forces.

1.2 Thesis Overview

The chapters that follow present detailed studies of the flows of thin liquid film on rotating cylinders. Their organization and content are summarized below.

1.2.1 Chapter 2: Thin-film coating of surfactant-laden liquids on rotating cylinders without axial flux

In this chapter, a systematic analysis of surfactant effects on the flow of thin liquid films around rotating cylinders has been carried out to improve fundamental understanding of the coating of discrete objects. In the limiting case where axial variations in film and surfactant concentration are neglected, our focus is on identifying the critical cylinder rotation rate and critical surfactant concentration required to obtain a smooth coating.

To do so, the lubrication approximation is applied to derive three coupled nonlinear evolution equations describing the variation of the film thickness, surfactant surface concentration, and surfactant bulk concentration as functions of time and the angular coordinate. In the absence of gravitational effects, linear stability analysis is used to reveal how soluble surfactants influence the growth of small perturbations triggered by centrifugal forces around cylinder circumference. When gravitational effects are present, evolution equations are solved numerically using a finite difference method to track the film evolution in different flow regimes. Results of our nonlinear simulations provide a guide to taking advantage of the benefits of surfactants while avoiding problems they may cause in the coating process.

1.2.2 Chapter 3: Three-dimensional surfactant-covered flows of thin liquid films on rotating cylinders

This chapter extends the numerical model described in Chapter 2 to incorporate the effects of axial flow. The motivation for this work is to understand the mechanism underlying the stable speed window (§1.1.2) in which instabilities have no tendencies to grow into defects. In addition, we seek to use this 3D model to reveal the influence of an insoluble surfactant on the onset of various axial instabilities including the Rayleigh-Taylor instability and the Rayleigh-Plateau instability.

Both linear stability analysis and nonlinear simulations are used to investigate the complex interplay among surface tension forces, gravitational forces, viscous forces, centrifugal forces, and Marangoni stresses, which are all forces that can potentially trigger instabilities. To analyze the stability of the coating, we also construct two stability diagrams to show the cutoff wavelength of axial perturbations for the cases where surfactant is absent and present respectively. To support results from numerical simulations, complementary flow visualization experiments have also been conducted. Significant details about the experimental setup and a comparison between results of our numerical simulations and our experiments are given in this chapter as well.

1.2.3 Chapter 4: Liquid-film coating on topographically patterned rotating cylinders

This chapter discusses a model problem which is liquid-film flow on rotating cylinders patterned with sinusoidal and trapezoidal topographical features. We are interested in identifying the critical condition in which a coating that closely conforms to the surface geometry can be obtained.

The Stokes equations, augmented with a term accounting for centrifugal forces, are solved in a rotating reference frame using the Galerkin finite-element method (GFEM). A nonlinear evolution equation for the film thickness based on lubrication theory is also solved numerically and its predictions are compared to those from the GFEM calculates to test the validity of the thin-film assumption. The conditions under which coating instabilities, including eddies, "pinches", and "ridges", may form are investigated for a broad range of pattern amplitude and frequency. Results of this study provide an

estimate of when the coating is susceptible to rupture.

1.2.4 Chapter 5: Viscous free-surface flows on rotating elliptical cylinders

To start to understand the influence of a non-circular cross section on the maximum load that can be supported on the cylinder, we take flow of liquid films on rotating elliptical cylinders as a model problem in this chapter. The coating is smooth with no large variation in free-surface curvature when the deposited load is less than that critical value. All the governing equations are solved using GFEM, which provides the location of the free surface as a function of time.

We characterize the bahavior of the maximum load for different values of Stokes number, which measures the strength of gravity-driven drainage, and results are compared to those from the circular-cylinder case. Tracking the transient bahavior of the free surface also allows us to reveal the role surface tension plays in stabilizing the coating. This study serves as a starting point for understanding coating of discrete objects having more complicated cross-section shapes.

1.2.5 Chapter 6: Conclusion and future directions

We summarize our key findings and draw conclusions about practical learnings from this work. Future research directions are provided in this chapter as well.

Chapter 2

Thin-film Coating of Surfactant-laden Liquids on Rotating Cylinders

Abstract - Motivated by the need to improve fundamental understanding of the coating of discrete objects, the influence of surfactants on the flow of thin liquid films around rotating cylinders is considered in this work. The lubrication approximation is applied to derive three coupled nonlinear evolution equations describing the variation of the film thickness, surfactant surface concentration, and surfactant bulk concentration as a function of time and the angular coordinate. In the absence of gravitational effects, linear stability analysis reveals that Marangoni stresses suppress the growth rate of instabilities driven by centrifugal forces and hinder the leveling of perturbations to the film thickness. When gravitational effects are present, Marangoni stresses lower the critical rotation rate needed to cause motion of a liquid lobe around the cylinder. These stresses also lead to faster damping of oscillations in the film thickness at relatively short times, but if strong enough can increase the oscillation amplitude at longer times. In all cases examined, surfactant solubility has the effect of weakening the influence Marangoni stresses.[1]

[1] This chapter has been published in [46].

2.1 Introduction

Coating of non-flat discrete objects is an important processing step for various products, including biomedical devices, food, and automobiles. In practice, the objects to be coated are sometimes rotated to control the film thickness [47] or to deliberately create patterns in the coating [48]. One of the major challenges in developing a fundamental understanding of the coating of rotating discrete objects is the characterization of various instabilities, as these may give rise to defects that degrade the quality of the final product.

Cylinders that rotate about their horizontal axes are commonly used as model rotating discrete objects because of their geometric simplicity. Many experimental studies of thin-film coating with this configuration have been reported, as reviewed by Evans *et al.* [10, 15]. These studies generally consider Newtonian liquids with a constant surface tension.

In practice, however, surfactants are often present in coating liquids for various purposes including dispersion of solute particles [23], reduction of surface roughness [24], improving surface cleanliness [25], and surface-tension control [26]. The existence of surfactant at the liquid-air interface decreases the surface tension locally, and as a result, a surfactant concentration gradient will give rise to a surface-tension gradient. The resulting surface shear stress then drives flow from regions of high to low surfactant concentration, and this well-known Marangoni phenomenon further complicates coating behavior. Although the influence of surfactants on thin-film behavior on planar substrates has been extensively studied [27, 3], little is known about how they influence the coating of rotating discrete objects such as cylinders. The purpose of this contribution is to address this issue.

When a cylinder is coated with a liquid film, the film will tend to sag under the action of gravity, and would simply drain away in the absence of surface tension and cylinder rotation. Moffatt [9] discovered that by invoking the lubrication approximation and neglecting surface tension, inertia, and axial variations in the film thickness, it is possible to obtain an analytical expression for the maximum amount of liquid that can be supported when the cylinder rotates. In terms of a critical rotation rate Ω_c needed

to support a liquid film of mean thickness H, the condition is [10]

$$\Omega_c = \left(\frac{2\pi}{4.443}\right)^2 \left(\frac{H}{R}\right)^2 \frac{\rho g R}{\mu}. \tag{2.1}$$

Here, R is the cylinder radius, ρ is the liquid density, g is the magnitude of the gravitational acceleration, and μ is the liquid viscosity. When $\Omega > \Omega_c$, the liquid film is thicker on the upward-moving side and thinner on the downward-moving side. Such so-called Moffatt-type steady-state solutions or smooth coatings are unique for a given rotation rate [11].

When $\Omega < \Omega_c$, a solution can only be obtained when surface tension is restored [10]. This was discussed in detail by Evans *et al.*, who used lubrication theory to derive a nonlinear evolution equation for the film thickness which was then solved numerically [10]. In this case, a drop-like liquid bulge forms on the underside of the cylinder, and rises higher on the upward-moving side as the rotation rate approaches the critical value. The significant effects of surface tension are confined to the vicinity of the liquid bulge, where large changes in film thickness occur. Many other studies have also explored various aspects of thin-film flows on rotating cylinders while accounting for surface tension (e.g., see [15, 18, 14, 19, 28] and references therein), but to the best of our knowledge the influence of surface-tension gradients due to surfactants has not yet been addressed. The present chapter extends the work of Evans *et al.* [10] to account for the influence of soluble and insoluble surfactant.

In the case where the cylinder is stationary, the influence of insoluble surfactant on film drainage has been considered by Weidner using lubrication theory [31]. It was found that the accumulation of surfactant at the cylinder bottom, induced by the initial drainage flow, leads to a surface shear stress toward the cylinder top. This stress tends to oppose or even reverse the drainage flow, resulting in a more uniform coating film around the cylinder. The present chapter extends the work of Weidner [31] to include the effects of cylinder rotation.

The mathematical model we use, which is based on lubrication theory, is discussed in §2.2. Results are presented in §2.3, where we discuss the cases where gravitational effects are absent and present, and the cases of insoluble and soluble surfactant. Conclusions are given in §2.4.

2.2 Mathematical Model

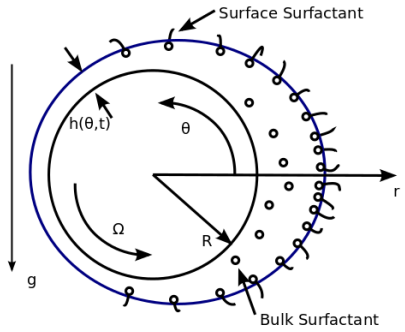

Figure 2.1: Schematic of problem geometry

We consider the flow of a thin film of a Newtonian liquid with constant viscosity μ and density ρ over a horizontal cylinder of radius R (Fig. 2.1). The cylinder rotates counterclockwise about its axis at angular speed Ω. Our focus will be on characterizing film thickness variations around the circumference, so any axial variations are neglected here. The liquid velocity is expressed as

$$\mathbf{u} = w\mathbf{e}_r + (r\Omega + u)\mathbf{e}_\theta \tag{2.2}$$

in cylindrical coordinates (r,θ), where $\mathbf{e}_r$ and $\mathbf{e}_\theta$ are the corresponding unit vectors. The liquid film is assumed to completely wet the cylinder, with thickness $h(\theta, t)$ measured from the cylinder surface. For convenience, a new radial coordinate $z = r - R$ is defined, so all the equations are to be solved in the interval $0 < z < h(\theta, t)$.

The surfactant is assumed to be soluble and can adsorb onto and desorb from the liquid-air interface. The corresponding surface and bulk concentrations are $\Gamma(\theta, t)$ and $c(\theta, z, t)$, respectively. The presence of surfactant at the liquid-air interface lowers the surface tension from its maximum value of σ_0 to $\sigma(\Gamma)$. We assume that the surfactant concentration is sufficiently dilute to permit use of a linear equation of state,

$$\sigma = \sigma_0 + \Gamma \left(\frac{d\sigma}{d\Gamma} \right)_{\Gamma=0}. \tag{2.3}$$

2.2.1 Governing Equations

The equations of mass and momentum conservation are given by

$$\boldsymbol{\nabla} \cdot \mathbf{u} = 0, \tag{2.4}$$

$$\rho \left[\mathbf{u}_t + \mathbf{u} \cdot \boldsymbol{\nabla}\mathbf{u}\right] = -\boldsymbol{\nabla} p + \mu \boldsymbol{\nabla}^2 \mathbf{u} + \rho \mathbf{g}, \tag{2.5}$$

where p denotes pressure, and $\mathbf{g} = (-g \sin\theta)\mathbf{e}_r + (-g\cos\theta)\mathbf{e}_\theta$ with g being a constant characterizing gravitational acceleration.

Convection-diffusion equations describe the evolution of surfactant concentration,

$$\Gamma_t + \boldsymbol{\nabla}_s \cdot (\mathbf{u}_s \Gamma) + (\boldsymbol{\nabla}_s \cdot \mathbf{n})\Gamma(\mathbf{n} \cdot \mathbf{u}) = D_s \boldsymbol{\nabla}_s^2 \Gamma + J, \quad \text{at } z = h(\theta, t), \tag{2.6}$$

$$c_t + \mathbf{u} \cdot \boldsymbol{\nabla} c = D_b \boldsymbol{\nabla}^2 c, \qquad \text{for } 0 < z < h(\theta, t), \tag{2.7}$$

where D_s and D_b are surface and bulk diffusion coefficients, respectively, which are assumed to be constants. The surface gradient operator $\boldsymbol{\nabla}_s = (\mathbf{I} - \mathbf{nn}) \cdot \boldsymbol{\nabla}$, in which $\mathbf{I}$ is the identity tensor and $\mathbf{n}$ is the unit normal pointing outward from the liquid-air interface. Similarly, the surface velocity is $\mathbf{u}_s = (\mathbf{I} - \mathbf{nn}) \cdot \mathbf{u}$. Equations (2.6) and (2.7) are coupled with each other by a linearized sorptive flux [49], $J(\Gamma, c) = k_1 c_s - k_2 \Gamma$, which contains two components: an adsorptive one determined by rate constant k_1 and a desorptive one determined by rate constant k_2. Here, $c_s(\theta, t) = c(\theta, z = h, t)$ is the concentration in the bulk immediately beneath the liquid-air interface, known as the subsurface [49].

On the cylinder surface, $z = 0$, no-slip and no-penetration conditions are applied,

$$u = w = 0. \tag{2.8}$$

In addition, surfactant transport satisfies the no-flux condition at $z = 0$,

$$\left.\frac{\partial c}{\partial z}\right|_{z=0} = 0. \tag{2.9}$$

At the liquid-air interface, $z = h(\theta, t)$, we have normal and tangential stress balances,

$$-p + 2\mu(\mathbf{n} \cdot \boldsymbol{\tau} \cdot \mathbf{n}) = -\sigma\kappa, \tag{2.10}$$

$$2\mu(\mathbf{n} \cdot \boldsymbol{\tau} \cdot \mathbf{t}) = \boldsymbol{\nabla}_s \sigma, \tag{2.11}$$

where $\kappa = \boldsymbol{\nabla}_s \cdot \mathbf{n}$ is the surface curvature, $\mathbf{t}$ is the unit tangent to the interface, and $\boldsymbol{\tau} = [\boldsymbol{\nabla}\mathbf{u} + (\nabla\mathbf{u})^T]/2$ is the rate-of-strain tensor. Since the liquid-air interface is a free surface, the kinematic boundary condition must also be applied,

$$\left.\frac{DF}{Dt}\right|_{z=h(\theta,t)} = 0, \tag{2.12}$$

where $F = z - h(\theta, t)$. The surfactant flux, $J(\Gamma, c)$, has the form

$$J(\Gamma, c) = k_1 c - k_2 \Gamma = \mathbf{n} \cdot (\mathbf{u}c - D_b \boldsymbol{\nabla} c), \quad \text{at } z = h(\theta, t). \tag{2.13}$$

2.2.2 Scaling

Since the liquid films are often thin in practice, we consider the case where the characteristic film thickness H is much smaller than the cylinder radius R, and let $\epsilon = H/R \ll 1$. The lubrication approximation can then be applied to exploit this disparity between the two length scales and yield a simplified set of governing equations. Inspired by prior work on related problems [10, 29], we introduce the following dimensionless quantities which are denoted with tildes:

$$\begin{aligned}
&(z, h) = H(\tilde{z}, \tilde{h}), && r = R\tilde{r}, && t = T\tilde{t}, \\
&u = U\tilde{u}, && w = \epsilon U\tilde{w}, && p = P\tilde{p}, \\
&\Gamma = \Gamma_m\tilde{\Gamma}, && c = c^*\tilde{c}, && \sigma = \sigma_m + \tilde{\sigma}\varphi.
\end{aligned} \tag{2.14}$$

Here, $U = \rho g H^2/\mu$ is a characteristic speed, $T = R/U$ is a characteristic time scale, and $P = \rho g H$ is a characteristic pressure. The mean surfactant concentration is denoted by Γ_m, and σ_m is the surface tension corresponding to Γ_m. The quantity $\varphi = \sigma_0 - \sigma_m$ is a positive constant known as the spreading pressure. In addition, constant $c^* = k_2/k_1\Gamma_m$ is defined to non-dimensionalize the bulk concentration.

Order-of-magnitude estimates for selected dimensional quantities are listed in Table 2.1. Although we assume $H/R \ll 1$ to permit use of the lubrication approximation, prior studies of liquid film flow on rotating cylinders have shown that as long as the rotation rate is high enough, the lubrication approximation works well even when the film thickness is of the same order of magnitude as the cylinder radius [14]. For simplicity, we henceforth drop the tilde notation and all variables are taken to be dimensionless.

Table 2.1: Order-of-magnitude estimates of dimensional quantities. The viscosity, density, and surface tension are representative of a glycerol-water mixture. The values of the bulk and surface diffusivities were obtained from Ref. [50].

Constants	Typical values
Viscosity, μ (P)	0.5
Density, ρ (g/cm^3)	1
Surface tension, σ_0 (dyn/cm)	65
Spreading pressure, φ (dyn/cm)	5
Film thickness, H (cm)	0.001
Cylinder radius, R (cm)	1
Bulk diffusivity, D_b (cm^2/s)	10^{-2}
Surface diffusivity, D_s (cm^2/s)	$10^{-4} - 10^{-2}$

After introducing the above scalings, Eqs. (2.4) and (2.5) become

$$\frac{\partial}{\partial z}(rw) + \frac{\partial u}{\partial \theta} = 0, \tag{2.15}$$

$$-W^2(1+\epsilon z) = -\frac{\partial p}{\partial \theta} + \epsilon \frac{\partial^2 w}{\partial^2 z} - \sin\theta, \tag{2.16}$$

$$0 = -\epsilon \frac{\partial p}{\partial \theta} + \frac{\partial^2 u}{\partial^2 z} + \epsilon \frac{\partial u}{\partial z} - \cos\theta. \tag{2.17}$$

Here, $W = \Omega/\sqrt{g/R}$ is the dimensionless rotation rate. Note that terms of $O(\epsilon^2)$ are neglected in above equations. The Reynolds numbers $Re = \rho^2 g H^2 R/\mu^2$ and $Re_\Omega = \rho\Omega R^2/\mu$ are assumed to be not larger than $O(1)$ so that we can neglect inertial terms as well.

The dimensionless form of the no-slip and no-penetration conditions (2.8) have the form

$$u = w = 0. \tag{2.18}$$

The simplified form of the shear-stress balance at the free surface is given by

$$\frac{\partial u}{\partial z} - \epsilon u = \epsilon Ma \frac{\partial \sigma}{\partial \theta}, \tag{2.19}$$

where $Ma = \varphi/\mu U$ is the Marangoni number, which provides a measure of the strength of surface-tension-gradient forces relative to viscous forces.

The surface curvature can be expressed as

$$\kappa = 1 - \epsilon h - \epsilon \frac{\partial^2 h}{\partial^2 \theta} + O(\epsilon^2). \tag{2.20}$$

We substitute it into Eq. (2.10) and for dilute concentrations of surfactant such that $\varphi/\sigma_m \sim \epsilon$, the normal stress balance can be expressed as

$$-p + 2\epsilon(\mathbf{n}\cdot\boldsymbol{\tau}\cdot\mathbf{n}) = -\frac{1}{\epsilon Bo} + \frac{1}{Bo}(h + \frac{\partial^2 h}{\partial^2\theta}) + \epsilon Ma\sigma. \tag{2.21}$$

The Bond number, $Bo = \rho g H^2/\sigma_m$, is a measure of the importance of surface-tension forces relative to gravitational forces. The outward unit normal $\mathbf{n}$ and rate-of-strain tensor $\boldsymbol{\tau}$ become

$$\mathbf{n} = \mathbf{e}_r - \mathbf{e}_\theta \frac{\epsilon}{r}\frac{\partial h}{\partial\theta} + O(\epsilon^2), \tag{2.22}$$

$$\tau_{rr} = \frac{\partial w}{\partial z}, \tag{2.23}$$

$$\tau_{\theta\theta} = \frac{1}{r}\frac{\partial u}{\partial\theta} + \epsilon\frac{w}{r}, \tag{2.24}$$

$$2\tau_{r\theta} = 2\tau_{\theta r} = \frac{1}{\epsilon}\frac{\partial u}{\partial z} - \frac{u}{r} + \frac{\epsilon}{r}\frac{\partial w}{\partial\theta}. \tag{2.25}$$

Also, the kinematic boundary condition (2.12) takes the following form:

$$\frac{\partial h}{\partial t} + \frac{r\Omega + u}{r}\frac{\partial h}{\partial\theta} - w = 0. \tag{2.26}$$

After non-dimensionalization, the surfactant transport equations (2.6) and (2.7) become

$$r\frac{\partial\Gamma}{\partial t} + \frac{\partial}{\partial\theta}\left(rU_\Omega\Gamma + u_s\Gamma\right) + \epsilon\frac{\partial h}{\partial t}\Gamma = \frac{1}{Pe_s}\frac{\partial}{\partial\theta}\left(\frac{1}{r}\frac{\partial\Gamma}{\partial\theta}\right) + rJ, \tag{2.27}$$

$$r\epsilon^2 Pe_b\left[r\frac{\partial c}{\partial t} + \frac{\partial}{\partial\theta}(rcU_\Omega + cu) + \frac{\partial}{\partial z}(rwc)\right] = r\frac{\partial}{\partial z}\left(r\frac{\partial c}{\partial z}\right) + \epsilon^2\frac{\partial^2 c}{\partial^2\theta}, \tag{2.28}$$

where $U_\Omega = R\Omega/U$ is the ratio of the cylinder surface speed to the characteristic velocity. We require this quantity to be $O(1)$ or smaller to ensure that surface tension plays an essential role in supporting excess liquid on the underside of the cylinder [10]. The surface and bulk Péclet numbers, $Pe_s = UR/D_s$ and $Pe_b = UR/D_b$, represent the strength of surfactant convection relative to diffusion.

The sorptive flux has the form

$$J = K(c_s - \Gamma) = -\frac{1}{\beta Pe_b}\left(\frac{1}{\epsilon^2}\frac{\partial c}{\partial z} - \frac{1}{r^2}\frac{\partial h}{\partial\theta}\frac{\partial c}{\partial\theta}\right), \quad \text{at } z = h(\theta, t), \tag{2.29}$$

and gives rise to two additional dimensionless parameters:

$$K = \frac{k_2 R}{U}, \quad \beta = \frac{k_1}{k_2 H}. \tag{2.30}$$

The constant K represents the strength of desorption relative to convection, and the constant β represents the strength of adsorption relative to desorption. As $\beta \to \infty$ or $K \to 0$, the sorptive flux disappears, and the surface and bulk concentration decouple from each other. In general, it is difficult to obtain reliable estimates of these parameters because of uncertainty regarding the values of k_1 and k_2 [51]. The other key dimensionless parameters governing the problem are summarized in Table 2.2 along with typical values.

Table 2.2: Dimensionless problem parameters

Parameter	Representation	Physical meaning	Typical value
M	$\mu/\rho\sqrt{gR^3}$	Dimensionless viscosity	0.01
W	$\Omega/\sqrt{g/R}$	Dimensionless rotation rate	0.001
Bo	$\rho g R^2/\sigma_m$	Gravitational force/Surface-tension force	10
Ma	$\varphi/\rho g R^2$	Surface-tension-gradient force/Viscous force	0.001
Pe_s	$\rho g R^3/\mu D_s$	Rate of convection/Rate of surface diffusion	$10^4 - 10^6$
Pe_b	$\rho g R^3/\mu D_b$	Rate of convection/Rate of bulk diffusion	10^3

2.2.3 Evolution Equations

2.2.3.1 Film Thickness

In order to solve Eqs. (2.15)-(2.17) subject to the above-mentioned boundary conditions, we apply the following asymptotic expansions:

$$\begin{aligned} u &= u^{(0)} + \epsilon u^{(1)} + ..., \\ w &= w^{(0)} + \epsilon w^{(1)} + ..., \\ p &= \epsilon^{-1} p_0 + p^{(0)} + \epsilon p^{(1)} + ... \end{aligned} \tag{2.31}$$

Here, p_0 is a constant, and from the normal stress balance (2.21) we find that $p_0 = 1/Bo$. We substitute above expansions into Eqs. (2.15)-(2.17) and then equate equal powers of ϵ to yield a sequence of linear problems. The leading-order pressure and velocity

components are

$$p^{(0)} = -\frac{1}{Bo}(h + \frac{\partial^2 h}{\partial^2 \theta}) + (W^2 - \sin\theta)(z - h), \tag{2.32}$$

$$u^{(0)} = \cos\theta \left(\frac{1}{2}z^2 - hz\right), \tag{2.33}$$

$$w^{(0)} = \sin\theta \left(\frac{1}{6}z^3 - \frac{1}{2}hz^2\right) + \frac{1}{2}\cos\theta \frac{\partial h}{\partial \theta} z^2. \tag{2.34}$$

At the next order it turns out that we only need $u^{(1)}$, and it has the form

$$\begin{aligned} u^{(1)} = &- \cos\theta \left(\frac{1}{3}z^3 - hz^2 + \frac{3}{2}h^2 z\right) - \left[\frac{1}{Bo}\frac{\partial}{\partial\theta}\left(h + \frac{\partial^2 h}{\partial^2\theta}\right)\right. \\ &\left. + (W^2 - \sin\theta)\frac{\partial h}{\partial\theta}\right]\left(\frac{1}{2}z^2 - hz^2\right) + Maz\frac{\partial\sigma}{\partial\theta}. \end{aligned} \tag{2.35}$$

Note that the Marangoni term (the last term on the right-hand side) does not appear in the leading-order solutions, suggesting that Marangoni effects only make a small contribution to the film dynamics. But in regions where the concentration gradients are large (large $\partial\sigma/\partial\theta$), Marangoni forces can be significant, driving flow from areas of high concentration to low concentration.

Integrating the continuity equation from $z = 0$ to $z = h$, and substituting the resulting expression into the kinematic condition (2.26), gives the evolution equation for the film thickness. A similar derivation for the surfactant-free case is presented by Evans *et al.* [10], so for brevity we simply state the final result:

$$\begin{aligned} (1 + \epsilon h)\frac{\partial h}{\partial t} = &- U_\Omega \frac{\partial}{\partial\theta}\left(h + \epsilon\frac{h^2}{2}\right) + \frac{\partial}{\partial\theta}\left[\left(\frac{h^3}{3} + \epsilon\frac{h^4}{2}\right)\cos\theta\right] - \epsilon\frac{1}{2}Ma\frac{\partial}{\partial\theta}(\frac{\partial\sigma}{\partial\theta}h^2) \\ &- \epsilon\frac{\partial}{\partial\theta}\left[\frac{h^3}{3Bo}\frac{\partial}{\partial\theta}(h + \frac{\partial^2 h}{\partial^2\theta}) + \frac{h^3}{3}(W^2 - \sin\theta)\frac{\partial h}{\partial\theta}\right]. \end{aligned} \tag{2.36}$$

2.2.3.2 Surfactant Concentration

In Eq. (2.28), the dimensionless group $\epsilon^2 Pe_b$ determines the relative strength of convection to bulk diffusion and is a very small number ($\epsilon^2 Pe_b \ll 1$) for the parameter values given in Tables 2.1 and 2.2. This indicates that any concentration gradients in the vertical direction will quickly be smoothed through bulk diffusion. For this reason,

the bulk concentration $c(\theta, z, t)$ is decomposed into a cross-sectional average component, $C(\theta, t)$, independent of z, and a small perturbation, $C_1(\theta, z, t)$ [49],

$$c(\theta, z, t) = C(\theta, t) + \epsilon^2 Pe_b C_1(\theta, z, t). \tag{2.37}$$

If we define a z-averaged quantity

$$\bar{\Phi}(\theta, z, t) = \frac{1}{h}\int_0^{h(\theta,t)} \Phi(\theta, z, t)\,\mathrm{d}z, \tag{2.38}$$

then the assumption of fast bulk diffusion requires that $\bar{C_1} = 0$.

Using decomposition (2.37) and dropping terms proportional to ϵ^2, the bulk transport equation (2.28) then becomes

$$r\frac{\partial C}{\partial t} + \frac{\partial}{\partial \theta}\left(uC + rU_\Omega C\right) + \frac{\partial}{\partial z}(rwC) = \frac{1}{Pe_b}\left\{\frac{1}{r}\frac{\partial^2 C}{\partial^2 \theta} + \frac{\partial}{\partial z}\left(r\frac{\partial C_1}{\partial z}\right)\right\}. \tag{2.39}$$

Integrating Eq. (2.39) across the film height and using the continuity equation (2.15), we get

$$\begin{aligned}\left(h + \frac{1}{2}\epsilon h^2\right)\frac{\partial C}{\partial t} + h\bar{u}\frac{\partial C}{\partial \theta} + U_\Omega\left(h + \frac{1}{2}\epsilon h^2\right)\frac{\partial C}{\partial \theta} = \\ \frac{1}{Pe_b}\int_0^h \left\{\frac{1}{r}\frac{\partial^2 C}{\partial^2 \theta} + \frac{\partial}{\partial z}\left(r\frac{\partial C_1}{\partial z}\right)\right\}\mathrm{d}z.\end{aligned} \tag{2.40}$$

Using the identity $\overline{\Phi_\theta} = (\bar{\Phi})_\theta + (\bar{\Phi} - \Phi_s)h_\theta/h$ [49], Eq. (2.40) is solved subject to the following boundary conditions:

$$\left.\frac{\partial C_1}{\partial z}\right|_{z=0} = 0, \tag{2.41}$$

$$-\frac{1}{\beta}\frac{\partial C_1}{\partial z} + \frac{1}{\beta Pe_b}\frac{1}{r^2}\frac{\partial h}{\partial \theta}\frac{\partial C}{\partial \theta} = K(C - \Gamma), \quad \text{at } z = h(\theta, t). \tag{2.42}$$

The resulting nonlinear evolution equation for the bulk concentration is

$$(h + \epsilon\frac{h^2}{2})\frac{\partial C}{\partial t} + \left[h\bar{u} + U_\Omega\left(h + \epsilon\frac{h^2}{2}\right)\right]\frac{\partial C}{\partial \theta} = \frac{1}{Pe_b}\frac{\partial}{\partial \theta}\left(h\frac{\partial C}{\partial \theta}\right) + \beta K(\Gamma - C)(1 + \epsilon h), \tag{2.43}$$

where

$$\begin{aligned}h\bar{u} &= \int_0^h (u^{(0)} + \epsilon u^{(1)})\mathrm{d}z \\ &= -\left(\frac{h^3}{3} + \epsilon\frac{h^4}{2}\right)\cos\theta + \epsilon\left\{\frac{h^3}{3Bo}\frac{\partial}{\partial \theta}\left(h + \frac{\partial^2 h}{\partial^2 \theta}\right) + \frac{h^3}{3}(W^2 - \sin\theta)\frac{\partial h}{\partial \theta}\right\} \\ &\qquad + \epsilon\frac{1}{2}Mah^2\frac{\partial \sigma}{\partial \theta}.\end{aligned} \tag{2.44}$$

To obtain the evolution equation for surface concentration, Eq. (2.29) is substituted into Eq. (2.27) to yield

$$r\frac{\partial \Gamma}{\partial t}+\frac{\partial}{\partial \theta}\left(rU_{\Omega}\Gamma+u_s\Gamma\right)+\epsilon\frac{\partial h}{\partial t}\Gamma=\frac{1}{Pe_s}\frac{\partial}{\partial \theta}\left(\frac{1}{r}\frac{\partial \Gamma}{\partial \theta}\right)+rK(C-\Gamma), \tag{2.45}$$

where the surface velocity u_s can be expressed as

$$\begin{aligned} u_s =& -\frac{1}{2}h^2\cos\theta-\epsilon\frac{5}{6}h^3\cos\theta+\epsilon Mah\frac{\partial \sigma}{\partial \theta} \\ &+\epsilon\frac{1}{2}\left\{\frac{h^2}{Bo}\frac{\partial}{\partial \theta}\left(h+\frac{\partial^2 h}{\partial^2 \theta}\right)+h^2(W^2-\sin\theta)\frac{\partial h}{\partial \theta}\right\}. \end{aligned} \tag{2.46}$$

2.2.3.3 Numerical Methods

The third term on the left-hand side of Eq. (2.45) arises due to surface stretching. We did simulations for cases with and without this term, and found that it only causes small changes in the resulting concentration profiles provided that ϵ is small enough; detailed results are omitted here for brevity. Neglecting this stretching term considerably simplifies the numerical scheme, and we will do so in the following calculations. For the same reason, we also drop three small terms of order ϵ in Eq. (2.36), following Evans *et al.* [10].

For convenience we rescale all lengths with the cylinder radius R (as done in Ref. [10]), and the final governing equations become

$$\begin{aligned} \frac{\partial h}{\partial t} =& -MW\frac{\partial h}{\partial \theta}+\frac{\partial}{\partial \theta}\left(\frac{h^3}{3}\cos\theta\right)-\frac{1}{2}Ma\frac{\partial}{\partial \theta}(\frac{\partial \sigma}{\partial \theta}h^2) \\ &-\frac{\partial}{\partial \theta}\left[\frac{h^3}{3Bo}\frac{\partial}{\partial \theta}(h+\frac{\partial^2 h}{\partial^2 \theta})+\frac{h^3}{3}(W^2-\sin\theta)\frac{\partial h}{\partial \theta}\right], \end{aligned} \tag{2.47}$$

$$(h+\frac{h^2}{2})\frac{\partial C}{\partial t}+\left[h\bar{u}+MW\left(h+\frac{h^2}{2}\right)\right]\frac{\partial C}{\partial \theta}=\frac{1}{Pe_b}\frac{\partial}{\partial \theta}\left(h\frac{\partial C}{\partial \theta}\right)+\beta K(\Gamma-C)(1+h), \tag{2.48}$$

$$r\frac{\partial \Gamma}{\partial t}+\frac{\partial}{\partial \theta}\{(MWr+u_s)\,\Gamma\}=\frac{1}{Pe_s}\frac{\partial}{\partial \theta}\left(\frac{1}{r}\frac{\partial \Gamma}{\partial \theta}\right)+K(C-\Gamma)(1+h). \tag{2.49}$$

Similar equations have been used to study leveling and other phenomena [27, 3, 49, 52]. These evolution equations allow for the study of nonlinear phenomena at a relatively

modest cost (compared to solving the full Navier-Stokes equations and surfactant transport equations).

For a fixed set of problem parameters, a partially implicit finite-difference scheme is applied [10, 53]. Film thickness, bulk concentration, and surface concentration are obtained over 400 uniformly discretized nodes on the cylinder at a given instant of time. At each time step, $t = t^{(k+1)}$, we solve Eq. (2.47) subject to the current surface tension $\sigma^{(k)}$, and current film thickness $h^{(k)}$, to yield the new interface shape, $h^{(k+1)}$. After substituting $h^{(k+1)}$ into Eqs. (2.48) and (2.49), we solve for $\Gamma^{(k+1)}$ and $C^{(k+1)}$, which are then used to update the surface tension field $\sigma^{(k+1)}$ for the next time step.

2.3 Results and Discussion

2.3.1 Zero Gravity

We first consider film evolution around rapidly spinning cylinders. In the regime where the gravitational acceleration g is dominated by the centrifugal acceleration $R\Omega^2$ ($W \gg 1$), gravity effects can be neglected. Because Eqs. (2.47)-(2.49) were initially non-dimensionalized using gravity, we rescale them using σ_m/μ as the characteristic velocity and neglect all gravitational terms. This yields

$$\frac{\partial h}{\partial t} = -\frac{\Omega\mu R}{\sigma_m}\frac{\partial h}{\partial \theta} - \frac{1}{3}\frac{\partial}{\partial \theta}\left\{h^3\frac{\partial}{\partial \theta}\left(h + \frac{\partial^2 h}{\partial^2 \theta}\right) + h^3 S\frac{\partial h}{\partial \theta}\right\} + \frac{1}{2}Ma\frac{\partial}{\partial \theta}\left(h^2\frac{\partial \Gamma}{\partial \theta}\right), \quad (2.50)$$

$$h\frac{\partial C}{\partial t} + h\bar{u}\frac{\partial C}{\partial \theta} + \frac{\Omega\mu R}{\sigma_m}(h + \frac{h^2}{2})\frac{\partial C}{\partial \theta} = \frac{1}{Pe_b}\frac{\partial}{\partial \theta}\left(h\frac{\partial C}{\partial \theta}\right) + \beta K(\Gamma - C)r, \quad (2.51)$$

$$r\frac{\partial \Gamma}{\partial t} + \frac{\partial}{\partial \theta}\left(u_s\Gamma + \frac{\Omega\mu R}{\sigma_m}\Gamma\right) = \frac{1}{Pe_s}\frac{\partial}{\partial \theta}\left[(1-h)\frac{\partial \Gamma}{\partial \theta}\right] + K(C - \Gamma)r, \quad (2.52)$$

with parameters

$$\begin{aligned} S &= \rho\Omega^2 R^3/\sigma_m, & Ma &= \varphi/\sigma_m, \\ Pe_s &= R\sigma_m/\mu D_s, & Pe_b &= R\sigma_m/\mu D_b, \\ K &= k_2 R\mu/\sigma_m, & \beta &= k_1/k_2 R. \end{aligned} \quad (2.53)$$

The Weber number, S, measures the importance of centrifugal forces relative to surface-tension forces. To gain insight into system behavior in the absence of gravity, we perform

a linear stability analysis and also numerically solve Eqs. (2.50)-(2.52) for selected cases. The parameter $\Omega\mu R/\sigma_m$ is a capillary number based on the cylinder surface speed.

In the linear stability analysis, each variable is decomposed as follows,

$$\begin{aligned} h(\theta,t) &= H_b + H_0 \exp(ik\theta + st), \\ \Gamma(\theta,t) &= \Gamma_b + \Gamma_0 \exp(ik\theta + st), \\ C(\theta,t) &= C_b + C_0 \exp(ik\theta + st), \end{aligned} \tag{2.54}$$

where, H_b, Γ_b, and C_b represent base-state values and H_0, Γ_0, and C_0 are the perturbation amplitudes, which are assumed to have wavenumber k and growth rate s. Substituting the above three expressions into the evolution equations leads to an eigenvalue problem,

$$\mathbf{A} \begin{pmatrix} H_0 \\ \Gamma_0 \\ C_0 \end{pmatrix} = \left(s + ik\frac{\Omega\mu R}{\sigma_m} \right) \begin{pmatrix} H_0 \\ \Gamma_0 \\ C_0 \end{pmatrix}, \tag{2.55}$$

where

$$\mathbf{A} = \begin{pmatrix} \frac{1}{3}H_b^3 k^2[(1+S)-k^2] & -\frac{1}{2}Mak^2H_b^2 & 0 \\ \frac{1}{2r_b}H_b^2\Gamma_b k^2[(1+S)-k^2] & -\frac{1}{r_b}\left(MaH_b\Gamma_b k^2 + \frac{1}{Pe_s}\frac{1}{r_b}k^2\right) - K & K \\ 0 & \frac{r_b}{H_b}\beta K & -\frac{1}{Pe_b}k^2 - \frac{\beta K r_b}{H_b} \end{pmatrix}. \tag{2.56}$$

Here, $r_b = 1 + H_b$ and we have used the fact that $C_b = \Gamma_b$ in the base state. The amplitude of the perturbation is only controlled by the real part of the eigenvalues, s, while the imaginary part, $ik\Omega\mu R/\sigma_m$, changes the phase. Solving this matrix equation yields three different eigenvalues, which are associated with distinct transport modes. We now consider various limiting cases in order to gain insight into how these transport modes influence stability.

2.3.1.1 Insoluble Surface-passive Surfactant

If surfactant is only present at the free surface, but has no effect on film evolution, then $Ma = K = 0$. In this case, solving Eq. (2.55) yields:

$$s_1 = \frac{1}{3}H_b^3[(1+S)k^2 - k^4], \tag{2.57}$$

$$s_2 = -\frac{1}{r_b^2}\frac{1}{Pe_s}k^2. \tag{2.58}$$

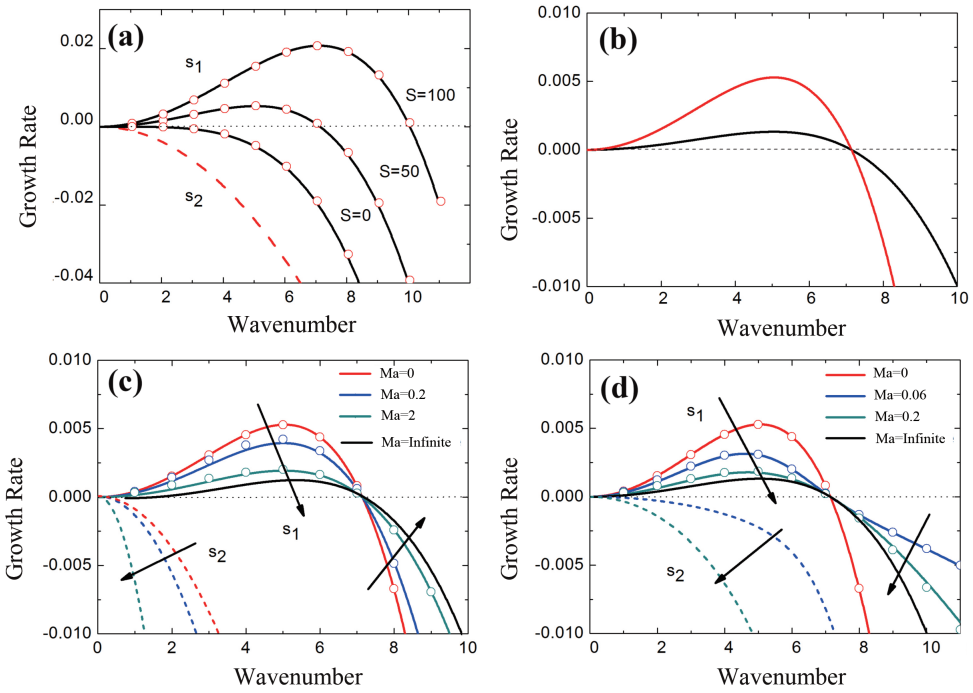

Figure 2.2: Growth rates versus wavenumber in the absence of gravity. Lines are results from the linear stability analysis with H_b= 0.029 and $\Gamma_b = 0.3$. Open circles are results obtained from numerically solving the nonlinear evolution equations. The good agreement between the two serves to validate the numerical solutions. (a) Insoluble surface-passive surfactant. (b) Red line: Insoluble surface-passive surfactant; Black line: Insoluble surfactant with infinite Ma; both are for $S = 50$. (c) Insoluble surfactant with $Pe_s = 10^3$ and $S = 50$. (d) Insoluble surfactant with $Pe = 10^5$ and $S = 50$. The arrows indicate the direction of increasing Marangoni number.

The first eigenvalue (s_1) describes the growth rate of perturbations to the film thickness, and is exactly the same as that for a surfactant-free film (with surface tension σ_m) [10]. The second eigenvalue (s_2) is associated with diffusion-driven decay of concentration perturbations at the free surface.

In Fig. 2.2a, we plot both growth rates s_1 and s_2 against the wavenumber k for $S = 0, 50$, and 100. For a static cylinder, $S = 0$, all wavenumbers are stable (negative growth rate) due to capillary leveling. As the cylinder starts to rotate ($S > 0$), centrifugal forces compete with the capillary forces and tend to destabilize the film (positive growth rate) with a cutoff wavenumber $k_{cutoff} = [\sqrt{1+S}]$, where $[x]$ is the greatest integer less than

x. Perturbations with wavenumber $k > k_{cutoff}$ are leveled (stable region), and those with $k < k_{cutoff}$ grow in amplitude (unstable region).

2.3.1.2 Insoluble Surfactant with Infinite Ma

Now we consider another limiting case, $Ma \to \infty$ and $K = 0$, where surfactant still only exists at the free surface but Marangoni effects start to influence film dynamics. Dividing Eq. (2.19) by Ma and letting $Ma \to \infty$ results in $\partial\Gamma/\partial\theta = 0$, which indicates that the surfactants are uniformly distributed along the free surface.

Substituting this result into Eq. (2.52) yields $u_s = 0$, corresponding to an immobile free surface. Based on this new boundary condition, we are able to solve for the only growth rate in this limit, and it has the form

$$s_\infty = -\frac{1}{12} H_b^3 [(1+S)k^2 - k^4]. \tag{2.59}$$

Note that the absolute value of s_∞ is smaller by a factor of four than the growth rate for the surface-passive-surfactant case (Eq. (2.57)), simply because of the increased hindrance of liquid motion at the immobile surface. We plot both growth rates against wavenumber in Fig. 2.2b with $S = 50$. This result is also valid for leveling of thin films of surfactant solutions on planar substrates [54, 52].

2.3.1.3 Insoluble Surfactant with Intermediate Ma

For intermediate Ma there are two eigenvalues that are coupled together. Fig. 2.2c shows these eigenvalues, denoted s_1 and s_2, as functions of the wavenumber for two different values of Ma with $Pe_s = 10^3$ and $S = 50$. The growth rates for the insoluble surface-passive case ($Ma = 0$) and the immobile-surface case ($Ma \to \infty$) are plotted in the same figure for comparison.

Figure 2.2c indicates that s_2 is always negative and that it becomes even smaller as Ma increases. The other eigenvalue, s_1, is positive over a range of wavenumbers (unstable region) and negative beyond the cutoff wavenumber (stable region). In the unstable region, increasing Ma leads to a reduction in the value of s_1. But in the stable region, the value of s_1 increases. This indicates that surfactant reduces the instability growth rate (region where s_1 is positive) but also slows down the leveling rate (region where s_1 is negative). The mechanism underlying this behavior will be discussed below.

Figure 2.2d shows results similar those in Fig. 2.2c but at a larger value of $Pe_s = 10^5$. In the unstable region, increasing Ma still reduces the growth rate. But in the stable region, increasing Ma now raises the leveling rate (i.e., s_1 becomes more negative) for nonzero Ma. We note that the cutoff wavenumber is independent of Ma and Pe_s.

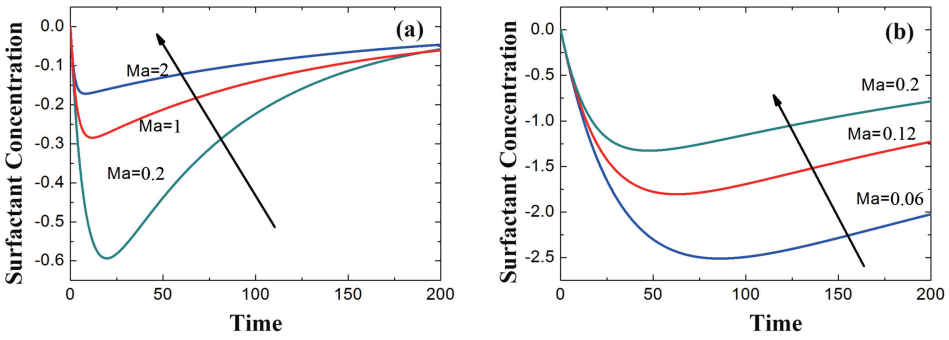

Figure 2.3: Surface concentration perturbation for insoluble surfactant at $\theta = 0$ with $S = 50$, $k = 11$, and (a) $Pe_s = 10^3$, (b) $Pe_s = 10^5$. The initial film thickness and surfactant concentration are 0.029 and 0.3, respectively. The arrows indicate the direction of increasing Marangoni number.

Some of the above observations can be rationalized via an analysis of the eigenfunctions, the results of which we summarize here. In the unstable region, centrifugal forces are stronger than capillary forces and drive liquid from the wave troughs to the wave crests. Surfactant is carried along with the liquid, leading to higher concentrations and lower surface tensions at the crests, and lower concentrations and higher surface tensions at the troughs. The surface-tension gradient then drives flow from the crests to the troughs, hindering instability growth and lowering the value of s_1 in the unstable region.

In the stable region, capillary forces are stronger than centrifugal forces and liquid is driven from the crests to the troughs. The resulting concentration gradient sets up a surface-tension gradient that opposes this leveling flow, leading to larger values of s_1 in the stable region. This explains the increase of s_1 in the stable region shown in Fig. 2.2c. At the cutoff wave number, centrifugal forces are balanced by capillary forces, and no Marangoni flows are present, which is consistent with the constant value of k_{cutoff}.

To explain the different behavior in the stable region shown in Fig. 2.2d for higher Pe_s, it is instructive to directly follow the evolution of concentration perturbations. We

do this by solving Eqs. (2.50) and (2.52) numerically, and extracting the concentration perturbation at $\theta = 0$ as a function of time. These results are shown in Fig. 2.3 for $Pe_s = 10^3$ and $Pe_s = 10^5$, and different values of Ma, where we have chosen a wavenumber in the stable region, $k = 11$.

In the case where $Pe_s = 10^3$ (Fig. 2.3a), the concentration perturbations are nearly the same at long times for all values of Ma due to strong surface diffusion, which implies that the concentration gradients will be nearly the same. Increasing the value of Ma at a constant concentration gradient increases the effectiveness of those gradients, leading to slower leveling as Ma increases. This is consistent with the behavior shown in Fig. 2.2c.

In the case where $Pe_s = 10^5$ (Fig. 2.3b), surface diffusion is much weaker and the difference in the concentration perturbations for different values of Ma is much more pronounced. The smaller concentration perturbations, and hence the smaller concentration gradients, occur for larger values of Ma. This can be rationalized by recognizing that in this regime, it is the Marangoni flows rather than surface diffusion that will smooth out concentration gradients, and the strength of these flows of course increases as Ma does. So, for larger values of Ma, surfactants will not be as effective at hindering the leveling, which is is consistent with the behavior shown in Fig. 2.2d. It is also clear from Figs. 2.2c and 2.2d that leveling is always slower when Marangoni stresses are present ($Ma \neq 0$) compared to the case where they are absent ($Ma = 0$).

Phenomena similar to what is described above have also been reported in studies of the leveling of planar liquid layers [52, 54, 55]. In practice, Pe_s is likely to be very large (Table 2), meaning that increasing the Marangoni number will hinder the growth of small perturbations in the unstable region while speeding up the leveling in the stable region (although the leveling will be slower relative to the $Ma = 0$ case). This behavior is desirable for coating applications where the goal is often to maintain a nearly uniform film thickness.

2.3.1.4 Soluble Surfactant

When we consider soluble surfactant, all of the system parameters will, in general, be non-zero. The resulting three growth rates couple together, but only one is unstable. That eigenvalue is plotted in Fig. 2.4 to investigate the effects of different dimensionless

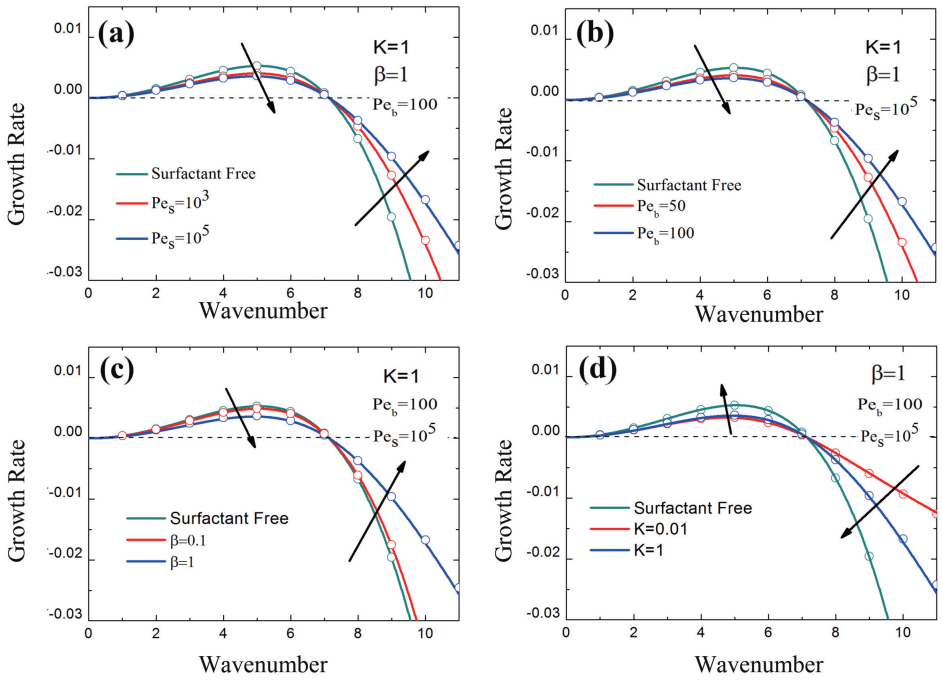

Figure 2.4: Growth rates versus wavenumber in the absence of gravity for soluble surfactants with $Ma = 0.12$, $S = 50$, $H_b = 0.029$, and $\Gamma_b = 0.3$. As in Fig. 2.2, lines are results from the linear stability analysis and open circles are results obtained from numerically solving the nonlinear evolution equations. Shown are influence of (a) surface Péclet number, Pe_s, (b) bulk Péclet number, Pe_b, (c) β, and (d) K. The arrows indicate the direction of increasing each system parameter.

system parameters: Pe_s, K, β, and Pe_b. We summarize here the key features.

As can be seen in Figs. 2.4a and 2.4b, decreasing both Pe_s and Pe_b increases the absolute values of the eigenvalue. This is because a smaller Péclet number corresponds to stronger bulk and surface diffusion, which erases sooner the concentration gradients that oppose the leveling and growth.

Given that the surfactant influences the film dynamics only by its effects at the liquid-air interface, any changes in system parameters that weaken surfactant solubility and thus allow more surfactant to be absorbed at the interface will strengthen the Marangoni effects. According the definitions given earlier, increasing β and decreasing K both correspond to an decrease in surfactant desorption, and hence a decrease in

surfactant solubility. This would be expected to give rise to smaller growth rates and slower leveling rates, as is reflected in Figs. 2.4c and 2.4d.

2.3.2 Gravity Effects

We now incorporate the effects of gravity. To select a parameter regime, we consider a cylinder radius of $R = 5l_c$ $(Bo = 25)$, where $l_c = \sqrt{\sigma_m/\rho g}$ is the capillary length. For a glycerol-water mixture, $\sigma_0 \approx 65$ dyn/cm and $\rho = 1.26$ g/cm^3, yielding $l_c \approx 0.2$ cm and a dimensional cylinder radius of $R \approx 1$ cm. The dimensionless viscosity M controls the time scale, and for the physical properties listed in Table 2.1, $M \approx 0.02$. Note that $M\sqrt{Bo} = \mu/\sqrt{\rho\sigma_m R} = Oh$, the Ohnesorge number, which can be interpreted as a capillary number with a characteristic velocity equal to the capillary wave speed.

All simulations are started with a layer of uniform thickness $h(\theta, t = 0) = 0.007$, which is typical of previous experiments [10]. In this case, the corresponding critical rotation rate given by Eq. (2.1) is $\Omega_c = 0.16$ s^{-1}, or $W_c = 0.0049$ in dimensionless form. In this parameter regime, we solve Eqs. (2.47), (2.48), and (2.49) numerically, again considering various limiting cases.

2.3.2.1 Surfactant-free Flows

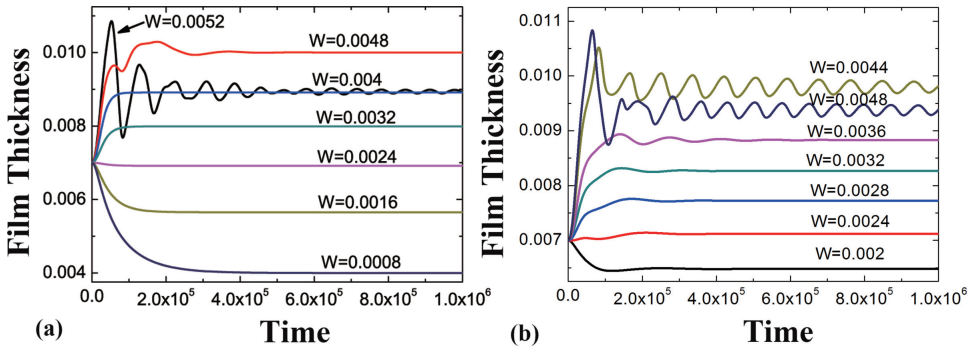

Figure 2.5: Time variation of film thickness at $\theta = 0$ with $W_c = 0.0049$, $h(\theta, t = 0) = 0.007$, $M = 0.02$, and $Bo = 25$. (a) Surfactant-free case. (b) Insoluble surfactant with $Ma = 0.0048$, $Pe_s = 10^6$.

Similar to the zero-gravity case, if we set $Ma = 0$ our evolution equation for film thickness reduces to that presented by Evans *et al.* [10] for a surfactant-free film (with

surface tension σ_m). In order to facilitate comparison with cases where surfactant is present, we plot the time history of film thickness at $\theta = 0$ for different values of the dimensionless rotation rate W in Fig. 2.5a.

For a rotation rate $W < W_c$, the film thickness slowly approaches a steady state in which a liquid drop hangs from the bottom of the cylinder when $W = 0$. As W increases, the liquid drop, rises closer to the $\theta = 0$ point, leading to an increase in the final film thickness at this point as shown in Fig. 2.5a.

The liquid drop rises over the cylinder symmetry plane when $W > W_c$. In this case, the gravitational forces are overwhelmed by the viscous forces and the drop is carried around the cylinder in the direction of rotation. Such a liquid "lobe" gradually decays in size due to surface tension [56], leaving a nearly smooth coating with higher thickness on the upward-moving side and lower thickness on the downward-moving side. In Fig. 2.5a, for $W = 0.0052$ ($> W_c$), there is a sudden drop in film thickness (following an initial increase), reflecting the formation of a lobe. As the lobe starts to rotate around the cylinder, the film thickness oscillates with a fixed frequency and a decaying amplitude, slowly approaching a constant value. The formation of a rotating lobe is necessary for a relatively smooth coating, and its decay rate controls the time needed to obtain such a coating.

2.3.2.2 Insoluble surfactant

For insoluble surfactant, we set $K = 0$, which corresponds to no adsorption or desorption between the surface and the bulk. All simulations are started with uniform surface concentration $\Gamma_0 = 0.1$. We plot the time-evolution of film thickness and surfactant concentration at $\theta = 0$ in Fig. 2.5b with $Ma = 0.0048$ and $Pe_s = 10^6$. It is interesting to find that the sudden drop in film thickness and subsequent oscillations occur even when the rotation rate is still lower than the critical value ($W_c = 0.0049$) calculated from Eq. (2.1).

To explain why the film thickness oscillations occur at lower values of W when Marangoni stresses are present, we plot in Fig. 2.6a the position of the maximum film thickness and maximum surface concentration as a function of W (for values below those which produce oscillations). For any given rotation rate, the maximum film thickness is always located several degrees above the point of maximum surface concentration. This

high concentration region triggers a Marangoni stress that pushes already accumulated liquid drops upward, closer to the symmetry plane (Fig. 2.6a). Since the oscillations occur when the drop rises above the symmetry plane, surfactants lower the rotation rate at which this occurs by raising the position of the drop via Marangoni stresses. As the surface Péclet number increases, these Marangoni stresses increase and push the drop to higher positions, as shown in Fig. 2.6b.

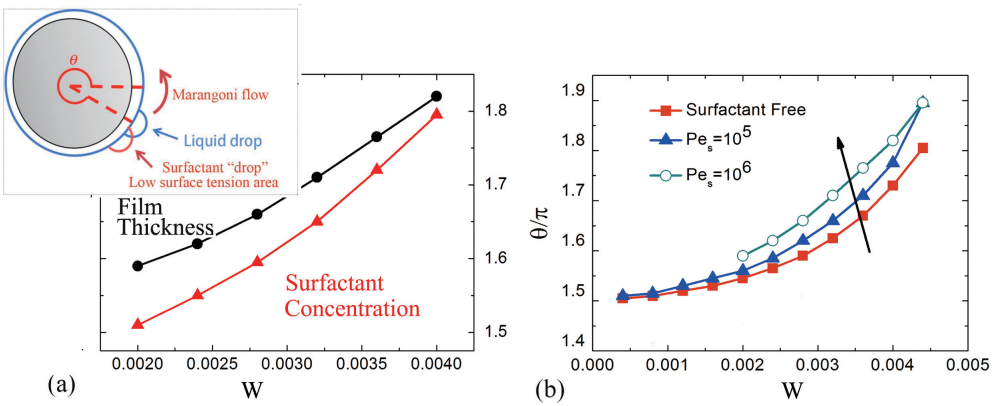

Figure 2.6: (a) Location of the points of maximum thickness and surfactant concentration with $Ma = 0.0048$ and $Pe = 10^6$. (b) Location of the points of maximum film thickness for different values of Pe_s with $Ma = 0.0048$.

To further analyze the nature of the oscillations when Marangoni stresses are present, we plot in Fig. 2.7 the film thickness and surfactant concentration at $\theta = 0$ when $W = 0.0052$. There is a early transient stage, followed by a quasi-steady stage where the oscillations slowly decay. We have selected several times during the early stage (labeled (i)-(iii)) and the later stage (labeled (iv)-(vi)) for the analysis below.

In Figs. 2.8a and 2.8c, we plot the film thickness and concentration profiles at times (i)-(iii) during the early stage. The film thickness is largest near $\theta = 0$ and oscillates due to the motion of the lobe around the cylinder (see §2.3.2.1). The surfactant concentration is also highest near $\theta = 0$, meaning that the surface tension is lower there relative to the adjacent areas. The resulting Marangoni stress would be expected to enhance thinning of the film near $\theta = 0$. This suggests that at early times, the oscillations should actually decay more quickly in the presence of surfactant. We return to this point below.

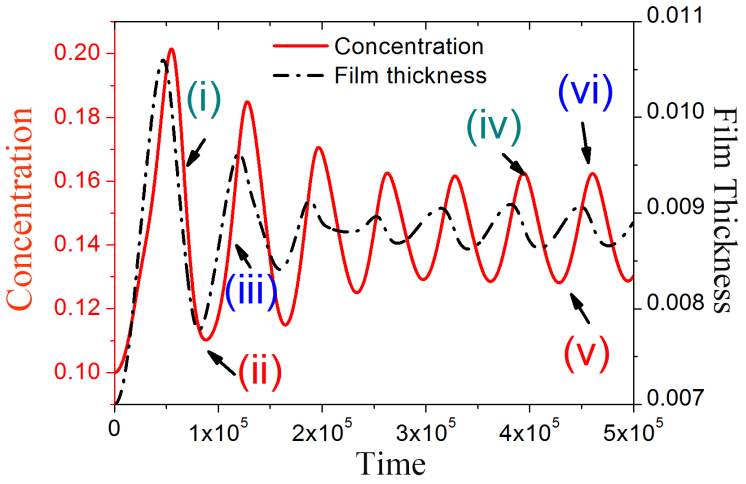

Figure 2.7: Time variation of film thickness (black dashed) and surface concentration (red solid) at $\theta = 0$ with $M = 0.02$, $Bo = 25$, $Ma = 0.0048$, $Pe_s = 10^6$, and $W = 0.0052$.

In Figs. 2.8b and 2.8d, we plot the film thickness and concentration profiles at times (iv)-(vi) during the later stage. Here, the temporal oscillations in the film thickness (Fig. 2.8b) are much less pronounced relative to those in the early stage (Fig. 2.8a). However, the temporal oscillations in the surfactant concentration (Fig. 2.8d) are much more pronounced relative to those in the film thickness (Fig. 2.8b). The concentration is highest near $\theta = 0$ and drops from time (iv) to (v). Inspection of Fig. 2.8b indicates that the film thickness near $\theta = 0$ drops slightly from times (iv) to (v), consistent with a Marangoni flow that drives liquid from near $\theta = 0$ to adjacent areas. The concentration and film thickness profiles at time (vi) are very similar to those at time (iv), indicating that the flow is restoring the conditions that produced the thinning in the first place. This suggests that at later times, Marangoni stresses can drive oscillations in the film thickness.

To gain further insight, we show in Fig. 2.9a the influence of the surface Péclet number on the film thickness oscillations at $\theta = 0$. When Marangoni stresses are present, the oscillations damp more quickly (and the mean film thickness is smaller), consistent with the conjecture made above (Figs. 2.8a and 2.8c). At relatively early times, the damping is greater for $Pe_s = 10^6$ compared to $Pe_s = 10^5$. This can be

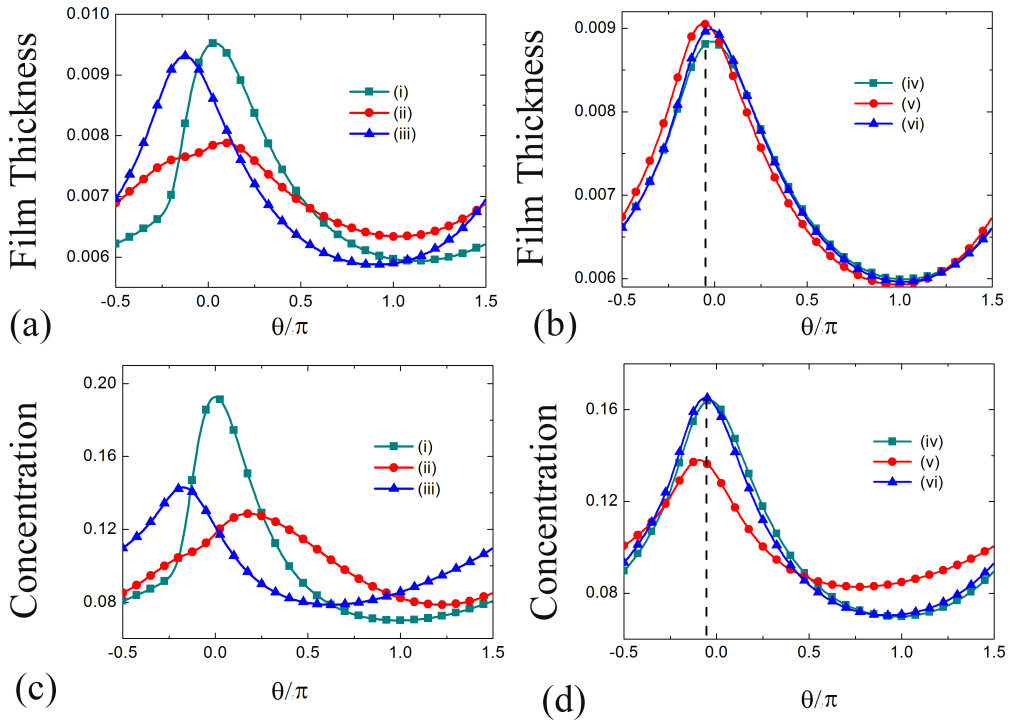

Figure 2.8: Film thickness profiles (a, b) and surface concentration profiles (c, d) at six given times (marked in Fig. 2.7) with $Ma = 0.0048$, $Pe_s = 10^6$, and $W = 0.0052$.

attributed to the fact that surface diffusion is weaker, and thus the Marangoni stresses are stronger, when $Pe_s = 10^6$. At later times, the oscillation amplitudes for the two values of Pe_s are comparable (Fig. 2.9b).

The situation at even later times is shown in Fig. 2.9c. The oscillations are much more damped for $Pe_s = 10^5$ compared to the surfactant-free case. The smaller oscillation amplitude for $Pe_s = 10^5$ is due to the faster damping shown in Fig. 2.9a. Interestingly, the oscillations for $Pe_s = 10^6$ have an amplitude that is larger than that for $Pe_s = 10^5$ and is comparable to that for the surfactant-free case.

The larger oscillation amplitude for $Pe_s = 10^6$ (compared to that for $Pe_s = 10^5$) is consistent with the suggestion made earlier that Marangoni stresses can drive oscillations in the film thickness (Figs. 2.8b and 2.8d). As noted above, the Marangoni stresses are stronger when $Pe_s = 10^6$ due to the weaker surface diffusion. While this leads to faster

damping of the oscillations (compared to that for $Pe_s = 10^5$) at relatively short times, at longer times the stronger Marangoni stresses can increase the oscillation amplitude.

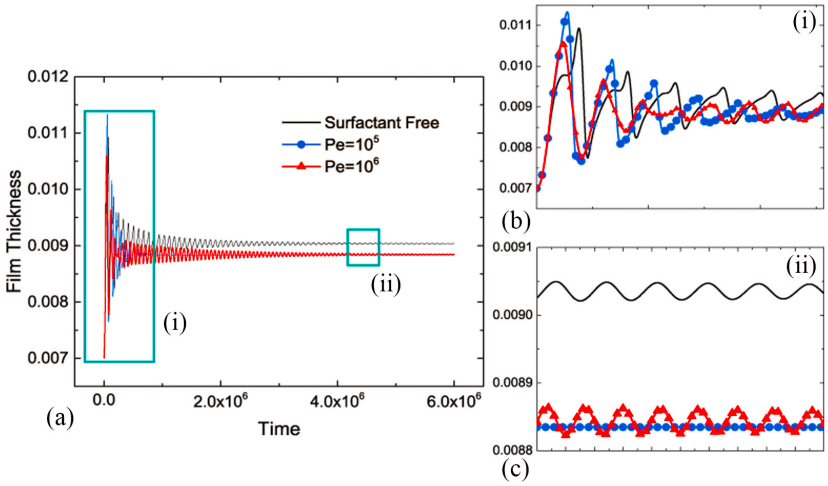

Figure 2.9: Time variation of film thickness for different values of Pe_s at $\theta = 0$ with $Ma = 0.0048$ and $W = 0.0052$. Panels (b) and (c) are enlargements of the regions marked in panel (a).

Although the oscillation amplitudes for $Pe_s = 10^6$ and the surfactant-free case are comparable for the set of parameters used in Fig. 2.9, the oscillation amplitude for $Pe_s = 10^6$ is also determined by the values of W and Ma, as seen in Fig. 2.10. Comparison of Fig. 2.10a with Fig. 2.9c shows that increasing Ma raises the oscillation amplitude for $Pe_s = 10^6$ so it becomes larger than that in the surfactant-free case. This is again consistent with idea that Marangoni stresses can drive oscillations in film thickness.

Comparison of Fig. 2.10b with Fig. 2.9c shows that increasing the value of W (the dimensionless rotation rate) lowers the oscillation amplitude for $Pe_s = 10^6$ so it becomes smaller than that in the surfactant-free case. Increasing W (at fixed dimensionless viscosity M) corresponds to increasing the strength of viscous forces since the product MW appears in Eqs. (2.47)-(2.49). This weakens the Marangoni stresses even at fixed

Ma, since due to the choice of the characteristic velocity the viscosity does not appear in Ma (§2.2.2 and Table 2.2). As a consequence, the Marangoni stresses are less able to drive oscillations in the film thickness at long times and the amplitude is smaller than that in the surfactant-free case (but still larger than that for $Pe_s = 10^5$ where the Marangoni stresses are even weaker due to stronger surface diffusion).

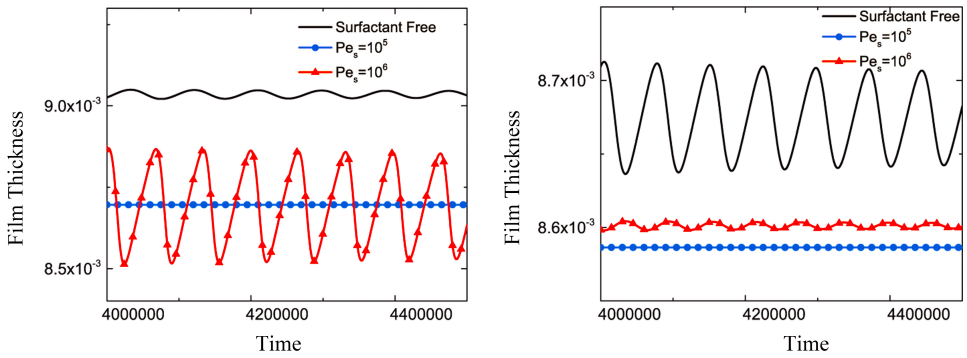

Figure 2.10: Time variation of film thickness at $\theta = 0$ at later times with (a) $Ma = 0.0096$, $W = 0.0052$, and (b) $Ma = 0.0048$, $W = 0.0056$.

2.3.2.3 Soluble Surfactant

When the surfactant is soluble, our observations are similar to those in the zero-gravity case, so for brevity we simply provide a brief summary. As in the zero-gravity case, strengthening of surfactant solubility tends to weaken Marangoni effects. Increasing K and decreasing β lead to greater solubility and thus weaker Marangoni effects. Decreasing the bulk Péclet number (Pe_b) also leads to weaker Marangoni effects since concentration gradients are erased sooner.

2.4 Conclusions

The inclusion of surfactants greatly modifies the behavior of thin liquid films on rotating cylinders. When gravitational effects are negligible, Marangoni stresses suppress the growth rate of instabilities driven by centrifugal forces. Surfactants hinder the leveling

of perturbations to the film thickness, but increasing the strength of Marangoni forces tends to lessen this effect if the surface Péclet number is sufficiently large.

When gravitational effects are present, surfactant-induced Marangoni stresses lower the critical rotation rate needed to cause motion of a liquid lobe around the cylinder. These stresses also lead to faster damping of oscillations in the film thickness at relatively short times, but if strong enough can lead to larger oscillation amplitudes in the film thickness (relative to a surfactant-free film) at longer times. In all cases examined in this chapter, surfactant solubility has the effect of weakening the influence of Marangoni stresses.

The results of this chapter have important implications for the coating of discrete objects such as biomedical devices. Since a smooth coating is usually desired, the addition of surfactants can help achieve this by a lowering of the critical rotation rate, faster damping of oscillations in the film thickness, and suppression of instabilities at high rotation rates. However, this may be counterbalanced by the tendency of surfactants to hinder leveling and produce larger film thickness oscillations at longer times.

Since evaporation is usually present in coating processes, it would be useful to extend the present work in that direction. As evaporation proceeds, the film viscosity will increase and this will oppose the Marangoni effects. It may thus be possible to take advantage of the benefits of surfactants at short times while avoiding problems they may cause at longer times. Three-dimensional effects also arise in practice and it would be useful to extend the present work to account for axial variations in the film thickness [15]. Such extensions, along with asymptotic analysis [56] and flow visualization experiments [15], could lead to the development of coating maps that identify regions of the problem parameter space where high-quality coatings can be obtained.

Chapter 3

Three-dimensional surfactant-covered flows of thin liquid films on rotating cylinders

Abstract—The coating of discrete objects is an important but poorly understood step in the manufacturing of a broad variety of products. An important model problem is the flow of a thin liquid film on a rotating cylinder, where instabilities can arise and compromise coating uniformity. In this work, we use lubrication theory and flow visualization experiments to study the influence of surfactant on these flows. Two coupled evolution equations describing the variation of film thickness and concentration of insoluble surfactant as a function of time, the angular coordinate, and the axial coordinate are solved numerically. The results show that surface-tension forces arising from both axial and angular variations in the angular curvature drive flows in the axial direction that tend to smooth out free-surface perturbations and lead to a stable speed window in which axial perturbations do not grow. The presence of surfactant leads to Marangoni stresses that can cause the stable speed window to disappear by driving flow that opposes the stabilizing flow. In addition, Marangoni stresses tend to reduce the spacing between droplets that form at low rotation rates, and reduce the growth rate of rings that form at high rotation rates. Flow visualization experiments yield observations that are qualitatively consistent with predictions from linear stability analysis and the

simulation results. The visualizations also indicate that surfactants tend to suppress dripping, slow the development of free-surface perturbations, and reduce the shifting and merging of rings and droplets, allowing more time for solidifying coatings in practical applications.

3.1 Introduction

Coating of non-flat objects arises in the manufacturing of a broad variety of products such as aerospace components [57], medical implants [33, 58], and 3D printed parts [34] due to the need to protect or functionalize surfaces. The flows of liquid films that occur in these coating processes are challenging to understand due to the large number of forces at play. These include gravitational, inertial, viscous, surface-tension, and centrifugal forces, and the complex interplay among them may lead to the growth of instabilities and thus coating failure. An understanding of the circumstances under which a coating can be successfully applied is therefore very valuable.

Flow of a thin liquid film on a cylinder that rotates about its horizontal axis provides an entry into the problem of coating non-flat objects, and the stability of these coating flows has been widely investigated as reviewed by Evans *et al.* [15]. There are two major instabilities that can potentially influence the coating uniformity in the axial direction: the Rayleigh-Plateau (RP) instability and the Rayleigh-Taylor (RT) instability. For cylinders with a sufficiently high rotation rate or thin enough film, the film is unstable to the axial RP instability, leading to the formation of "rings" [9, 21] or "bands" [22] enveloping the cylinder.

For cylinders with a sufficiently low rotation rate or thick enough film, the film tends to sag under the action of gravity, resulting in a ridge of liquid aligned with the cylinder axis. In this case, the RT instability dominates and axial perturbations will grow in amplitude, causing the liquid ridge to break into droplets [16] or "fingers" [15] located near the bottom of the cylinder. The occurrence of the ring-type (RP) instability and the droplet-type (RT) instability both lead to formation of coating defects and thus are generally undesired.

Evans *et al.* [15] developed a 3D lubrication-theory-based model to investigate the formation of the RT and RP instabilities on rotating cylinders. Their results show the transition between the two instabilities and the existence of a stable speed window at moderate rotation rates in which the film will stay axially uniform. Despite the importance of this stable speed window for obtaining defect-free coatings on discrete objects, the physical mechanisms underlying it are still unknown, which hinders the possibility of widening the window. One purpose of the present chapter is to understand

these mechanisms.

One possible way to control the growth of axial instabilities is to add surfactants to the coating liquid. Surfactants are commonly used to make coating processes operable over a wider range of operating conditions [26]. The existence of surfactant at a liquid-air interface lowers the surface tension, and as a result, a surfactant concentration gradient gives rise to a surface-tension gradient. The resulting tangential stress then drives flow from high- to low-concentration areas. In practice, this well-known Marangoni effect has been exploited to disperse solute particles [23], reduce surface roughness [24], and improve surface cleanliness [25]. However, new instabilities, including fingering phenomena [59] and van der Waals rupture [60], may arise due to the spreading of surfactant at a liquid-air interface, and these can adversely influence the quality of the final coating.

On planar substrates, these surfactant-induced instabilities have been extensively studied, as reviewed by Oron *et al.* [27] and Craster and Matar [3]. For coating of non-flat substrates, additional flows triggered by substrate curvature complicate surfactant transport, and relatively little is known about the effects of surfactant on the growth of instabilities on rotating discrete objects such as cylinders. A second purpose of the present chapter is to investigate the RP and RT instabilities on a rotating cylinder in the presence of insoluble surfactant.

Most prior work on coating of rotating cylinders neglects thickness variations along the cylinder axis to simplify the governing equations. Moffatt [9] and Pukhnachev [11] considered lubrication-theory-based models in the limit that surface tension is negligible. Their results show the existence of a critical rotation rate, Ω_c, above which the coating is smooth (i.e., no large curvature variations at the free surface) with a thicker film on the upward-moving side of the cylinder and thinner film on the downward-moving side.

For a liquid film of mean thickness H, the critical rotation rate can be expressed as

$$\Omega_c = \left(\frac{2\pi}{4.443}\right)^2 \left(\frac{H}{R}\right)^2 \frac{\rho g R}{\mu}, \tag{3.1}$$

where R is the cylinder radius, ρ is the liquid density, g is the magnitude of the gravitational acceleration, and μ is the liquid viscosity. The addition of surface tension allows for a steady coating to be obtained at rotation rates $\Omega < \Omega_c$ [10]. In this case, the excess

liquid forms a ridge near cylinder bottom that is supported by surface tension. Experiments using Newtonian liquids with a constant surface tension have been conducted by Preziosi and Joseph [13] and Kelmanson [12], and their results show good agreement with Moffatt's critical load condition even with the occurrence of large thickness variations in the axial direction.

Li and Kumar investigated the critical-rotation-rate condition in the presence of surfactant [46] using lubrication theory. Their results show that surfactant-induced Marangoni stresses tend to lower the value of Ω_c and also shorten the time required to obtain a Moffatt-type smooth coating. In the case where the cylinder is stationary, the influence of insoluble surfactant on the growth of the RT instability was considered by Weidner using a similar model [31]. It was found that the accumulation of surfactant at the cylinder bottom, induced by the initial drainage flow, leads to Marangoni stresses directed toward the top of the cylinder. These stresses tend to weaken the gravitational drainage, and as a result, suppress the growth rate of the RT instability. Here, we extend the works of (i) Weidner [31] to include cylinder rotation, (ii) Evans et al. [15] to include insoluble surfactant, and (iii) Li and Kumar [46] to include axial variations.

In §3.2, we present a 3D lubrication-theory-based model that accounts for the influence of insoluble surfactant. A limiting case where gravitational forces are negligible is considered in §3.3 to help build physical understanding. When gravitational forces are restored, stability diagrams for cases where surfactant is absent and present are shown in §3.4. The mechanism behind the stable speed window, which can disappear when Marangoni stresses are present, is presented in §3.5. Surfactant effects on the growth of both the RT and RP instabilities are discussed in §3.6. To complement the modeling results, some flow visualization experiments have been performed, and these are reported in §3.7. Conclusions are given in §3.8.

3.2 Mathematical model

We consider the flow of a thin film of a Newtonian liquid with viscosity μ and density ρ over a cylinder of radius R and length L (Fig. 3.1). The cylinder is assumed to be long enough so that end effects can be neglected. The cylinder rotates counterclockwise around its axis, which is held perpendicular to the gravity vector $\mathbf{g}$, at a constant angular

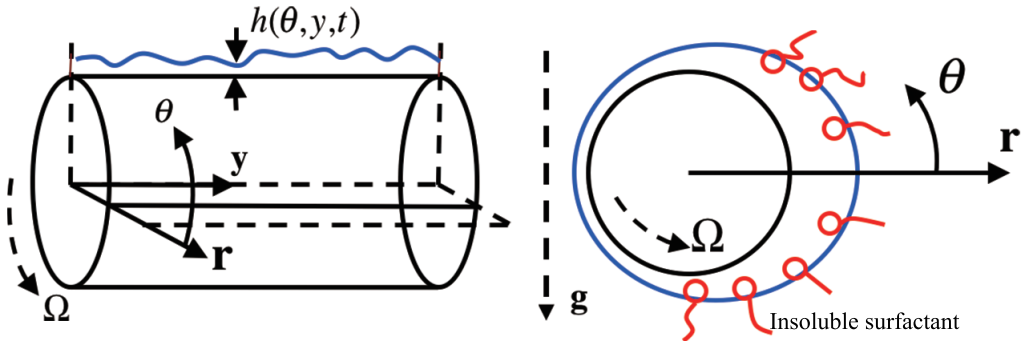

Figure 3.1: Schematic of problem geometry

speed Ω. The liquid velocity is expressed as

$$\mathbf{u} = \omega \mathbf{e}_r + (r\Omega + u)\mathbf{e}_\theta + v\mathbf{e}_y, \tag{3.2}$$

in cylindrical coordinates (r, θ, y), where $\mathbf{e}_r$, $\mathbf{e}_\theta$, and $\mathbf{e}_y$ are the corresponding unit vectors. The liquid is assumed to completely wet the cylinder and is confined to a region $R < r \leq R + h$, where the film thickness, $h(\theta, y, t)$, is measured from the cylinder surface and is a function of θ, y, and time, t.

We consider the limiting case where the surfactant is insoluble and its concentration is sufficiently dilute to permit use of a linear equation of state to describe the relationship between surfactant concentration $\Gamma(\theta, y)$, and surface tension, $\sigma(\Gamma)$,

$$\sigma = \sigma_0 + \Gamma \left(\frac{d\sigma}{d\Gamma} \right)_{\Gamma=0}, \tag{3.3}$$

where σ_0 is the surface tension of a surfactant-free interface.

3.2.1 Governing equations

The equations of mass and momentum conservation are given by

$$\boldsymbol{\nabla} \cdot \mathbf{u} = 0, \tag{3.4}$$

$$\rho \left[\mathbf{u}_t + \mathbf{u} \cdot \boldsymbol{\nabla} \mathbf{u} \right] = -\boldsymbol{\nabla} p + \mu \boldsymbol{\nabla}^2 \mathbf{u} + \rho \mathbf{g}, \tag{3.5}$$

where p is pressure and $\mathbf{g} = -g\sin(\theta)\mathbf{e}_r - g\cos(\theta)\mathbf{e}_\theta$. For convenience, we define a new radial coordinate $z = r - R$, so all governing equations are solved in the interval $0 \leq z \leq h(\theta, y, t)$.

On the cylinder surface, $z = 0$, no-slip and no-penetration conditions are applied,

$$u = \omega = v = 0. \tag{3.6}$$

At the liquid-air interface, $F(\theta, y, z, t) = z - h(\theta, y, t) = 0$, the liquid needs to satisfy the normal and tangential stress balances and the kinematic condition,

$$-p + 2\mu(\mathbf{n} \cdot \boldsymbol{\tau} \cdot \mathbf{n}) = -\sigma\kappa, \tag{3.7}$$

$$2\mu(\mathbf{n} \cdot \boldsymbol{\tau} \cdot \mathbf{t}) = \boldsymbol{\nabla}_s \sigma, \tag{3.8}$$

$$\left.\frac{DF}{Dt}\right|_{z=h(\theta,y,t)} = 0, \tag{3.9}$$

where $\mathbf{n}$ and $\mathbf{t}$ are the unit outward normal and tangent vectors, $\boldsymbol{\nabla}_s = (\mathbf{I} - \mathbf{nn}) \cdot \boldsymbol{\nabla}$ is the surface gradient operator, $\mathbf{I}$ is the identity tensor, $\kappa = \boldsymbol{\nabla}_s \cdot \mathbf{n}$ is the surface curvature, $\boldsymbol{\tau} = [\boldsymbol{\nabla}\mathbf{u} + (\boldsymbol{\nabla}\mathbf{u})^T]/2$ is the rate-of-strain tensor, and D/Dt is the material derivative

The surfactant concentration at the liquid-air interface is governed by the following convection-diffusion equation:

$$\Gamma_t + \boldsymbol{\nabla}_s \cdot (\mathbf{u}_s \Gamma) + (\boldsymbol{\nabla}_s \cdot \mathbf{n})\Gamma(\mathbf{n} \cdot \mathbf{u}) = D\boldsymbol{\nabla}_s^2 \Gamma, \tag{3.10}$$

where D is the surface diffusivity.

3.2.2 Scaling

We consider the case where the characteristic film thickness, H, is much smaller than the cylinder radius, R, $\epsilon \equiv H/R \ll 1$, so that lubrication theory can be applied. Following Refs. [10] and [46], we scale velocity with $U = \rho g h^2/\mu$, pressure with $P = \mu U/H$, and time with R/U, so that

$$\begin{aligned}
&(z, h) = H(\tilde{z}, \tilde{h}), && (r, y) = R(\tilde{r}, \tilde{y}) && t = T\tilde{t}, \\
&u = U\tilde{u}, && w = \epsilon U\tilde{w}, && v = U\tilde{v}, \\
&\Gamma = \Gamma_m\tilde{\Gamma}, && \sigma = \sigma_m + \tilde{\sigma}\varphi, && p = P\tilde{p}.
\end{aligned} \tag{3.11}$$

Here, the dimensionless quantities are denoted with tildes. The terms Γ_m and σ_m are the mean surfactant concentration and the corresponding surface tension, respectively. Since the presence of surfactant lowers the surface tension, the spreading pressure,

$\varphi = \sigma_0 - \sigma_m$, is a positive constant. Order-of-magnitude of estimates for selected dimensional quantities are listed in Table 3.1. For simplicity, we henceforth drop the tilde notation and all variables are taken to be dimensionless.

Table 3.1: Order-of-magnitude estimates of dimensional quantities. The viscosity, density, and surface tension are representative of a glycerol-water mixture. The values of the bulk and surface diffusivities were obtained from Ref. [50].

Constants	Order of magnitude
Viscosity, μ (P)	0.1
Density, ρ (g/cm^3)	1
Surface tension, σ_0 (dyn/cm)	100
Spreading pressure, φ (dyn/cm)	1
Film thickness, H (cm)	0.001
Cylinder radius, R (cm)	0.1
Surface diffusivity, D (cm^2/s)	$10^{-4} - 10^{-2}$
Cylinder rotation rate, Ω (rad/s)	$10 - 30$

With the above scalings, Eqs. (3.4), (3.5), and (3.10) and the corresponding boundary conditions can be simplified using the lubrication approximation (see Appendix A and Refs. [10], [15], and [31] for details), leading to two coupled evolution equations for the film thickness and surfactant concentration,

$$\begin{aligned}(1+h)\frac{\partial h}{\partial t} =& -MW\frac{\partial}{\partial\theta}\left(h+\frac{h^2}{2}\right)+\frac{\partial}{\partial\theta}\left[\left(\frac{h^3}{3}+\frac{h^4}{2}\right)\cos\theta\right] \\ & -\overline{\boldsymbol{\nabla}}\cdot\left[\frac{h^3}{3Bo}\overline{\boldsymbol{\nabla}}(h+\overline{\nabla}^2 h)+\frac{h^3}{3}(W^2-\sin\theta)\overline{\boldsymbol{\nabla}}h-\frac{1}{2}Mah^2\overline{\boldsymbol{\nabla}}\Gamma\right],\end{aligned} \tag{3.12}$$

$$r\frac{\partial\Gamma}{\partial t}+\frac{\partial}{\partial\theta}\left(rMW\Gamma+u_s\Gamma\right)+\frac{\partial}{\partial y}\left[\Gamma v_s\right]+\frac{\partial h}{\partial t}\Gamma=\frac{1}{Pe}\frac{\partial}{\partial\theta}\left(\frac{1}{r}\frac{\partial\Gamma}{\partial\theta}\right)+\frac{1}{Pe}\frac{\partial}{\partial y}\left(r\frac{\partial\Gamma}{\partial y}\right), \tag{3.13}$$

where

$$\overline{\boldsymbol{\nabla}}=\mathbf{e}_\theta\frac{\partial}{\partial\theta}+\mathbf{e}_y\frac{\partial}{\partial y}\qquad\text{and}\qquad\overline{\nabla}^2=\frac{\partial^2}{\partial\theta^2}+\frac{\partial^2}{\partial y^2}. \tag{3.14}$$

Table 3.2 gives the definitions, physical meanings, and typical values of the dimensionless parameters. Note that operators $\overline{\boldsymbol{\nabla}}$ and $\overline{\nabla}^2$ are not the usual gradient and Laplacian in cylindrical coordinates.

In Eqs. (3.12) and (3.13), we have neglected terms of $O(\epsilon^2)$ and higher and also rescaled all lengths with the cylinder radius R as done in Refs. [10] and [15]. The

surface velocity, $(u_s, v_s) = (u, v)|_{z=h}$, is

$$\begin{aligned} u_s =& -\frac{1}{2}h^2\cos\theta - \frac{5}{6}h^3\cos\theta - Mah\frac{\partial\Gamma}{\partial\theta} \\ &+ \frac{1}{2}\left\{\frac{h^2}{Bo}\frac{\partial}{\partial\theta}\left(h + \overline{\nabla}^2 h\right) + h^2(W^2 - \sin\theta)\frac{\partial h}{\partial\theta}\right\}, \\ v_s =& \frac{1}{2}\left\{\frac{h^2}{Bo}\frac{\partial}{\partial y}\left(h + \overline{\nabla}^2 h\right) + h^2(W^2 - \sin\theta)\frac{\partial h}{\partial y}\right\} - Mah\frac{\partial\Gamma}{\partial y}. \end{aligned} \tag{3.15}$$

When Marangoni effects are absent($Ma = 0$), Eq. (3.12) reduces to that obtained by Evans *et al.* [10]. In the limiting case where the cylinder is stationary ($W = 0$), Eqs. (3.12) and (3.13) are consistent with the evolution equations obtained by Weidner [31].

Table 3.2: Dimensionless problem parameters

Parameter	Representation	Physical meaning	Typical value
M	$\mu/\rho\sqrt{gR^3}$	Dimensionless viscosity	0.007
W	$\Omega/\sqrt{g/R}$	Dimensionless rotation rate	$0.1 - 0.3$
Bo	$\rho g R^2/\sigma_m$	Gravitational forces/Surface-tension forces	1
Ma	$Ma = (\sigma_0 - \sigma_m)/\mu U$	Surface-tension-gradient forces/Viscous forces	0.001
Pe	$\rho g R^3/\mu D$	Convection rate/Diffusion rate	10^5

For a fixed set of problem parameters (W, M, Bo, Pe, and Ma), an alternating direction implicit (ADI) finite-difference method similar to that used in Refs. [61] and [62] is applied to solve Eqs. (3.12) and (3.13). Following Ref. [46], we neglect the fourth term on the left-hand side of Eq. (3.13), $(\partial h/\partial t)\Gamma$, to simplify our numerical scheme. This term arises due to surface stretching, and our simulations show that it only causes small changes in the resulting concentration profiles for the thin coatings considered here.

Second-order centered differences are used to discretize the spatial derivatives, and an iterative procedure is applied at each timestep to improve solution accuracy [62]. The (θ, y) domain is discretized into a mesh of $n_\theta \times (n_y + 1)$ grid points with grid spacing $\Delta_\theta = \Delta_y = 2\pi/n_\theta$ and cylinder length $L = n_y\Delta_y = 2\pi n_y/n_\theta$. Following Refs. [10] and [31], no-flux boundary conditions are imposed at the two ends of the cylinder ($y = 0$ and $y = L$), and periodicity is imposed in the θ direction ($h(\theta, y) = h(\theta + 2\pi, y)$). In our simulations, we choose $n_\theta = 150$ to 200 and $n_y = 250$ to 500. For each set of n_θ and n_y used to generate the results shown here, increasing the number of grid points

did not change the results within graphical accuracy. Typical computation times for a given run ranged from one day to 1 week on a workstation with a 2.8 GHz Intel Xeon processor.

3.3 Zero-gravity case

Although the main focus of this chapter is on the case where gravitational effects are significant, it is instructive to first consider the case where the cylinder is spinning so rapidly that gravitational effects are negligible. Since it is no longer appropriate to nondimensionalize Eqs. (3.12) and (3.13) using gravity, we rescale them using σ/μ and σ/R as the new characteristic velocity and pressure (stress), respectively [10, 42, 63]. The resulting evolution equations become

$$(1+h)\frac{\partial h}{\partial t} = -\frac{\Omega\mu R}{\sigma_m}\frac{\partial h}{\partial \theta} - \frac{1}{3}\overline{\boldsymbol{\nabla}}\cdot\left\{h^3\overline{\boldsymbol{\nabla}}\left(h+\overline{\nabla}^2 h\right)+h^3 S\overline{\nabla}h\right\}+\frac{1}{2}Ma\overline{\boldsymbol{\nabla}}\cdot\left(h^2\overline{\boldsymbol{\nabla}}\Gamma\right), \quad (3.16)$$

$$r\frac{\partial \Gamma}{\partial t}+\frac{\partial}{\partial \theta}\left(r\frac{\Omega\mu R}{\sigma_m}\Gamma+u_s\Gamma\right)+\frac{\partial}{\partial y}\left[\Gamma v_s\right]=\frac{1}{Pe}\frac{\partial}{\partial \theta}\left(\frac{1}{r}\frac{\partial \Gamma}{\partial \theta}\right)+\frac{1}{Pe}\frac{\partial}{\partial y}\left(r\frac{\partial \Gamma}{\partial y}\right), \quad (3.17)$$

where the Marangoni number, Ma, the Péclet number, Pe, and the dimensionless rotation rate (Weber number), S, are defined as

$$Ma=\varphi/\sigma_m, \qquad Pe=R\sigma_m/\mu D, \qquad S=\rho\Omega^2R^3/\sigma_m.$$

3.3.1 Linear stability analysis

When gravitational forces are absent, a film of constant thickness with a uniform surfactant concentration is a solution of the governing equations. We examine the fate of small perturbations to this solution via a linear stability analysis (LSA), in which the following normal mode decomposition is used for h and Γ,

$$\begin{aligned} h(x,y,t) &= H_b + H_0\exp(ik_\theta\theta + ik_y y + st), \\ \Gamma(x,y,t) &= \Gamma_b + \Gamma_0\exp(ik_\theta\theta + ik_y y + st), \end{aligned} \quad (3.18)$$

where H_b and Γ_b are the base-state values, and H_0 and Γ_0 are the perturbation amplitudes, which are assumed to have real-valued wavenumbers k_θ and k_y and growth rate s.

Substitution of Eq. (3.18) into the linearized versions of Eqs. (3.16) and (3.17) leads to an eigenvalue problem of the form

$$\mathbf{A}\begin{pmatrix} H_0 \\ \Gamma_0 \end{pmatrix} = \left(s + ik_\theta \frac{\Omega\mu R}{\sigma_m}\right)\begin{pmatrix} H_0 \\ \Gamma_0 \end{pmatrix}, \tag{3.19}$$

where

$$\mathbf{A} = \begin{pmatrix} \frac{H_b^3}{3r_b}k^2[(1+S)-k^2] & -\frac{1}{2r_b}Mak^2H_b^2 \\ \frac{1}{2r_b}H_b^2\Gamma_b k^2[(1+S)-k^2] & -\frac{1}{r_b}\left(MaH_b\Gamma_b k^2 + \frac{1}{Pe_s}\frac{1}{r_b}k_\theta^2 + \frac{1}{Pe_s}r_b k_y^2\right) \end{pmatrix}. \tag{3.20}$$

Here, $k = (k_\theta^2 + k_y^2)^{1/2}$ and $r_b = 1 + H_b$. The two values of the growth rate can be determined analytically, but we do not show the expressions for brevity. It turns out that both values of s are purely real, but only one of them is positive over a range of wavenumbers and it is this value which is discussed below.

It is useful to first consider separately the cases of purely angular and purely axial perturbations when Marangoni stresses are absent ($Ma = 0$). Purely angular perturbations ($k_y = 0$) were considered in Ref. [10], and the corresponding growth rate is

$$s_\theta = \frac{1}{3}H_b^3((1+S)k_\theta^2 - k_\theta^4). \tag{3.21}$$

Angular perturbations with $k_\theta < k_\theta^{\text{cutoff}}$ have positive growth rates and grow in amplitude due to centrifugal forces, while those with $k_\theta > k_\theta^{\text{cutoff}}$ have negative growth rates and decay due to surface tension. The cutoff wavenumber, k_θ^{cutoff}, and the most-dangerous wavenumber, $k_\theta^{\max}$, are

$$k_\theta^{\text{cutoff}} = [\sqrt{1+S}], \tag{3.22}$$

$$k_\theta^{\max} = [\sqrt{(1+S)/2}], \tag{3.23}$$

where $[x]$ is the greatest integer less than x (Due to periodicity, k_θ is restricted to integer values.) Note that when $S = 0$ (stationary cylinder), purely angular perturbations do not grow.

For purely axial perturbations ($k_\theta = 0$), it turns out that the growth rate has the same expression with k_y in place of k_θ, i.e., $s_y = \frac{1}{3}H_b^3((1+S)k_y^2 - k_y^4)$. The cutoff wavenumber is $k_y^{\text{cutoff}} = \sqrt{1+S}$ and the most dangerous wavenumber is $k_y^{\max} = \sqrt{(1+S)/2}$. In contrast to purely angular perturbations, purely axial perturbations

can grow when $S = 0$, which corresponds to the Rayleigh-Plateau instability. When $S = 0$, perturbations having a wavelength longer than the cylinder circumference will tend to grow. When $S \neq 0$, centrifugal forces further destabilize perturbations, causing the growth rates to increase and the band of unstable wavenumbers to widen.

When Marangoni stresses are present, we can no longer obtain analytical expressions for the cutoff and most-dangerous wavenumbers. The case of purely angular perturbations ($k_y = 0$) was considered in Ref. [46], and it was found that surfactant-induced Marangoni stresses reduce the growth rates but do not significantly change the cutoff and most-dangerous wavenumbers. This occurs because the surfactant concentration perturbations are in phase with the interface perturbations, lowering the surface tension at the interface crests relative to the troughs. The resulting Marangoni stresses then drive a flow back to the troughs, thereby reducing the instability growth rates. We have conducted a similar analysis for purely axial perturbations ($k_\theta = 0$) and observe the same behavior. Rather than showing detailed results here, we refer the reader to Appendix B.

3.3.2 Nonlinear evolution

We now turn to the nonlinear evolution of the instabilities discussed in §3.3.1. The finite-difference scheme described in §3.2 was validated by comparison with the LSA results of §3.3.1. Excellent agreement was observed for both purely angular and purely axial perturbations for both $Ma = 0$ and $Ma \neq 0$ (results not shown). Here, we examine what happens when perturbations in both directions grow simultaneously using a representative set of problem parameters. The following initial condition is used:

$$h(\theta, y, t = 0) = h_0(1 + \alpha \cos(k_\theta \theta) + \alpha \cos(k_y y)), \tag{3.24}$$

where α denotes the perturbation amplitude and h_0 denotes the mean film thickness.

We first set $Ma = 0$ and consider an initial perturbation with $k_\theta = 2 < k_\theta^{\max} = 3$ and $k_y = k_y^{\max} = 3$. To gain insight into how the flow transports surfactant, we also calculate the concentration field Γ even though it does not influence the film shape when $Ma = 0$. The evolution of the film follows two distinct stages, and we show in Figs. 3.2a and 3.2c the free-surface profiles and surfactant distributions in these two stages. For ease of visualization, the corresponding free-surface profiles around the cylinder

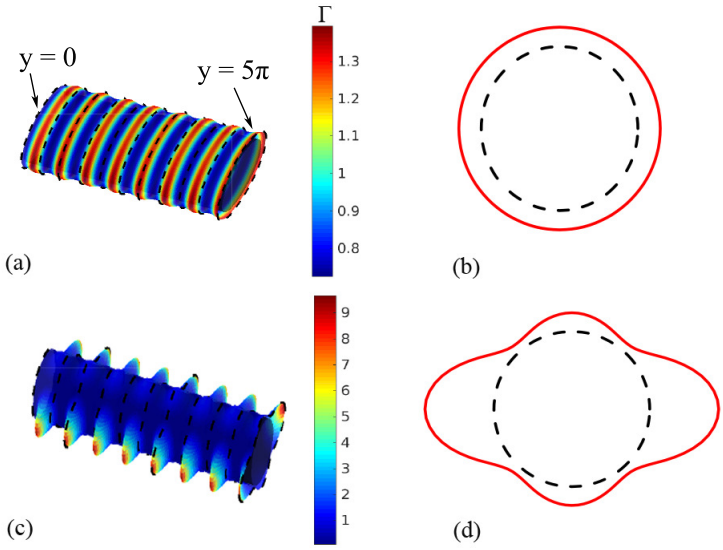

Figure 3.2: (a, c) Free-surface profiles and surfactant distributions in the zero-gravity case with $h_0 = 0.03162$, $\alpha = 10^{-5}$, $k_y = 3$, $k_\theta = 2$, $S = 20$, $Ma = 0$, and $Pe = 10^5$ at (a) $t = 7 \times 10^3$ and (b) $t = 10^4$. The corresponding free-surface profiles around the cylinder circumference at $y = 0$ are plotted in panels (b) and (d) with red solid lines. The black dashed lines indicate the cylinder surface. For ease of visualization, the thickness plotted in panels (a)-(d) is five times larger than the actual value. The spacing between the dashed lines in panels (a) and (c) is 0.5π.

circumference at $y = 0$ (marked in Fig. 3.2a) are shown in Figs. 3.2b and 3.2d with red solid lines.

During the early stage (Fig. 3.2a), 7.5 rings develop along the axis ($k_y \times L/2\pi = 7.5$), while the coating stays almost axisymmetric (Fig. 3.2b). This is simply because the initial perturbation has a higher growth rate in the axial direction. As these rings grow in size, they become unstable to angular perturbations in the later stage and each of them breaks into two liquid droplets ($k_\theta = 2$) connected by relatively thin films as shown in Figs. 3.2c and 3.2d. The growth of these droplets leads to a highly distorted free-surface shape, which significantly increases computational costs, and for this reason, we are unable to find a steady state with our lubrication model.

For an initial perturbation with $k_\theta = 3$ and $k_y = 2$, the evolution of the coating also follows two distinct stages. The corresponding free-surface profiles and surfactant distributions at $t = 7 \times 10^3$ and $t = 10^4$ are shown in Fig. 3.3, along with the free-surface

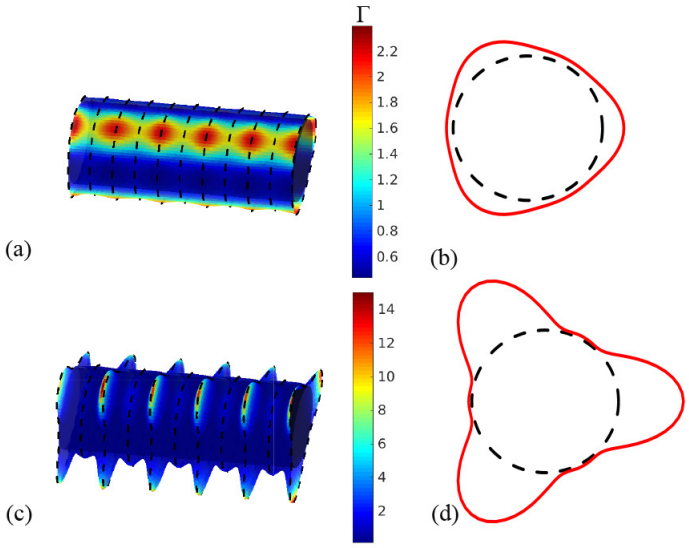

Figure 3.3: (a, c) Free-surface profiles and surfactant distributions in the zero-gravity case with $h_0 = 0.03162$, $\alpha = 10^{-5}$, $k_y = 2$, $k_\theta = 3$, $S = 20$, $Ma = 0$, and $Pe = 10^5$ at (a) $t = 7 \times 10^3$ and (b) $t = 10^4$. The corresponding free-surface profiles around the cylinder circumference at $y = 0$ are plotted in panels (b) and (d) with red dashed lines. The black dashed lines indicate the cylinder surface. For ease of visualization, the thickness plotted in panels (a-d) is five times larger than the actual value. The spacing between the dashed lines in panels (a) and (c) is 0.5π.

profiles around the cylinder circumference at $y = 0$. In this case, three ridges ($k_\theta = 3$) aligned with the cylinder axis develop at the early stage (Fig. 3.3b) with relatively small axial variations in film thickness (Fig. 3.3a). As more liquid is driven into the ridges by centrifugal forces, the growth of axial perturbations is promoted and each ridge breaks into five droplets ($k_y \times L/2\pi = 5$) in the later stage, as shown in Figs. 3.3c and 3.3d.

Figs. 3.2a, 3.2c, 3.3a, and 3.3c clearly show that the regions where the film is thicker also appear to be the high-concentration (red) regions. Thus, the convective flows triggered by centrifugal forces tend to drive surfactant to the thick-film regions, giving rise to concentration gradients at the free surface. This suggests that when $Ma \neq 0$, the resulting Marangoni stresses will drive liquid away from the thick-film (lower-surface-tension) regions to the thin-film (higher-surface-tension) regions and thus suppress the growth rates of both the angular and axial perturbations. Results from our nonlinear simulations confirm this but are not shown here for brevity.

3.4 Stable speed window ($Ma = 0$) and its disappearance ($Ma \neq 0$)

We now incorporate the effects of gravity to show the presence of a stable speed window when $Ma = 0$, first reported in Ref. [15] (§3.1). Within this window, which occurs at moderate rotation rates, the film stays axially uniform [15]. At low rotation rates, the film is susceptible to the Rayleigh-Taylor (RT) instability and droplets form near the bottom of the cylinder. At high rotation rates, the film is susceptible to the Rayleigh-Plateau (RP) instability and rings form around the cylinder. We also demonstrate here that the presence of Marangoni stresses can cause the stable speed window to disappear.

Following Ref. [15], we consider a rotating cylinder with dimensional radius $R = l_c$ ($Bo = 1$), where $l_c = \sqrt{\sigma_m/\rho g}$ is the capillary length. For a glycerol-water mixture (Table 3.1), the corresponding values are $l_c = R = 0.2$ cm. As in Ref. [15], we perform simulations for a film with mean thickness $h_0 = 0.03162$ and dimensionless viscosity $M = 0.007$ (Table 3.2). The corresponding dimensionless critical rotation rate (Eq. (3.1)) is $W_c = 2.01h_0^2/M = 0.29$ ($\Omega_c = 20$ s^{-1} in dimensional form). Above this rotation rate, a smooth coating can be formed (§3.1). Equations (3.12) and (3.13) are solved with initial condition

$$h(\theta, y, 0) = h_0 \left[1 + \alpha_y \cos\left(\frac{2\pi y}{\lambda}\right)\right], \tag{3.25}$$

which corresponds to an axisymmetric coating with a half-cosine variation in the axial direction. Here, $\alpha_y = 0.001$ is the perturbation amplitude and λ is the wavelength of the perturbation.

Similar to the zero-gravity case, perturbations with wavelength longer than a cutoff value, λ_{cutoff}, grow in amplitude at a given rotation rate, while those with $\lambda < \lambda_{\text{cutoff}}$ decay. Thus, for a given value of W, varying λ in the initial condition allows us to approximately locate the cutoff wavelength. Results of our numerical simulations are shown in Fig. 3.4a, where the red dots denote the largest stable wavelength, and the black triangles denote the smallest unstable wavelength. This stability diagram is in good agreement with that obtained by Evans *et al.* [15].

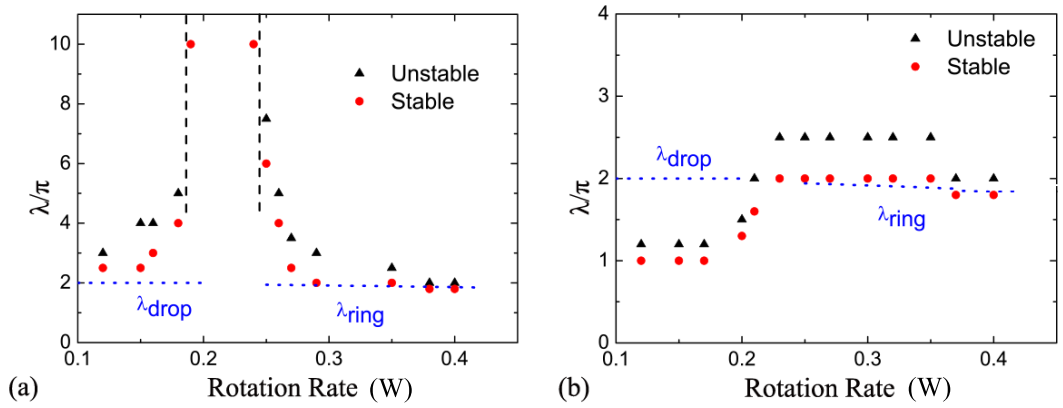

Figure 3.4: Stability diagram for a coating on a rotating cylinder with $Bo = 1$, $h_0 = 0.03162$, $M = 0.007$, and (a) $Ma = 0$ and (b) $Ma = 0.001$ and $Pe = 10^5$. Blue dashed lines denote the cutoff wavelength obtained from a linear stability analysis (for $Ma = 0$). The black dotted vertical lines in panel (a) correspond to $W = 0.186$ and $W = 0.242$.

It is instructive to compare the cutoff wavelengths in Fig. 3.4a with known results for the RT and RP instabilities, as done in Ref. [15]. For an axisymmetric coating on a cylinder, the cutoff wavelength for the RP (ring-type) instability is $\lambda_{\text{ring}} = 2\pi/k^{\text{cutoff}} = 2\pi/\sqrt{1+S}$ (§3.3.1). For a thin layer of liquid underneath a planar substrate (see Appendix B), the cutoff wavelength for the RT (droplet-type) instability is $\lambda_{\text{drop}} = 2\pi/\sqrt{Bo}$. We plot in Fig. 3.4a λ_{ring} and λ_{drop} as functions of W with blue dashed lines.

Fig. 3.4a shows that the cutoff wavelength from the simulations is in good agreement with λ_{ring} in the RP regime (high rotation rates), but is always slightly lager than λ_{drop} in the RT regime (low rotation rates), possibly due to the planar geometry on which λ_{drop} is based. At moderate rotation rates, the cutoff wavelength increases dramatically, and even perturbations with wavelength $\lambda = 10\pi$ (the longest wavelength tested in our simulations) are found to be stable for $0.186 < W < 0.242$, suggesting that axial perturbations are unlikely to grow. The physical mechanisms responsible for this window are discussed in §3.5.

While computational limitations have prevented us from performing a comprehensive parametric study, we speculate that the stable speed window may not exist if gravitational forces become sufficiently strong relative to surface tension forces, which

could happen if Bo or the initial film thickness is too large. Limited simulations performed by Evans *et al.* indicate that an increase in M shifts the stable speed window to lower rotation rates, presumably since a lower rotation rate is required in a more viscous liquid to obtain a film of comparable thickness [15]. This suggests that if M is large enough, the stable speed window may not be present in the range of rotation rates considered. Indeed, the results of some limited simulations we have performed appear consistent with this conjecture.

We now examine the influence of Marangoni stresses and consider a representative case where $Ma = 0.001$ and $Pe = 10^5$. All simulations are started with uniform surface concentration $\Gamma = 1$, and the stability diagram is shown in Fig. 3.4b. Also shown with blue dashed lines are predictions of λ_{ring} and λ_{drop} when $Ma = 0$, since LSA reveals that Marangoni stresses have very little influence on these values (see Appendix B).

In the regime where the RP instability dominates ($W > 0.3$), the corresponding cutoff wavelength is in good agreement with λ_{ring}, similar to the $Ma = 0$ case. In the regime where the RT instability dominates ($W < 0.2$), Marangoni stresses lower the cutoff value to about $\lambda_{\text{ring}}/2$. For all the rotation rates considered in our simulations ($0.1 < W < 0.5$), a minimum unstable wavelength above which the initial perturbations grow in amplitude can always be found. Marangoni stresses can thus cause the stable speed window to vanish. The mechanisms underlying this are discussed in §3.6.

3.5 Surfactant-free case ($Ma = 0$)

As noted in §3.1, although the stable speed window for $Ma = 0$ (§3.4) has been observed, the mechanisms underlying it are still unknown, and one purpose of the present chapter is to understand these mechanisms. In doing so, it is useful to integrate Eq. (A.24) from $z = 0$ to $z = h$ to study the axial flux, Q_y, given by

$$Q_y^{G/\Omega} = \frac{1}{3}h^3\left(\left(W^2 - \sin\theta\right)\frac{\partial h}{\partial y}\right), \tag{3.26}$$

$$Q_y^{\sigma} = \frac{1}{3Bo}h^3\left(\left(\frac{\partial h}{\partial y} + \frac{\partial^3 h}{\partial y^3}\right) + \frac{\partial}{\partial y}\left(\frac{\partial^2 h}{\partial \theta^2}\right)\right), \tag{3.27}$$

$$Q_y = Q_y^{G/\Omega} + Q_y^{\sigma}, \tag{3.28}$$

where $Q_y^{G/\Omega}$ denotes the contribution from centrifugal forces (term with W^2) and gravitational forces (term with $\sin\theta$), and Q_y^{σ} denotes the contribution from surface-tension forces. Positive values of Q_y correspond to an axial flux in the positive y-direction (Fig. 3.1a). We investigate the axial flux in both the low-W region (where the RT instability dominates) and the high-W region (where the RP instability dominates).

3.5.1 Rayleigh-Taylor instability

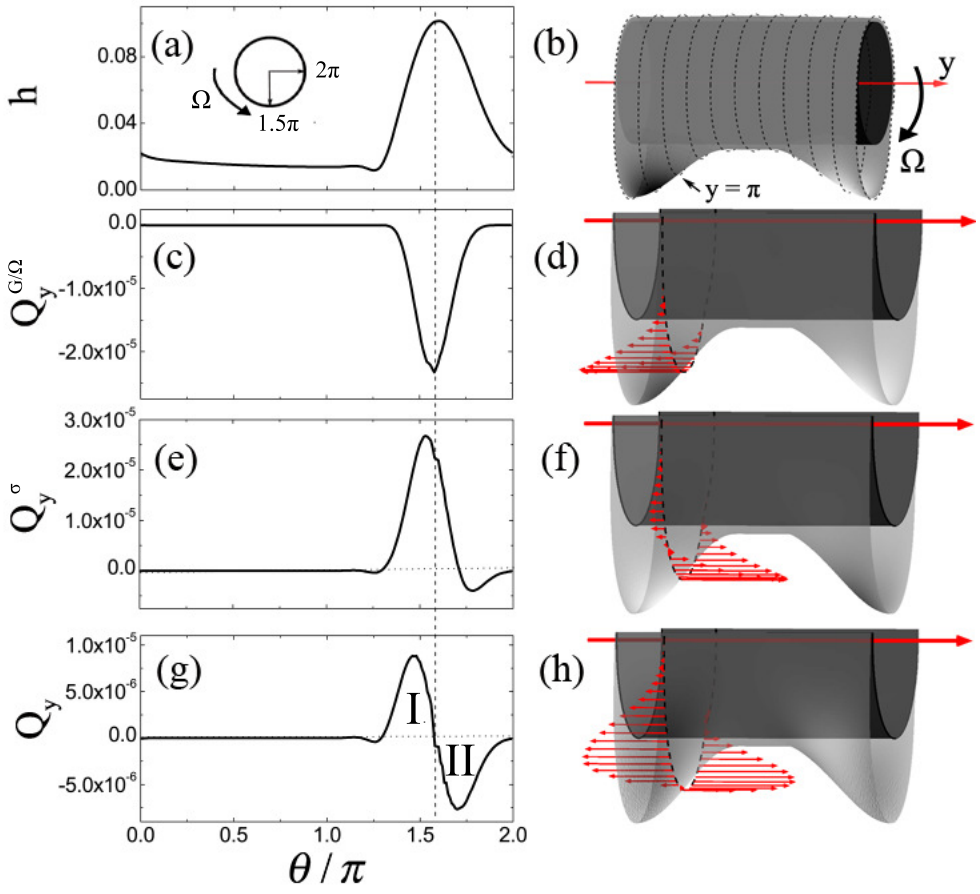

Figure 3.5: (a) Film thickness and (c, e, g) axial flux along the cylinder circumference at $y = \pi$ and $t = 4 \times 10^6$ with $L = 5\pi$, $Bo = 1$, $h_0 = 0.03162$, $M = 0.007$, $Ma = 0$, and $W = 0.1$. The corresponding free-surface profiles are shown in panels (b), (d), (f), and (g), where the thickness plotted is five times larger than the actual value for ease of visualization. Red arrows indicate the direction and strength of the axial flux at $y = \pi$.

In the regime where the RT instability dominates (left side of the stable speed window in Fig. 3.4a), the film sags due to gravity-driven drainage and forms a ridge of liquid aligned with the cylinder axis [15]. This ridge is unstable and tends to break up into droplets underneath the cylinder. These droplets grow in size until the coating reaches a steady state. We pick a representative rotation rate $W = 0.1$ (in the RT-instability region in Fig. 3.4a), and perform simulations with a layer of nearly uniform thickness with random noise added,

$$h(\theta, y, t = 0) = h_0(1 + 0.01[R_{\theta,y} - \frac{1}{2}]), \tag{3.29}$$

where $R_{\theta,y}$ is a randomly chose value between 0 and 1 for each value of θ and y.

The steady film-thickness profile at $t = 4 \times 10^6$ and the corresponding axial flux and its contributions are plotted in Figs. 3.5a, 3.5c, 3.5e, and 3.5g, respectively, as functions of angular position at $y = \pi$. Fig. 3.5b shows the full free-surface profile observed from the cylinder front. Figs. 3.5d, 3.5f, and 3.5h show the same free-surface profile but only at the lower half of the cylinder, where large variations in free-surface curvature occur.

As shown in Fig. 3.5b, two distinct half droplets of almost the same size develop near the bottom at the two ends of the cylinder. The corresponding film thickness around the circumference of the cylinder at $y = \pi$ is shown in Fig. 3.5a. The thickness profile on the downward-moving side of the droplet ($\pi < \theta < 1.5\pi$) is steeper than that on the upward-moving side of the droplet ($1.5\pi < \theta < 2\pi$) due to the effects of cylinder rotation, and the thickness reaches its maximum (denoted with a dashed line) slightly above the bottom of the cylinder ($\theta = 1.5\pi$).

For $W = 0.1$, the centrifugal term in Eq. (3.26) is negligible relative to the gravitational term, and the flux arising due to gravity ($Q_y^{G/\Omega}$ shown in Figs. 3.5c and 3.5d) is negative around cylinder circumference, indicating that gravitational forces tend to drive liquid to the thick-film regions (i.e., droplets). The strongest flux occurs at the point of maximum film thickness, which also corresponds to the point where gravitational forces acting on the liquid are the strongest.

The flux arising due to surface-tension forces (Q_y^{σ} shown in Figs. 3.5e and 3.5f) is positive on the downward-moving side of the droplet, but changes sign in a small region on the upward-moving side. This suggests that surface tension acts mainly as a stabilizing force, driving liquid to the thin-film region (i.e. middle of the cylinder). The

strongest flux occurs on the downward-moving side of the droplet, slightly ahead of the point of maximum film thickness.

The resulting total flux ($Q_y = Q_y^{G/\Omega} + Q_y^{\sigma}$ shown in Figs. 3.5g and 3.5h) changes sign at the point of maximum film thickness, and is positive on the upward-moving side of the droplet and negative on the downward-moving side. This implies that gravitational forces dominate on the upward-moving side, while surface-tension forces dominate on the downward-moving side. The competition between them determines whether the initial axial perturbation will grow or decay. The areas of region I and II marked in Fig. 3.5e, A_I, and A_{II}, measure how much flux crosses over the $y = \pi$ plane on the upward-moving side and on the downward-moving side, respectively. For $W = 0.1$, our numerical results (not shown here for brevity) reveal that A_{II} is always greater than A_I during the early transient stage , so droplets tend to grow in size under the action of gravity until the coating reaches a steady state (Fig. 3.5b) where $A_I = A_{II}$.

An increase in the value of W causes a decrease in the size of the ridge [10, 46], which corresponds to a smaller amount of liquid inside the ridge and therefore weaker destabilizing gravitational forces acting on the ridge. In this case, the flux arising due to gravity-driven drainage is not strong enough to compensate the liquid loss in the droplet caused by surface-tension-induced flow. This explains why the coating becomes more stable (larger cutoff wavelength) to axial perturbations with an increase in the rotation rate (near $W = 0.186$ in Fig. 3.4a) in the region where the RT instability dominates.

Further calculations reveal that $(h_{\theta\theta})_y$ is the dominant term in Eq. (3.27); this term arises from *both* angular and axial variations in the angular curvature. To understand why the effects of surface tension are especially strong on the downward-moving side of the droplet (Figs. 3.5e and 3.5f), we plot in Fig. 3.6 h and $h_{\theta\theta}$ for $\pi < \theta < 2.5\pi$ (marked in Fig. 3.6a) at different positions along the cylinder axis for the simulation shown in Fig. 3.5. We choose the region $\pi < \theta < 2.5\pi$ because large variations in h and $h_{\theta\theta}$ occur in this region.

For $y = 0$, $h_{\theta\theta}$ (red dashed line in Fig. 3.6a) is almost zero near the cylinder top ($2\pi < \theta < 2.5\pi$) where the film is very thin due to gravity-driven drainage. In the thick-film region ($1.25\pi < \theta < 2\pi$), $h_{\theta\theta}$ decreases on the downward-moving side of the droplet ($1.25\pi < \theta < 1.5\pi$), increases on the upward-moving side ($1.5\pi < \theta < 2\pi$), and reaches both its maximum and minimum on the downward-moving side.

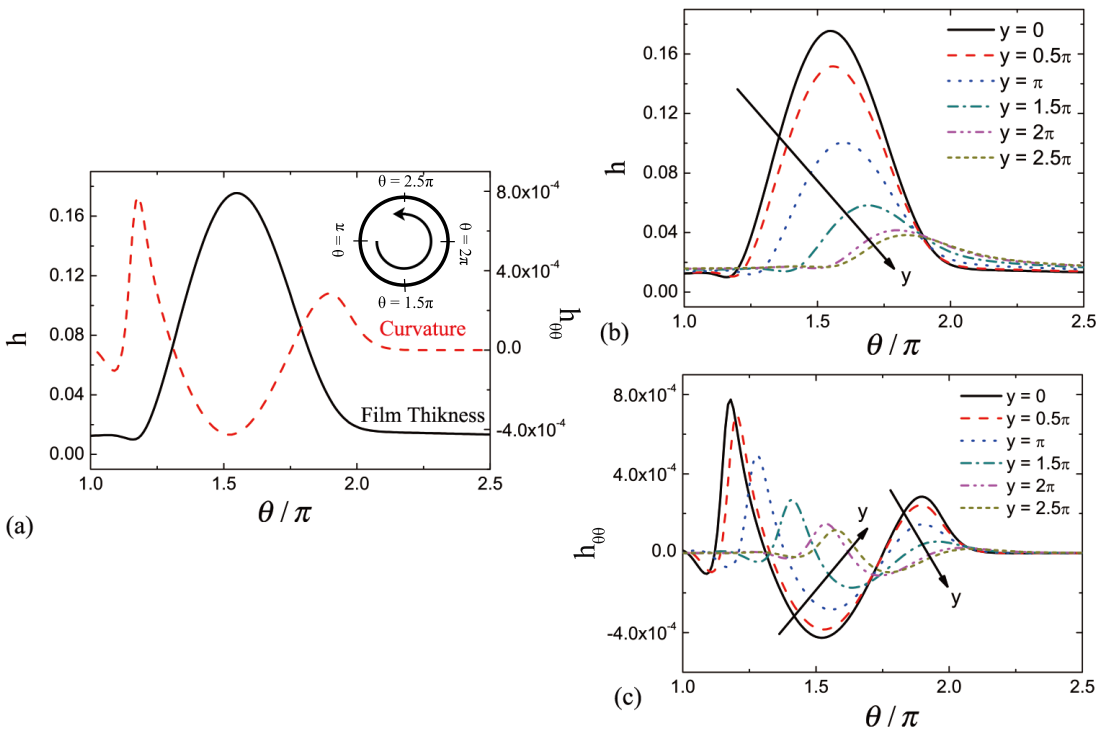

Figure 3.6: Film thickness (h) and its second derivative in the angular direction ($h_{\theta\theta}$) at (a) $y = 0$ and (b, c) at other values of y with $Bo = 1$, $h_0 = 0.03162$, $M = 0.007$, $L = 5\pi$, $Ma = 0$, and $W = 0.1$ at $t = 4 \times 10^6$.

Fig. 3.6b shows that the maximum film thickness around cylinder circumference at a given value of y decreases with an increase in y (closer to the middle of the cylinder), since gravitational forces draw liquid to both ends of the cylinder ($y = 0$). The increase in y also causes the point of maximum thickness to rise higher (larger θ). This phenomenon can be explained by noticing that the point of maximum thickness is determined by the interplay between viscous drag and gravity. A smaller maximum thickness corresponds to weaker gravitational forces there, and as a result, viscous-drag forces push the point of maximum thickness upward, closer to the cylinder symmetry plane ($\theta = 0$).

Since the minimum value of $h_{\theta\theta}$ occurs near the point of maximum thickness (Fig. 3.6a), the location of this minimum also rises higher with an increase in y (Fig. 3.6c). As a result, the value of $h_{\theta\theta}$ increases with an increase in y (yielding a positive value

of $(h_{\theta\theta})_y$) on the downward-moving side of the droplet ($1.25\pi < \theta < 1.75\pi$), while it decreases (yielding a negative value of $(h_{\theta\theta})_y$) in a small region on the upward-moving side ($1.75\pi < \theta < 2\pi$). The variation in $h_{\theta\theta}$ is more significant on the downward-moving side than elsewhere, and this gives rise to a strong flux there in the positive y-direction (Fig. 3.5e). This flux stabilizes the coating by driving liquid back to the middle of the cylinder.

3.5.2 Rayleigh-Plateau instability

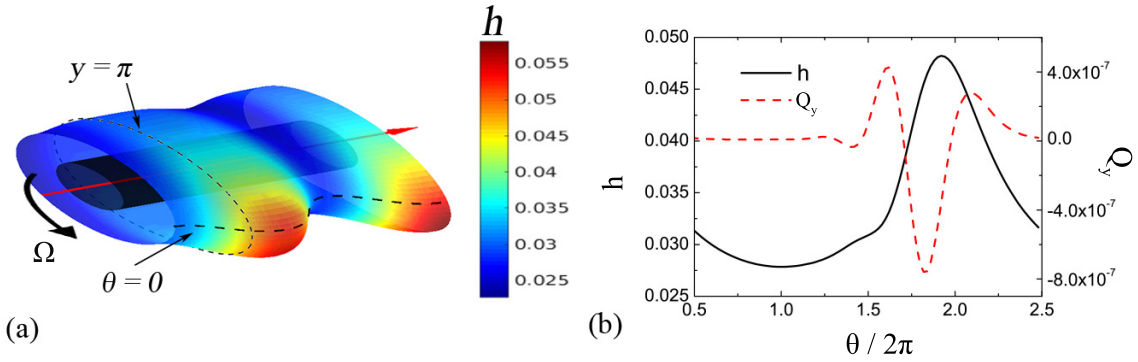

Figure 3.7: (a) Free-surface profile at $t = 4 \times 10^6$ with $L = 5\pi$, $Bo = 1$, $h_0 = 0.03162$, $M = 0.007$, $Ma = 0$, and $W = 0.3$. (b) Film-thickness and total axial flux (Q_y) at $y = \pi$ (marked in panel a). For ease of visualization, the thickness plotted in panel (a) is 50 times larger than the actual value.

We now turn to the regime where the RP instability dominates (right side of the stable speed window in Fig. 3.4a). In this regime, a Moffatt-type smooth coating, which is thicker on the upward-moving side of the cylinder and thinner on the downward-moving side, may break up into ring-shaped liquid bulges wrapped around the cylinder. Simulations similar to those described in §3.5.1 indicate that these rings tend to slowly shift along the cylinder axis, and as a consequence, we are unable to find steady states in this regime. For a representative case where $W = 0.3$, we show in Fig. 3.7 the free-surface profile, and the film thickness and axial flux (Q_y) at $y = \pi$, at a relatively late time ($t = 4 \times 10^6$).

Fig. 3.7a shows the appearance of one full ring (located near the middle of the cylinder) and one half ring (located near the end of the cylinder). These rings are

nonaxisymmetric, in contrast to the zero-gravity case (Fig. 3.2a), and are much thicker on the upward-moving side of the cylinder (dark red region). In this regime, centrifugal forces play a more significant role (relative to gravity) in the axial flux (Eq. (3.26)), and they are especially strong in the rings since more liquid is located there. Liquid is drawn from the surrounding areas to the rings, and as a result, the coating is destabilized.

There are three terms in the surface-tension contribution to the axial flux (Eq. (3.27)). The first term, h_y, represents axial variations in the angular curvature, and gives rise to surface-tension forces that tend to minimize area. As a result, liquid is driven to the rings, which in turn strengthens the centrifugal forces there. The second term, h_{yy}, represents axial variations in axial curvature (h_{yy}), and the third term, $(h_{\theta\theta})_y$, arises from both angular and axial variations in the angular curvature. The latter two terms give rise to surface-tension forces that tend to smooth out curvature gradients at the free surface and thus stabilize the coating. Note that the $(h_{\theta\theta})_y$ term does not exist in the standard RP instability where the film is axisymmetric. Analysis of our results indicates that this term dominates the other two surface-tension terms, similar to what is observed in the regime where the RT instability dominates (§3.5.1).

Fig. 3.7b shows that the total axial flux (red dashed line) at $y = \pi$ is negative in a small region slightly ahead of the point of maximum film thickness, indicating that stabilizing surface-tension forces are stronger than destabilizing centrifugal forces in this region, driving liquid away from the ring (in the negative y-direction). However, centrifugal forces dominate elsewhere and the resulting value of $\int_0^{2\pi} Q_y d\theta$ is positive for the case shown in Fig. 3.7b, leading to growth of the rings. A decrease in the value of W weakens the flux triggered by centrifugal forces and thus causes the coating to be more stable to axial perturbations. This explains the significant increase in the cutoff wavelength as W is decreased to a value of 0.242 (Fig. 3.4a).

We now explain the mechanism behind the stable speed window shown in Fig. 3.4a. For moderate cylinder rotation rates ($0.186 < W < 0.242$), the liquid film stays axially uniform, which leads to $Q_y = 0$. Based on the results shown in Figs. 3.5 and 3.7, we conclude that surface-tension forces arising due to the term $(h_{\theta\theta})_y$ will smooth out any small perturbations in the axial direction since both gravitational forces (weak due to small ridge size) and centrifugal forces (weak due to small rotation rate) are not able to continuously draw liquid to the droplets or rings in this regime. In the following section,

we will discuss how the presence of insoluble surfactant causes this stable speed window to disappear.

3.6 Influence of surfactant ($Ma \neq 0$)

Gradients in surfactant concentration at the free surface will lead to Marangoni stresses that modify both the RT and RP instabilities. As a consequence, the stable speed window in Fig. 3.4a disappears (Fig. 3.4b). We perform simulations similar to those described in §3.5 to understand the reasons for this disappearance.

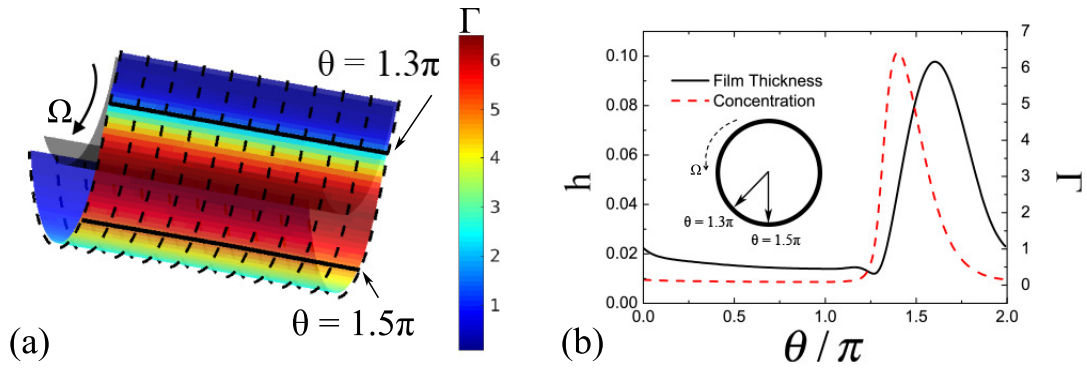

Figure 3.8: (a) Free-surface and concentration profiles with $Bo = 1$, $h_0 = 0.03162$, $L = 5\pi$, $M = 0.007$, $Ma = 0$, $Pe = 10^5$, and $W = 0.1$ at $t = 1 \times 10^6$. (b) Corresponding film thickness (black solid line) and concentration (red dashed line) at $y = 0$. For ease of visualization, the thickness plotted in panel (a) is five times larger than the actual value.

3.6.1 Rayleigh-Taylor instability

3.6.1.1 Surfactant concentration distribution

In the regime where the RT instability dominates (left side of Fig. 3.4b), it is useful to first examine the surfactant concentration distribution in the absence of Marangoni stresses. We again choose a representative rotation rate of $W = 0.1$.

For $W = 0.1$ and $Ma = 0$, the time-evolution of surfactant concentration follows three distinct stages. We show in Figs. 3.8 and 3.9 the corresponding free-surface

profiles and concentration distributions on the downward-moving side of the cylinder, where the surfactant concentration reaches its maximum.

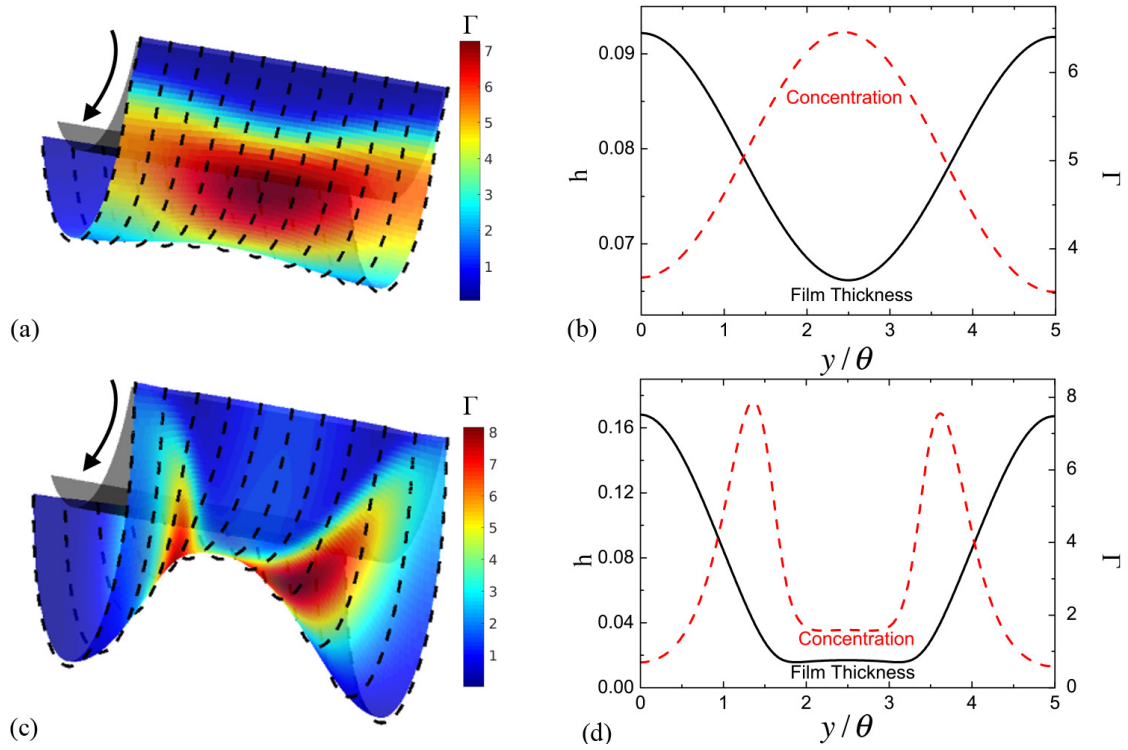

Figure 3.9: (a,c) Free-surface and concentration profiles, and film-thickness (black solid lines in panels (b) and (d)) and concentration (red dashed lines in panels (b) and (d)) at $\theta = 1.5\pi$ with $Bo = 1$, $h_0 = 0.03162$, $M = 0.007$, $Ma = 0$, $Pe = 10^5$, $L = 5\pi$, and $W = 0.1$ at (a,b) $t = 2 \times 10^6$and (c,d) $t = 4 \times 10^6$. For ease of visualization, the thickness plotted in panels (a) and (c) is five times larger than the actual value.)

Due to the initial gravity-driven drainage, surfactant tends to accumulate at the bottom of the cylinder in a liquid ridge with little concentration variation in the axial direction (red region in Fig. 3.8a). The corresponding film thickness and concentration at $y = 0$ are shown in Fig. 3.8b. Surfactant concentration increases significantly on the downward-moving side of the ridge ($1.3\pi < \theta < 1.5\pi$), and reaches its maximum several degrees below the point of maximum thickness.

As axial perturbations start to grow in amplitude (Fig. 3.9a), axial variations in both film thickness and surfactant concentration become significant, so we plot in Fig.

3.9b the film-thickness and concentration along the cylinder axis at $\theta = 1.5\pi$ (marked in Fig. 3.8a). Fig. 3.9b shows that film thickness and surface concentration evolve out of phase: liquid is driven to the ends of the cylinder forming two half droplets at $y = 0$ and $y = 5\pi$, while surfactant is driven to the middle of the cylinder, giving rise to a high-concentration region in the thin-film area ($y = 2.5\pi$). This happens because the region of high surfactant concentration in Fig. 3.8a ($1.3\pi < \theta < 1.5\pi$) occurs where the axial flux drives liquid to the middle of the cylinder (similar to the case shown in Fig. 3.5). As in §3.5.1, the negative axial flux arises because the contribution from surface-tension is stronger than the contribution from gravity and centrifugal forces. Again, the term $(h_{\theta\theta})_y$ dominates the surface-tension contribution.

The steady free-surface and concentration profiles are shown in Fig. 3.9c. The corresponding film thickness and concentration at $y = 1.5\pi$ are shown in Fig. 3.9d. As the two half-droplets grow in size, a satellite droplet forms in the middle of the cylinder (small bump in between $2\pi < y < 3\pi$ in Fig. 3.9d). This triggers an additional capillary flow that drives surfactant away from the middle of the cylinder. As a result, the surfactant concentration in the middle of the cylinder decreases dramatically and forms maxima in between the main droplets and the satellite droplet.

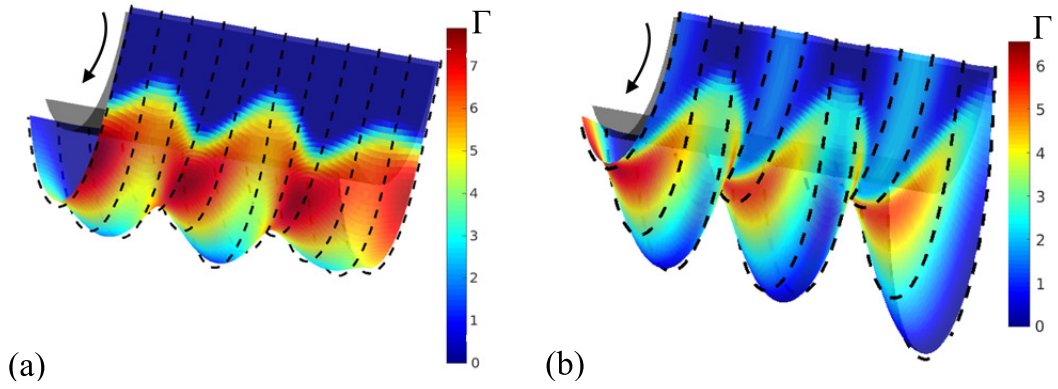

Figure 3.10: Free-surface and surfactant concentration profiles with $Bo = 1$, $h_0 = 0.03162$, $L = 5\pi$, $M = 0.007$, $Ma = 0.001$, $Pe = 10^5$, and $W = 0.1$ at (a) $t = 8.5 \times 10^4$ (b) $t = 2.5 \times 10^5$ (steady state). For ease of visualization, the thickness plotted in this figure is five times larger than the actual value.

3.6.1.2 Marangoni stresses

We now include the influence of Marangoni stresses by performing simulations with $Ma = 0.001$. Figs. 3.10a and 3.10b show the free-surface and surfactant concentration profiles on the downward-moving side of the cylinder during the transient stage and at steady state, respectively. Notably, a third droplet forms in the middle of the cylinder during the transient stage, corresponding to a decrease in the spacing between droplets relative to the zero-Ma case (Fig. 3.9c). The third droplet grows in size together with the two half droplets at two ends. The decrease in the spacing between droplets when $Ma \neq 0$ is consistent with the decrease in the cutoff wavelength in the RT regime shown in Fig. 3.4.

The results shown in Fig. 3.9 can be used to understand the growth of the third droplet. The accumulation of surfactant in between the two main droplets (Fig. 3.9b) lowers the local surface tension, and the resulting Marangoni stresses then drive liquid away from that area to those droplets. The surfactant concentration in the middle of the cylinder becomes especially low when the satellite droplet forms (Fig. 3.9d). The resulting Marangoni stresses then drive flow to the middle of the cylinder, leading to the formation of a third droplet (Fig. 3.10). The flows driven by the Marangoni stresses enhance the growth rate of the droplets, so steady state is reached sooner.

The Marangoni flows also lead to disappearance of the stable speed window (Fig. 3.4). Recall that the term $(h_{\theta\theta})_y$ drives flow to the middle of the cylinder and thus opposes the RT instability, leading to the large increase in the cutoff wavelength as the rotation rate is increased (Fig. 3.4a). The Marangoni stresses initially drive flow toward the ends of the cylinder and thus oppose the flow driven by the $(h_{\theta\theta})_y$ term. As a consequence, this term becomes much less effective at opposing the RT instability and the stable speed window disappears (Fig. 3.4b).

3.6.2 Rayleigh-Plateau instability

In the regime where the RP instability dominates (right side of Fig. 3.4b), we again choose a representative rotation rate of $W = 0.1$. Fig. 3.11a shows the free-surface and surfactant concentration profiles for the simulation shown in Fig. 3.7 where $Ma = 0$. The corresponding film thickness and surfactant concentration along the cylinder axis

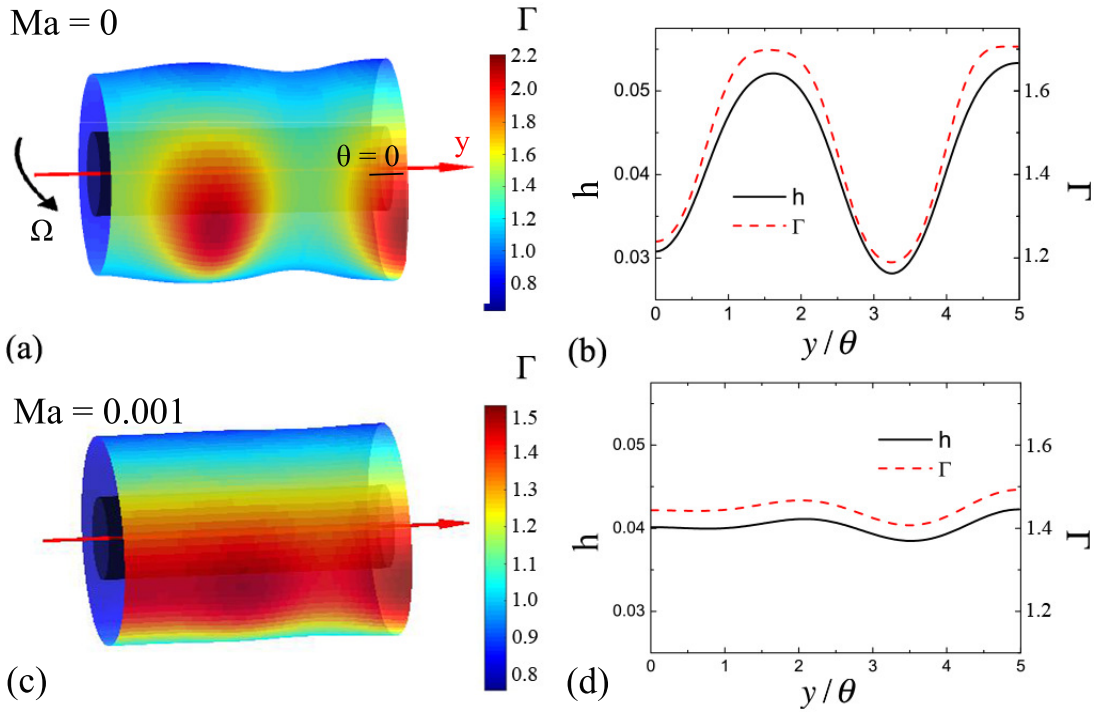

Figure 3.11: (a, c) Free-surface and surfactant concentration profiles for two different values of Ma with $Bo = 1$, $h_0 = 0.03162$, $L = 5\pi$, $M = 0.007$, $Pe = 10^5$, and $W = 0.3$ at $t = 4 \times 10^6$. For ease of visualization, the thickness plotted in panels (a) and (c) is 50 times larger than the actual value. (b, d) Corresponding film thickness (black solid lines) and concentration (red dashed lines) at $\theta = 0$ (marked in panel (a)).

at $\theta = 0$ are shown in Fig. 3.11b. The case where $Ma = 0.001$ is also considered, and results are shown in Figs. 3.11c and 3.11d for comparison.

For $Ma = 0$, the liquid film breaks into one-and-a-half rings wrapped circumferentially around the cylinder due to the RP instability (Fig. 3.11a). Surfactant tends to accumulate on the upward-moving side of the rings (red regions in Fig. 3.11a). Recall that when the rotation rate is smaller, surfactant tends to accumulate in a liquid ridge at the cylinder bottom (Fig. 3.8). As the rotation rate is increased, the ridge and point of maximum concentration shift to the upward-moving side of the cylinder [46]. As the ridge breaks up due to the RP instability, liquid and surfactant get driven into the rings, and as a consequence, the film thickness and surfactant concentration are in phase at $\theta = 0$, which is on the upward-moving side (Fig. 3.11b).

For $Ma = 0.001$, the gradients in film thickness and surfactant concentration are much smaller than those when $Ma = 0$ case and the coating stays almost axially uniform (Figs. 3.11c and 3.11d). Since surfactant tends to accumulate at the surface of the rings, the resulting Marangoni stresses drive flow from the rings to the thin-film areas, leading to the more uniform coating and concentration profile. In addition, these Marangoni flows slow the growth of the instability but do not appear to change the spacing between the rings.

The Marangoni flows again lead to disappearance of the stable speed window (Fig. 3.4). Recall that the term $(h_{\theta\theta})_y$ drives flow to the middle of the cylinder and thus opposes the RP instability (§3.5.2), leading to the large increase in the cutoff wavelength as the rotation rate is decreased (Fig. 3.4a). Because the Marangoni flows lead to a smoother free surface, the $(h_{\theta\theta})_y$ term is much less effective at opposing the RP instability and the stable speed window disappears (Fig. 3.4b).

3.7 Flow visualization experiments

To complement our numerical simulations, we have performed some flow visualization experiments. We first describe the experimental setup, and then present and discuss the results.

3.7.1 Experimental setup

The experimental apparatus is shown in Fig. 3.12. A smooth steel cylinder is mounted in a container whose front gate can be lifted, and the cylinder is rotated using an electric motor. In all of our experiments, liquid was first coated on the cylinder by rotating it with the container partially filled. The glass gate was then quickly lifted to drain the liquid from the container into a tray, leaving liquid on the rotating cylinder. Excess liquid would immediately drip off, which sometimes triggered visible axial variations in coating thickness or even dry patches. As a result, we sometimes had to repeat this process until a sufficiently uniform initial coating was obtained.

The steel cylinder has radius $R = 0.2$ cm, which is consistent with the value used in our simulations (Table 3.1), and length $L = 30$ cm. The liquid is a glycerol/water mixture (96 wt% glycerol) having surface tension $\sigma_0 = 66$ dyn/cm, density $\rho = 1.23$

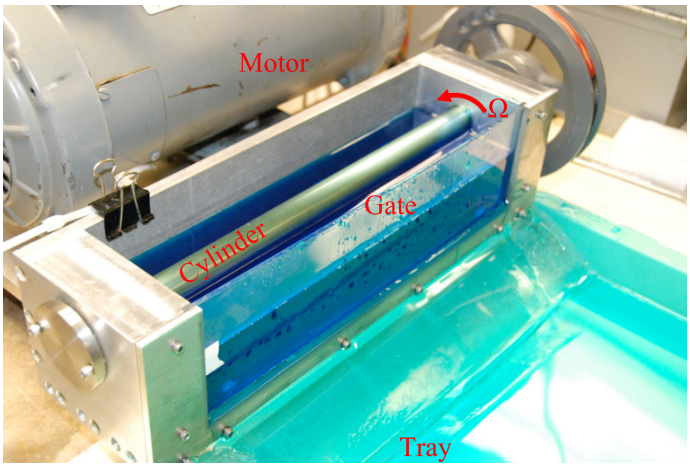

Figure 3.12: Experimental apparatus. The steel cylinder has length $L = 30$ cm and radius $R = 0.2$ cm.

g/cm^3, and viscosity $\mu = 2.6$ P. To study the influence of surfactant, we use sodium dodecyl sulfate (SDS; Thermo Scientific). For a bulk concentration $c = 0.1$ wt%, the surface tension drops to 50 dyn/cm, while the density and viscosity remain unchanged. An increase in c further reduces surface tension, suggesting that $c = 0.1$ is still smaller than the critical micelle concentration.

The values of key dimensionless parameters in the experiments are summarized in Table 3.3. Note that Bo in our experiments is around unity, consistent with the simulations. The dimensionless viscosity in our experiments ($M = 0.74$) is about 100 times higher than that in our simulations ($M = 0.007$) so that a much thicker coating can be maintained on the cylinder for ease of flow visualization. As noted in §3.4, if M or the initial film thickness are too large, a stable speed window may not be observed. In the experiments, the smallest rotation rates ($W \sim$ 0.03-0.06) were comparable to those in the simulations, while the largest rotation rates ($W \sim$ 0.2-0.3) were smaller. The Marangoni number in our experiments ($Ma = 0.35$) is much larger than that in our simulations ($Ma = 0.001$), so we expect to observe much stronger Marangoni effects in the experiments.

Table 3.3: Dimensionless problem parameters

	M	Bo	Ma	W (corresponding dimensional rotation rate)
Surfactant-free solution	0.74	0.73	0	0.056 $\sim$ 0.28 (4.0 rad/s $\sim$ 20.0 rad/s)
Surfactant-laden solution	0.74	1.0	0.35	0.028 $\sim$ 0.22 (2.0 rad/s $\sim$ 15.7 rad/s)

3.7.2 Results and discussion

For the surfactant-free solution (which corresponds to $Ma = 0$), images of the free surface on the upward-moving side of the cylinder at several different times are shown in Fig. 3.13 for $W = 0.056$ and $W = 0.22$.

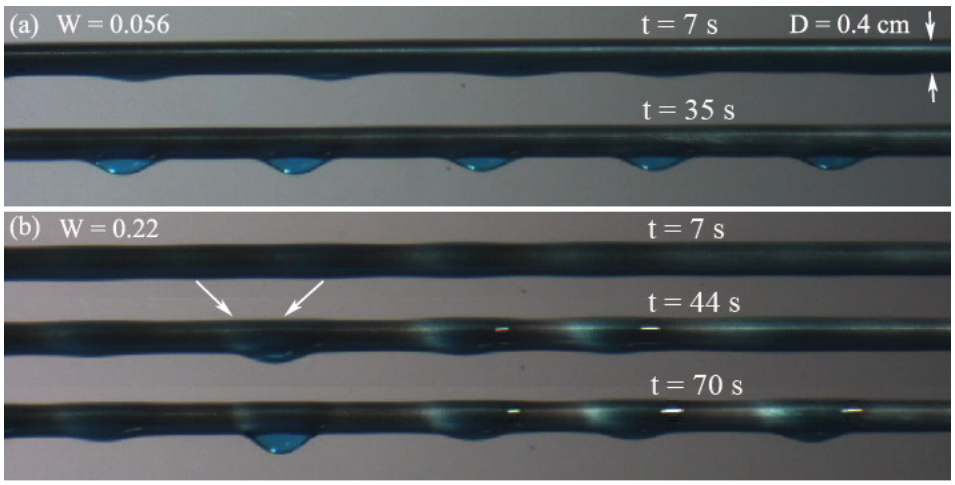

Figure 3.13: Images of the free surface on the upward-moving side of the cylinder for the surfactant-free solution at several different times for (a) $W = 0.056$ and (b) $W = 0.22$ with $Bo = 0.73$, $M = 0.74$, and $Ma = 0$.

For $W = 0.056$ (Fig. 3.13a), axial perturbations grow in amplitude due to gravity, and become visible near the underside of the cylinder within about 7 s (1 s corresponds to approximately 100 dimensionless time units). At later times, the coating breaks up into small droplets which are approximately evenly spaced along the cylinder axis, similar to the simulation result shown in Fig. 3.5 for the Rayleigh-Taylor instability. The sizes of the droplets reach a steady state within about 35 s, with the droplets tending to slowly shift along the cylinder axis.

With an increase in rotation rate to $W = 0.22$, there is a transition from the Rayleigh-Taylor instability to the Rayleigh-Plateau instability (Fig. 3.13b). Initial

perturbations grow into small ring-shaped liquid bulges under the action of centrifugal forces, similar to the simulation result shown in Fig. 3.7 for the Rayleigh-Plateau instability. These bulges are not stable, and adjacent ones tend to merge to form a droplet (marked by arrows in Fig. 3.13b). We do observe some shifting of rings along cylinder axis in our simulations (§3.5.2), but are not able to run simulations for a long enough time to observe merging. The formation of large bulges enhances the strength of gravitational forces and appears to draw liquid from the surrounding areas, which leads to a droplet. The sizes of the rings and droplet reach a steady state at a later time ($\sim$ 70 s) compared to the low-rotation rate case (Fig. 3.13a).

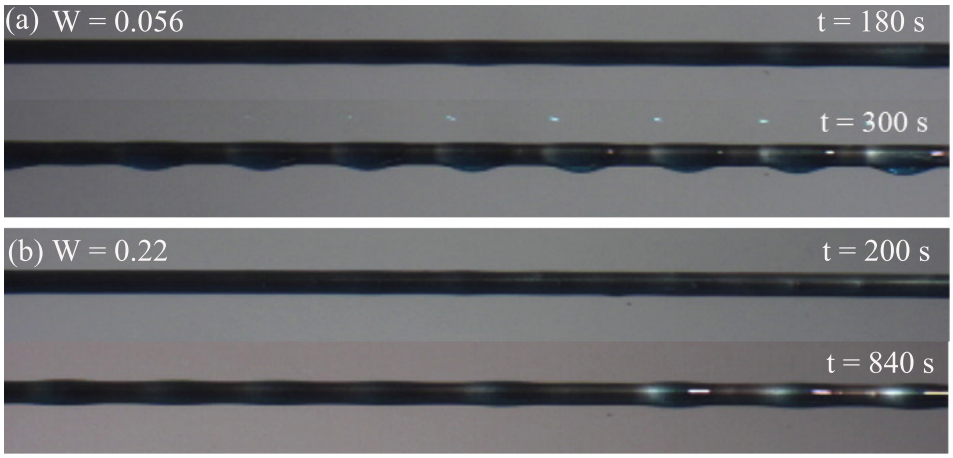

Figure 3.14: Images of the free surface on the upward-moving side of the cylinder for the surfactant-laden solution at several different times for (a) $W = 0.056$ and (b) $W = 0.22$ with $Bo = 1.0$, $M = 0.74$, and $Ma = 0.35$.

For the surfactant-laden solution (which corresponds to $Ma = 0.35$), images of the free surface on the upward-moving side of the cylinder at several different times are shown in Fig. 3.14 for $W = 0.056$ and $W = 0.22$. Similar to the surfactant-free case, droplets form at the lower rotation rate (Fig. 3.14a) while rings form at the higher rotation rate (Fig. 3.14b). However, the time required for axial perturbations to become visible is much longer compared to the surfactant-free case for both rotation rates. As a consequence, the sizes of the droplets and rings reach steady state at much later times, $\sim$ 5 min. for the droplets and $\sim$ 10 min. for the rings. In addition, the shifting and merging of rings and droplets seen in the surfactant-free case (Fig. 3.13b) appears to

be considerably suppressed when surfactant is present.

The slower development of free-surface perturbations at the higher rotation rate when $Ma \neq 0$ is consistent with the simulation results in §3.6.2 for the RP instability. However, the simulation results for the RT instability in §3.6.2 predict a faster development of free-surface perturbations when $Ma \neq 0$, in contrast to the experimental observations at the lower rotation rate. We believe that this situation arises because the initial coating in the experiments is non-axisymmetric, in contrast to the initial condition used in the simulations. The non-axisymmetric initial condition in the experiments arises due to liquid dripping. When surfactant is present, the resulting Marangoni stresses tend to suppress this dripping [31], leading to a slower development of free-surface perturbations. Nevertheless, this slower development created by surfactant may be very useful for applications, allowing for longer time period to solidify the coating before free-surface perturbations become prominent.

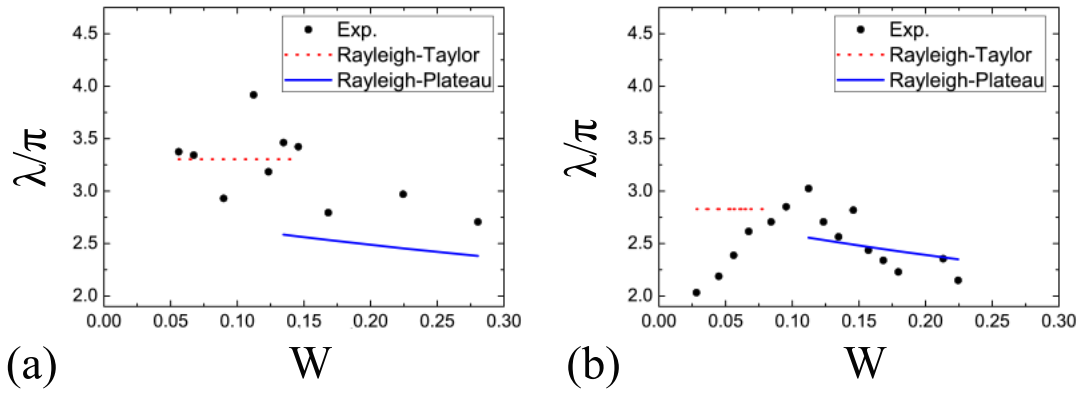

Figure 3.15: Most dangerous wavelength at different rotation rates with $M = 0.74$ and (a) $Bo = 0.73$ and $Ma = 0$ and (b) $Bo = 1.0$ and $Ma = 0.35$. Red dashed lines and blue solid lines indicate the most-dangerous wavelength obtained from linear stability analysis.

We have also measured the average spacing between the free-surface bulges as soon as they become visible over a range of rotation rates (Fig. 3.15). This spacing should correspond the most-dangerous wavelength, and is shown in non-dimensional form (scaled with R) in Fig. 3.15. Each point in Fig. 3.15 represents a mean of up to four measurements. For the surfactant-free solution, the largest deviation from the mean value

of the most dangerous wavelength was 0.3π, whereas for the surfactant-free solution, the largest deviation from the mean was much smaller, 0.05π, presumably due to the reduced shifting and merging of rings and droplets. Also shown in Fig. 3.15 are predictions of the most-dangerous wavelength from LSA for the RT and RP instabilities (see Appendix B and §3.4), yielding plots similar to those for the cutoff wavelength shown in Fig. 3.4.

The most-dangerous wavelengths of the RT and RP instabilities in the surfactant-free case are [15]

$$\text{RT instability:} \quad \lambda^{\star}_{\text{drop}} = \frac{2\sqrt{2}\pi}{\sqrt{Bo}}, \qquad \text{RP instability:} \quad \lambda^{\star}_{\text{ring}} = \frac{2\sqrt{2}\pi}{1+S}, \tag{3.30}$$

where $S = WBo^2$ is the Weber number defined in §3.3. When $Ma \neq 0$, analytical expressions for these quantities are not available, but calculations show that surfactant has only a very minor influence (see Appendix B). We thus use the expressions given in Eq. (3.30) even when $Ma \neq 0$, similar to Fig. 3.4.

For the surfactant-free solution (Fig. 3.15a), the average spacing oscillates about $\lambda^{\star}_{\text{drop}}$ (red dotted line) at low rotation rates, and is always larger than $\lambda^{\star}_{\text{ring}}$ (blue solid line) at high rotation rates. The discrepancy at high rotation rates is consistent with the merging of the rings (Fig. 3.14b), which lowers the number of rings along cylinder axis and causes the average spacing to increase. No stable speed window is observed, perhaps due to the large value of M and a relatively thick and non-uniform initial film.

For the surfactant-laden solution, (Fig. 3.15b), the average spacing is generally smaller compared to the surfactant-free case. This is consistent with the observation that surfactant lowers the mean surface tension, σ_m (larger Bo), which gives rise to a larger value of Bo and a smaller value of the most-dangerous wavelength (Eq. (3.30)). Again, no stable speed window is observed over the range of rotation rates considered.

When $W = 0.028$, the average spacing measured in our experiments is $\lambda/\pi = 2.0$ (~ 0.4 cm) in the surfactant-laden solution, which is much smaller than $\lambda^{\star}_{\text{drop}}/\pi = 2.8$ calculated using LSA (red dotted line in Fig. 3.15b). With an increase in W, the average spacing increases monotonically in the RT-instability regime and reaches its maximum at $W = 0.12$. The discrepancy between the experimental values and the LSA predictions is consistent with our simulation results, which show that Marangoni stresses lead to the formation of extra droplets along the cylinder axis (Fig. 3.10), which would cause

the average spacing to be smaller than that predicted by the simple RT LSA result. An increase in the rotation rate weakens the effects of gravity, and as a result, the coating becomes more stable to the RT instability. This explains the increase in the average spacing with increasing W in the regime of the RT-instability.

A further increase in W brings the system into the regime of the RP instability. Here, the average spacing decreases as the rotation rate increases, and there is much better agreement between the experimental observations and the LSA predictions relative to the RT regime (blue solid line in Fig. 3.15b). This can be rationalized by recalling that Marangoni stresses suppress the growth rate of the RP instability but do not modify the spacing between rings (§3.6.2). The behavior of the most-dangerous wavelength shown in Fig. 3.15b is analogous to the behavior of the cutoff wavelength shown in Fig. 3.4b, where the cutoff wavelength from the simulations is smaller than the LSA prediction at low rotation rates, but in much better agreement at high rotation rates.

We have also attempted to perform some nonlinear simulations to predict the most dangerous wavelength using an initial film thickness estimated from Eq. (3.1) and experimental observations of Ω_c. However, since the initial film thickness is much larger than that used for the simulations in §3.4-§3.6, large free-surface deformations quickly develop that we cannot accurately resolve, and as a consequence, we are unable to obtain predictions of the most dangerous wavelength from the simulations.

Nevertheless, the results of these flow visualization experiments appear to be qualitatively consistent with predictions from LSA and other behavior observed in our simulations. We note that while the simulations and LSA are for the case of an insoluble surfactant, the surfactant in the experiments is soluble. Nevertheless, it appears that much of what is observed in the experiments can largely be understood by a model that assumes surfactant insolubility, suggesting that surfactant solubility plays a secondary role in these experiments.

3.8 Conclusions

One purpose of this chapter was to determine the physical mechanisms underlying the stable speed window observed by Evans *et al.* [15]. Our simulations show that surface-tension forces arising from both axial and angular variations in the angular curvature

drive flows in the axial direction that tend to smooth out free-surface perturbations. The term responsible for this, $(h_{\theta\theta})_y$, is not present in the standard axisymmetric RP instability or in the RT instability for a film under a planar substrate.

A second purpose of this chapter was to determine how the presence of insoluble surfactant influences three-dimensional thin-liquid-film flow on rotating cylinders. Our simulations show that Marangoni stresses can cause the stable speed window to disappear by driving flows that oppose those arising from the $(h_{\theta\theta})_y$ term. In addition, Marangoni stresses tend to reduce the spacing between droplets at low rotation rates (RT instability regime), and reduce the growth rate of the rings at high rotation rates (RP instability regime). Our results extend those of (i) Weidner [31] to include cylinder rotation, (ii) Evans et al. [15] to include insoluble surfactant, and (iii) Li and Kumar [46] to include axial variations.

Flow visualization experiments yield observations that are qualitatively consistent with LSA predictions and behavior observed in the simulations. Although a stable speed window was not observed, the flow visualizations make clear that surfactants tend to suppress dripping, slow the development of free-surface perturbations, and reduce the shifting and merging of rings and droplets. This may be very useful for applications as it would allow a longer time period to solidify the coating before free-surface perturbations become too large.

While some of the results presented here can readily be understood in terms of the RT and RP instabilities, others appear to arise as a consequence of cylinder rotation. Many objects that need to be coated have a more complex cross-sectional shape, resulting in additional flows that arise due to curvature gradients on the object surface [64]. Nevertheless, the results obtained for the model problem considered here may be useful in understanding many features of the even more complex flows likely to arise is those cases.

Chapter 4

Liquid-film Coating on Topographically Patterned Rotating Cylinders

Abstract - The coating of discrete objects having surface topography is an important step in the manufacturing of a broad variety of products. To develop fundamental understanding of this problem, we study liquid-film flow on rotating cylinders patterned with sinusoidal topographical features. The Stokes equations, augmented with a term accounting for centrifugal forces, are solved in a rotating reference frame using the Galerkin finite-element method (GFEM). A nonlinear evolution equation for the film thickness based on lubrication theory is also solved numerically and its predictions are compared to those from the GFEM calculations. When gravitational effects are negligible and the rotation rate is sufficiently low, liquid accumulates over the pattern troughs before merging to form multiple larger drops (located over troughs) whose number at steady state depends on the topography wavelength and rotation rate. When the rotation rate is sufficiently high, similar merging events occur but liquid accumulates over the pattern crests at steady state. When gravitational forces become significant, it is possible to obtain a coating that closely conforms to the surface topography. The GFEM calculations are in agreement with predictions from the lubrication model provided that

the free-surface curvatures are sufficiently small. For sufficiently large pattern amplitude and film thickness, the GFEM calculations show that recirculation regions inside the troughs can appear and vanish as the cylinder rotates due to the variation of gravitational forces around the cylinder surface. This phenomenon, along with flow reversal over the crests, may strongly influence mixing, mass transport, and heat transport.[1]

[1] This chapter has been published in [63].

4.1 Introduction

The flow of liquid films on discrete objects is encountered in coating processes for products such as biomedical devices, automobiles, and food. Describing the shape of liquid films as they flow over discrete objects is a challenging task due to the complicated geometry of the object, the possible presence of object rotation, non-Newtonian rheology, and the occurrence of phenomena such as Marangoni flows and drying.

Flow of a thin liquid film on a cylinder that rotates about its horizontal axis is a common model problem for studying the coating of discrete objects and has attracted much attention since the pioneering work of Moffatt [9] and Pukhnachev [11]. When the cylinder rotation rate is below a critical value, gravity-driven drainage leads to a drop-like liquid bulge that hangs from the underside of the cylinder and is supported by surface tension [10]. As the rotation rate is increased beyond the critical value, a steady smooth coating can be obtained with a thicker film on the upward-moving side and a thinner film on the downward-moving side [9]. In recent years, different flow regimes in this problem have been extensively investigated both theoretically and experimentally (e.g., [10, 15, 65]).

The lubrication approximation has often been employed in previous studies to simplify the governing equations. Formally, this requires the film thickness to be much smaller than the cylinder radius and the slopes of the liquid-air interface to be small. To overcome these restrictions, Peterson *et al.* [14] used an adaptive finite-element scheme to solve the free-boundary problem involving the full Stokes equations. Their results reveal that the lubrication approximation works quite well even when the film thickness is a significant fraction ($\sim$40%) of the cylinder radius, especially under conditions where the ratio of the gravitational drainage rate to the cylinder rotation rate is not too large. When this ratio becomes too large, liquid shedding can occur and lead to interface shapes that are beyond the reach of lubrication theory.

Although most previous work assumes that the cylinder surface is perfectly smooth, in practice the cylinder surface may be uneven. This unevenness could be caused by surface imperfections or by imposed topographical patterns. The coating of substrates with topography occurs in the manufacturing of microelectronic devices [32], medical implants [33], and 3D printed parts (Fig. 1.4) [34]. For planar substrates, the presence

of topographical features can greatly modify film evolution and adversely influence the quality of the final coating [3]. Recirculation regions, for example, may form in topography valleys if both the topography waviness (the ratio of wave amplitude to wavelength) and film thickness are sufficiently large [35, 36, 37, 38]. These recirculation regions may strongly influence mixing, mass transport, and heat transport, and consequently, the quality of the final (dried) coating [35, 39, 40, 41].

The influence of topographical features on coating flows on rotating cylinders was first studied by Sahu and Kumar [42]. Applying the lubrication approximation, they derived and solved the governing equations for flow on a rotating cylinder patterned with sinusoidal topography. Their results reveal that when gravitational forces are negligible, steady states are reached where liquid tends to accumulate over the pattern troughs at low rotation rates and over the pattern crests at high rotation rates. When gravitational forces are significant, steady states cannot be attained, in contrast to the case of an unpatterned cylinder. The present chapter extends the work of Ref. [42] to study the more general case where the lubrication approximation is removed.

To do this, we employ the Galerkin finite-element method (GFEM), and also compare our results to those obtained from a lubrication model. Both modeling approaches are described in §4.2. Coating flows on rotating cylinders patterned with sinusoidal topography are studied in §4.3 and §4.4, where gravitational effects are absent and present respectively. Conclusions are given in §4.5.

4.2 Mathematical model

We consider flow of a Newtonian liquid with constant viscosity μ, density ρ, and surface tension σ on a topographically patterned rotating cylinder. For a cylinder with mean radius R_{mean}, its surface $R(\theta)$ can be expressed as

$$R = R_{\text{mean}} + \mathcal{B}(\theta), \tag{4.1}$$

where $\mathcal{B}(\theta)$ describes the shape of the topography as a function of the angular coordinate. For a sinusoidal surface topography (Fig. 4.1), $\mathcal{B}(\theta) = \delta \sin(\omega\theta)$, where δ and ω are the topography amplitude and (integer) frequency, respectively. The cylinder is rotating about its horizontal axis at constant angular speed Ω in the anti-clockwise direction. We are interested in the evolution of the film thickness around the cylinder circumference,

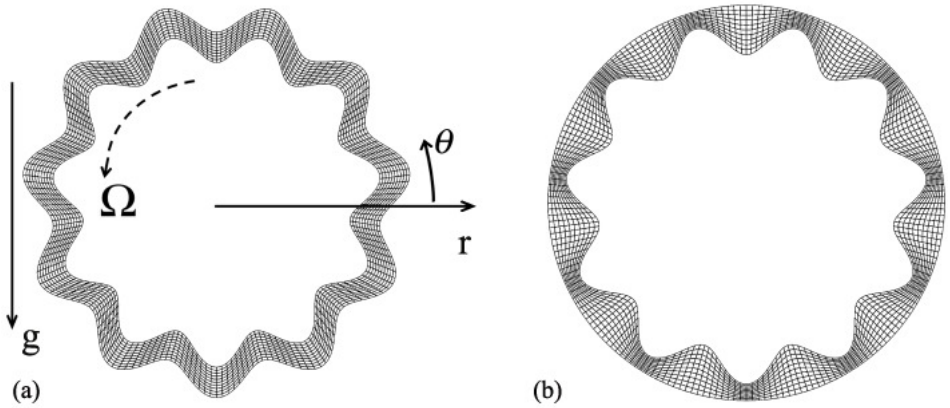

Figure 4.1: Problem geometry and sample finite-element meshes for two different initial conditions (ICs). (a) IC 1: uniform thickness, (b) IC 2: constant radius.

so any axial variations are neglected.

4.2.1 Governing equations

For studying liquid flow on a rotating cylinder, it is convenient to solve the governing equations in a rotating frame of reference. We employ polar coordinates with unit vectors $\mathbf{e}_r$, $\mathbf{e}_\theta$, and $\mathbf{e}_z$. The corresponding momentum balance equations can be written as [66]

$$\rho\left[\mathbf{u}_t + \mathbf{u}\cdot\boldsymbol{\nabla}\mathbf{u}\right] = -\boldsymbol{\nabla}p + \mu\nabla^2\mathbf{u} - \rho\boldsymbol{\Omega}\times(\boldsymbol{\Omega}\times\mathbf{r}) - 2\rho\boldsymbol{\Omega}\times\mathbf{u} + \rho\mathbf{g}, \tag{4.2}$$

where p is pressure, $\mathbf{u} = w\mathbf{e}_r + u\mathbf{e}_\theta$ is the velocity vector, t is time, $\mathbf{g} = g\mathbf{e}_g = -g\sin(\theta + \Omega t)\mathbf{e}_r + (-g\cos(\theta+\Omega t))\mathbf{e}_\theta$ is the gravitational field, $\boldsymbol{\Omega} = \Omega\mathbf{e}_z$ is the angular velocity, and $\mathbf{r}$ is the position vector of a fluid element.

Following Refs. [10] and [42], we scale length with R_{mean}, velocity with $U = \rho g R_{\text{mean}}^2/\mu$, time with R_{mean}/U, and pressure with $\mu U/R_{\text{mean}}$. The scaled governing equations are

$$\boldsymbol{\nabla}\cdot\mathbf{u} = 0, \tag{4.3}$$

$$Re[\mathbf{u}_t + \mathbf{u}\cdot\boldsymbol{\nabla}\mathbf{u}] = -\boldsymbol{\nabla}p + \nabla^2\mathbf{u} - W^2\mathbf{r} - 2Re_\Omega(\mathbf{e}_z\times\mathbf{u}) + \mathbf{e}_g, \tag{4.4}$$

where

$$W = \frac{\Omega}{\sqrt{g/R_{\text{mean}}}}, \quad Re = \frac{\rho^2 g R_{\text{mean}}^3}{\mu^2}, \quad Re_\Omega = \frac{\rho \Omega R_{\text{mean}}^2}{\mu}.$$

Here, W is the dimensionless rotation rate, Re is a Reynolds number based on a gravitational drainage velocity ($\rho g R_{\text{mean}}^2/\mu$), and Re_Ω is a Reynolds number based on the cylinder velocity ($R_{\text{mean}}\Omega$).

To simplify the governing equations, we neglect inertial effects arising from gravitational drainage ($Re[\mathbf{u}_t + \mathbf{u} \cdot \boldsymbol{\nabla}\mathbf{u}]$) and cylinder rotation ($2Re_\Omega(\mathbf{e}_z \times \mathbf{u})$). However, following Refs. [10] and [67], we still retain the centrifugal term ($W^2\mathbf{r}$). With these changes, Eq. (4.4) becomes

$$\mathbf{0} = -\boldsymbol{\nabla} p + \nabla^2 \mathbf{u} - W^2 \mathbf{r} + \mathbf{e}_g. \tag{4.5}$$

At the cylinder surface, $r = R(\theta) = R_{\text{mean}} + \delta \sin(\omega\theta)$, we apply no-slip and no-penetration conditions,

$$\mathbf{t} \cdot \mathbf{u} = 0, \quad \mathbf{n} \cdot \mathbf{u} = 0, \tag{4.6}$$

where $\mathbf{n}$ and $\mathbf{t}$ are the unit outward normal and tangent vectors.

At the free surface, the liquid needs to satisfy the kinematic and interfacial-stress boundary conditions,

$$\mathbf{n} \cdot \mathbf{u} = \mathbf{n} \cdot \dot{\mathbf{r}}, \tag{4.7}$$

$$\mathbf{n} \cdot \mathbf{T} = -\frac{\kappa}{Bo}\mathbf{n}, \tag{4.8}$$

where $\mathbf{T}$ is the total stress tensor, the components of which are nondimensionalized by $\mu U/R_{\text{mean}}$. The Bond number $Bo = \rho g R_{\text{mean}}^2/\sigma$ is a measure of the importance of surface-tension forces relative to gravitational forces, and $\kappa = \boldsymbol{\nabla} \cdot \mathbf{n}$ is the surface curvature. The dot above the $\mathbf{r}$ in Eq. (4.7) denotes a temporal derivative.

Order-of-magnitude estimates for key dimensional quantities are listed in Table 4.1. For the applications that motivate this work, the characteristic film thickness H is at least an order of magnitude smaller than the mean cylinder radius R_{mean}, so lubrication theory can be used to estimate the strength of inertial forces. Using lubrication scalings, the Reynolds number becomes $Re = \rho g H^2 R_{\text{mean}}/\mu^2$ while Re_Ω has the same definition as before, and both of these are multiplied by ϵ^2 in the governing equations, where $\epsilon = H/R_{\text{mean}}$ [10]. For the parameter values listed in Table 4.1, $\epsilon^2 Re$ and $\epsilon^2 Re_\Omega$ are

both no more than $O(10^{-1})$, justifying our neglect of these inertial terms. Inertial effects may become important for thicker films, less viscous liquids, and faster rotation rates, and lead to an even richer range of behavior than that reported here.

The equations associated with the above two-dimensional (2D) model are solved numerically with GFEM. The GFEM results are used to assess the validity of a lubrication-theory-based model (§4.2.3). The 2D model allows us to keep all nonlinearities of the system, and thus study with confidence flow regimes where the lubrication model is not formally valid. However, due to the high computational costs associated with the 2D model, for some of the calculations conducted in the thin-film regime in §4.3 and §4.4, only results from the lubrication model are presented.

Table 4.1: Order-of-magnitude estimates of dimensional quantities. The viscosity, density, and surface tension are representative of a glycerol-water mixture.

Constants	Typical values
Mean cylinder radius, R_{mean} (cm)	1
Rotation rate, Ω (rad/s)	$10^{-1} - 10^{1}$
Viscosity, μ (cP)	300
Density, ρ (g/cm^3)	1
Surface tension, σ (dyn/cm)	$10^{1} - 10^{2}$
Characteristic film thickness, H (cm)	$10^{-3} - 0.1$

Details about our Galerkin finite element scheme is given in Appendix C. We perform simulations with two different initial conditions (ICs) for the liquid film that coats the cylinder: IC 1-uniform thickness (Fig. 4.1a), and IC 2-constant radius (Fig. 4.1b). For our calculations, 2000 elements (200 elements in the axial direction and 10 elements in the radial direction) were found to be sufficient. Conservation of total mass is monitored and the results are considered accurate when $100(V_{max} - V_{min})/V_{ini} < 0.1\%$, where V_{max} and V_{min} are the maximum and minimum volumes of the liquid during the entire calculation, and V_{ini} is the initial volume [68].

4.2.2 Lubrication theory

Following Ref. [42], lubrication theory can be applied to derive a nonlinear evolution equation for the film thickness h,

$$\begin{aligned}\frac{\partial h}{\partial t} =& \frac{\partial}{\partial \theta}\left(\frac{h^3}{3}\cos\left(\theta + MWt\right) - \frac{h^3}{3Bo}\left(\frac{\partial h}{\partial \theta} + \frac{\partial^3 h}{\partial \theta^3}\right) - \frac{h^3}{3}\left(W^2 - \sin\left(\theta + MWt\right)\right)\frac{\partial h}{\partial \theta}\right) - \\ & \frac{\partial}{\partial \theta}\left(\frac{h^3}{3Bo}\left(\delta\omega\cos(\omega\theta) - \delta\omega^3\cos(\omega\theta)\right) + \frac{h^3}{3}\left(W^2 - \sin\left(\theta + MWt\right)\right)\delta\omega\cos(\omega\theta)\right),\end{aligned} \tag{4.9}$$

where $M = \mu/\rho\sqrt{gR_{\text{mean}}}$ is the dimensionless viscosity. In deriving this equation, we have assumed that $\epsilon = H/R_{\text{mean}} \ll 1$, and we have rescaled all lengths by R_{mean} to be consistent with the equations of §4.2.1.

This evolution equation allows for the study of nonlinear phenomena at a relatively modest cost compared to solving the full governing equations with GFEM. We note that Eq. (4.9) is a corrected version of Eq. (43) in Sahu and Kumar [42]; an extra factor of two in front of $\delta\omega\cos(\omega\theta)$ in the last term appeared in the latter equation. For a cylinder patterned with sinusoidal topography, the lubrication approximation is expected to work well when the pattern wavelength is much greater than the characteristic film thickness H ($\omega H \ll R_{\text{mean}}$) and the topography amplitude is much less than the cylinder radius $\delta \ll 1$ [42].

For a fixed set of problem parameters (δ, ω, Bo, M and W), we solve Eq. (4.9) numerically by applying a partially implicit finite-difference scheme [10, 53]. Film thickness is obtained over 400 uniformly discretized nodes at a given instant of time in a reference frame rotating with the cylinder. Solution accuracy is checked in a manner similar to that described in §4.2.2.

4.3 Results: Zero-gravity case

We first study the case of a cylinder with sinusoidal topography that is spinning so rapidly so that gravitational effects are negligible. It is no longer appropriate to take the drainage rate as the characteristic velocity in this regime, so we rescale the governing equations by using σ/μ and σ/R_{mean} as the new characteristic velocity and pressure (stress) respectively. When all gravitational terms are neglected, Eqs. (4.5) and (4.9)

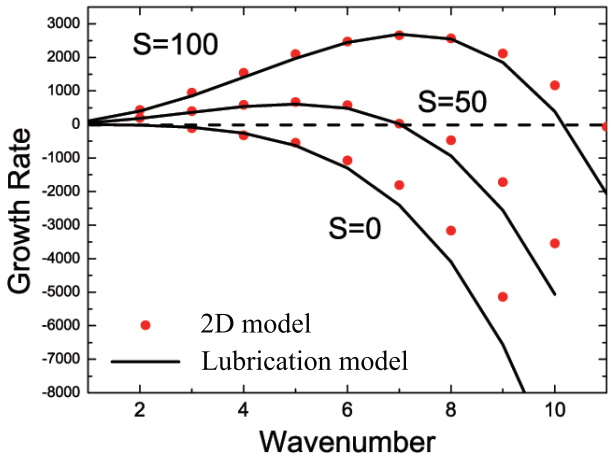

Figure 4.2: Growth rates versus wavenumber in the absence of gravity on an unpatterned cylinder with $h_0 = 0.1$.

become

$$0 = -\boldsymbol{\nabla} p + \nabla^2 \mathbf{u} - S\mathbf{r}, \tag{4.10}$$

$$\frac{\partial h}{\partial t} = -\frac{1}{3}\frac{\partial}{\partial \theta}\left[h^3\left(\frac{\partial h}{\partial \theta} + \frac{\partial^3 h}{\partial \theta^3} + S\frac{\partial h}{\partial \theta} + \delta\omega\cos(\omega\theta) - \delta\omega^3\cos(\omega\theta) + S\delta\omega\cos(\omega\theta)\right)\right], \tag{4.11}$$

where $S = \rho\Omega^2 R_{\text{mean}}^3/\sigma$ can be interpreted as an inverse Weber number or dimensionless rotation rate.

For an unpatterned cylinder ($\delta = 0$), evolution equation (4.11) reduces to that studied in Ref. [10]. Linear stability analysis reveals that perturbations with wavenumber $k < k_{\text{cutoff}}$ grow in amplitude under the action of centrifugal forces, while those with $k > k_{\text{cutoff}}$ are leveled by surface tension. The cutoff wavenumber, k_{cutoff}, is

$$k_{\text{cutoff}} = [\sqrt{1+S}] \tag{4.12}$$

where $[x]$ is the greatest integer less than x. This instability growth rate $\hat{\omega}$ is

$$\hat{\omega} = \frac{1}{3}\{(1+S)k^2 - k^4\}h_0^3, \tag{4.13}$$

where h_0 is the dimensionless mean film thickness.

The fastest-growing wave number, $k_{\max}$, has the form

$$k_{\max} = [\sqrt{(1+S)/2}]. \tag{4.14}$$

Numerical solutions of Eq. (4.11) show that unstable disturbances grow to form a steady state in which droplets on the cylinder surface are separated by thin films [10]. Thus, $k_{\max}$ indicates the number of drops expected on an unpatterned cylinder at steady state. We note that here and elsewhere in this chapter, the steady states we report reflect the long-time behavior of the coating. Thus, they should be regarded as apparent steady states since we do not solve for the steady states directly.

To validate our numerical solutions, we extracted growth rates of perturbations having different wavenumbers on an unpatterned cylinder using a representative mean film thickness of $h_0 = h(\theta, t = 0) = 0.1$. Results from the 2D model and lubrication model are in good agreement at low k (Fig. 4.2) over a broad range of rotation rates (S). But with increasing k, which corresponds to higher curvature at the free surface, the agreement worsens and the lubrication model overestimates the leveling rate (smaller growth rate). Since faster leveling is related to stronger capillary flows, the lubrication model tends to overestimate the effects of surface tension in regions where the free-surface curvature is large. Although not shown here for brevity, the growth rates extracted from numerical solution of Eq. (4.11) agree well with the linear stability result (Eq. (4.13)) for all k.

For a topographically patterned cylinder ($\delta \neq 0$), it was observed in Ref. [42] that liquid tends to accumulate over the pattern troughs at low rotation rates, and over the pattern crests at high rotation rates. Although this transition occurs over a range of rotation rates, it would be useful to have a single value that characterizes the transition. We refer to this value as the critical rotation rate S_{critical}, and have found that it can be estimated from Eq. (4.12). Suppose that the cylinder pattern creates a perturbation at the free surface with $k = \omega$, as would happen if one had an initial condition of uniform film thickness (Fig. 4.1). Then, inversion of Eq. (4.12) yields

$$S_{\text{critical}} = \omega^2 - 1. \tag{4.15}$$

For $S < S_{\text{critical}}$, a film having an initially uniform thickness would be expected to level at short times, driving liquid into the pattern troughs. Because there is more

liquid in the troughs, centrifugal forces would be stronger there and the liquid would be expected to thicken there at longer times. For $S > S_{\text{critical}}$, centrifugal forces would overwhelm the short-time leveling, and drops would be expected to form over the crests, where the centrifugal forces are stronger due to their greater distance from the cylinder center. Note that S_{critical} increases as the pattern frequency does, reflecting the fact that shorter wavelength disturbances are leveled (by surface tension) more easily.

In the following sections, we explore the nonlinear behavior of the film in the zero-gravity regime using numerical solutions of the lubrication model (Eq. (4.11)) and the 2D model (Eq. (4.10)). Following Ref. [42], we initially fix the pattern amplitude at $\delta = 0.01$ and the mean film thickness at $h_0 = 0.02$, and examine the cases where $S < S_{\text{critical}}$ (§4.3.1) and $S > S_{\text{critical}}$ (§4.3.2). We then consider the case of larger pattern amplitude (§4.3.3).

4.3.1 $S < S_{\text{critical}}$

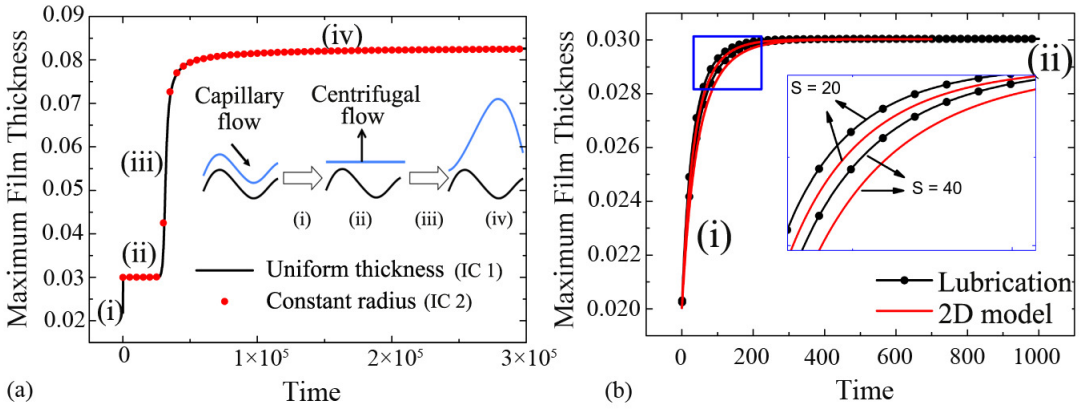

Figure 4.3: Time variation of maximum film thickness on a patterned cylinder with $\delta = 0.01$, $\omega = 11$, $h_0 = 0.02$, and $S_{\text{critical}} = 120$. (a) Results obtained with the lubrication model for $S = 40$ and two different initial conditions. (b) Results obtained with the lubrication model and the 2D model in stages (i) and (ii) for different values of S with an initial film of uniform thickness.

We first consider a cylinder with pattern frequency $\omega = 11$, where the corresponding critical rotation rate is $S_{\text{critical}} = 120$. To characterize film evolution, in Fig. 4.3 we plot the maximum film thickness as a function of time in the regime where $S < S_{\text{critical}}$.

Two different initial conditions are considered: (i) a film of uniform thickness and (ii) a film of constant radius (Fig. 4.1).

Fig. 4.3a shows that the steady maximum film thickness predicted by the lubrication model is independent of the initial condition. In addition, if the initial film is of uniform thickness, the formation of drops follows four distinct stages, which we summarize here using $S = 40$ as a representative case. In stage (i), capillary forces are stronger than centrifugal forces, driving liquid from the pattern crests to the pattern troughs, which leads to a coating of constant radius in stage (ii). Since the coating is thicker over the troughs and thinner over the crests, the centrifugal forces on the liquid over the troughs are stronger, and thus produce liquid drops over the troughs in stage (iii). These drops rapidly grow in size until the coating reaches a steady state in stage (iv), where centrifugal forces are balanced by surface-tension forces. If the initial film is of uniform radius, then the film starts in stage (ii) and goes through stages (iii) and (iv).

In Fig. 4.3b, we focus on stages (i) and (ii), plotting the evolution of the maximum film thickness for $S = 20$ and 40. The maximum film thickness in stage (ii) is independent of S; however, an increase in S hinders the rate of leveling (smaller maximum film thickness) in stage (i). This is simply because a higher value of S leads to stronger centrifugal forces on the liquid over the crests, which slows down the capillary leveling. The comparison in Fig. 4.3b between results obtained from the lubrication model and the 2D model suggests that the lubrication model tends to overpredict the leveling rate, which is consistent with our earlier observation that effects of surface tension are overestimated by the lubrication model.

To investigate the influence of rotation rate on liquid motion, in Fig. 4.4 we plot the steady film thickness profiles and free-surface profiles (stage (iv)) calculated with the lubrication model. These steady states occur at late times ($t \sim 10^5$) (Fig. 4.3a). Simulations with such extensive durations are computationally prohibitive with our GFEM scheme due to the small time-step size needed in the zero-gravity regime. Thus, only results from the lubrication model are shown in Fig. 4.4.

For a relatively small rotation rate, $S = 10$ (Figs. 4.4a and 4.4b), liquid accumulating in adjacent troughs partially merges to form larger drops that span several troughs. As the value of S (and thus the centrifugal force) is increased (Figs. 4.4c and 4.4d), several drops of nearly uniform size and spacing form, and these are located over troughs.

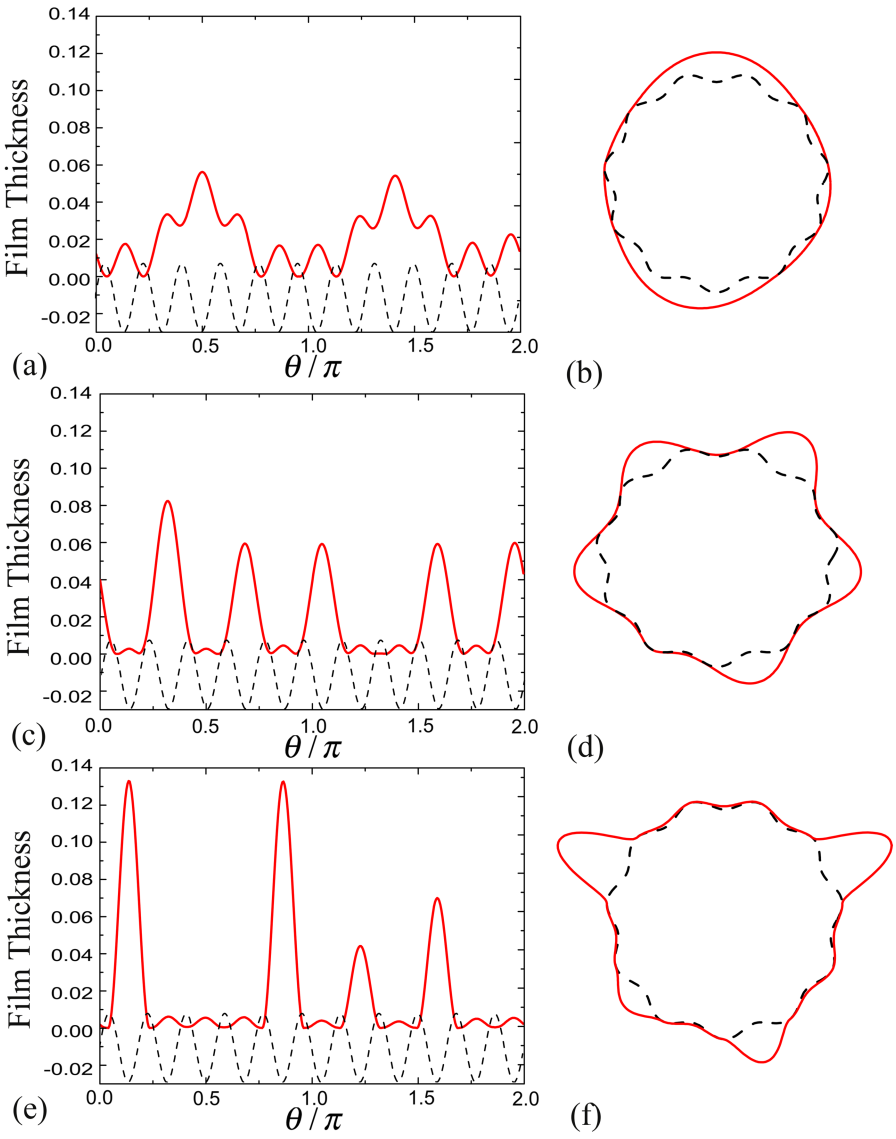

Figure 4.4: Steady film thickness profiles and corresponding free-surface profiles obtained from the lubrication model with $\delta = 0.01$, $\omega = 11$, and $h_0 = 0.02$ for (a, b) $S = 10$, (c, d) $S = 40$, and (e, f) $S = 100$. Initial conditions are films of uniform thickness. Dashed lines indicate surface topography. For ease of visualization, in panels (b), (d) and (f), the film thickness and pattern amplitude plotted are five times larger than the actual values.

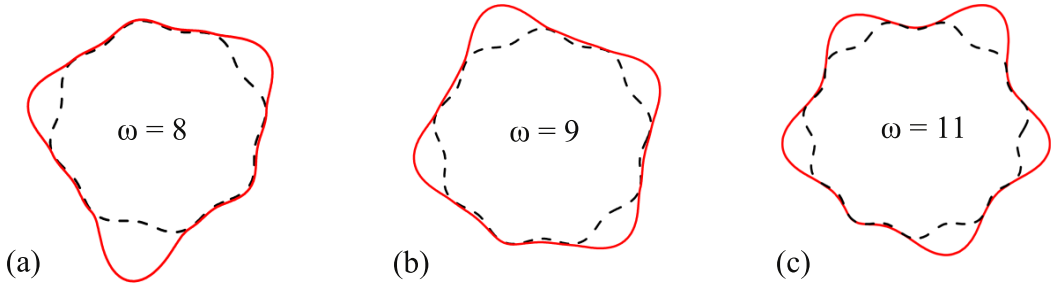

Figure 4.5: Steady free-surface profiles obtained from the lubrication model with $\delta = 0.01$, $S = 40$, and $h_0 = 0.02$ for (a) $\omega = 8$, (b) $\omega = 9$, and (c) $\omega = 11$. Initial conditions are films of uniform thickness. Dashed lines indicate surface topography. For ease of visualization, the film thickness and pattern amplitude plotted are five times larger than the actual values.

However, further increasing the rotation rate breaks the uniformity of drop size and causes an uneven distribution of liquid on the cylinder surface, as can be seen in Fig. 4.4e and 4.4f. The behavior shown in Fig. 4.4 clearly indicates that the steady film profile on a patterned cylinder is highly sensitive to the rotation rate in the regime where $S < S_{\text{critical}}$.

Note that for unpatterned cylinders with $S = 10, 40$, and 100, the fastest growing wavenumber $k_{\max}$ (calculated from Eq. (4.14)) is two, four, and seven, respectively. This indicates that two drops will develop on the cylinder when $S = 10$, six drops will develop when $S = 40$, and ten drops will develop when $S = 100$ at steady state when surface topography is absent [10, 42]. However, Fig. 4.4d and 4.4f show that with the presence of surface topography, the number of drops is five for $S = 40$ and four for $S = 100$. These do not match the corresponding values of $k_{\max}$, indicating that even small-amplitude surface topography significantly modifies the liquid distribution around the cylinder when $S < S_{\text{critical}}$. As the mismatch worsens as S increases, the influence of surface topography becomes more pronounced as the rotation rate (centrifugal force) increases. Moreover, for a fixed value of S, a decrease in ω leads to fewer troughs on the cylinder and therefore fewer drops, as shown in Fig. 4.5.

Finally, we briefly comment about the possible influence of several other parameters for which we have not been able to perform exhaustive studies. As film thickness increases for fixed topography amplitude, we expect that the influence of topography will

be diminished due to increasing disparity in the two length scales. Based on the results of Ref. [42], we expect that as the rotation rate increases, the topography amplitude required to trigger the effects we have observed will decrease due to the stronger centrifugal forces. As the pattern frequency decreases, the topography amplitude required to trigger the effects we have observed is expected to decrease as well due to lower free-surface curvatures (and thus slower film leveling).

4.3.2 $S > S_{\text{critical}}$

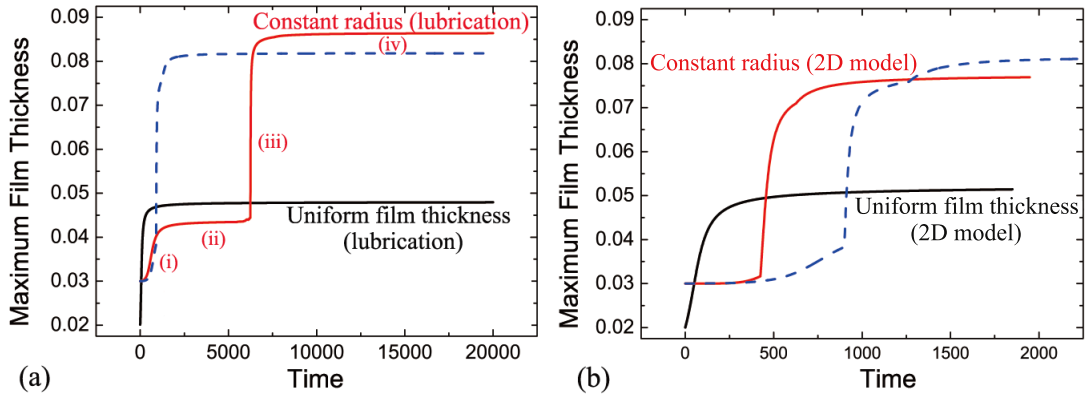

Figure 4.6: Time variation of the maximum film thickness with $S = 160$ ($> S_{\text{critical}}$), $\delta = 0.01$, $\omega = 11$, and $h_0 = 0.02$. Results are obtained with the (a) lubrication model and (b) 2D model. Results obtained by using the lubrication model with an initial film of constant radius and a superimposed perturbation are plotted in both panels for comparison (blue dashed line).

We now turn to the regime where $S > S_{\text{critical}}$, and consider the case $S = 160$ as a representative example. In Fig. 4.6a we plot the time-variation of the maximum film thickness obtained with the lubrication model starting from initial films of constant radius and uniform thickness. The results suggest that the steady film thickness profile strongly depends on the initial film condition, in contrast to the case where $S < S_{\text{critical}}$. For an initial coating of uniform thickness (black solid line), higher centrifugal forces on the liquid over the crests lead to the flow of liquid from surrounding areas and the formation of drops over the crests. The coating reaches a steady state almost immediately with drops of almost the same size connected by very thin films over the

troughs. Here, the number of drops is equal to the pattern frequency. The corresponding steady film-thickness profile and free-surface profile are plotted in Fig. 4.7a and 4.7b.

A similar time-history of film evolution is also observed with the 2D model, shown in Fig. 4.6b with a black solid line. Note that the time period shown in Fig. 4.6b is much shorter than that in Fig. 4a, reflecting faster growth of free-surface perturbations at higher S. As can be seen in Fig. 4.7a, the film-thickness profile predicted by the 2D model agrees well with the prediction from the lubrication model. The maximum film thickness predicted by the lubrication model is slightly smaller, which can be understood by recalling that this model tends to overestimate the effects of surface tension.

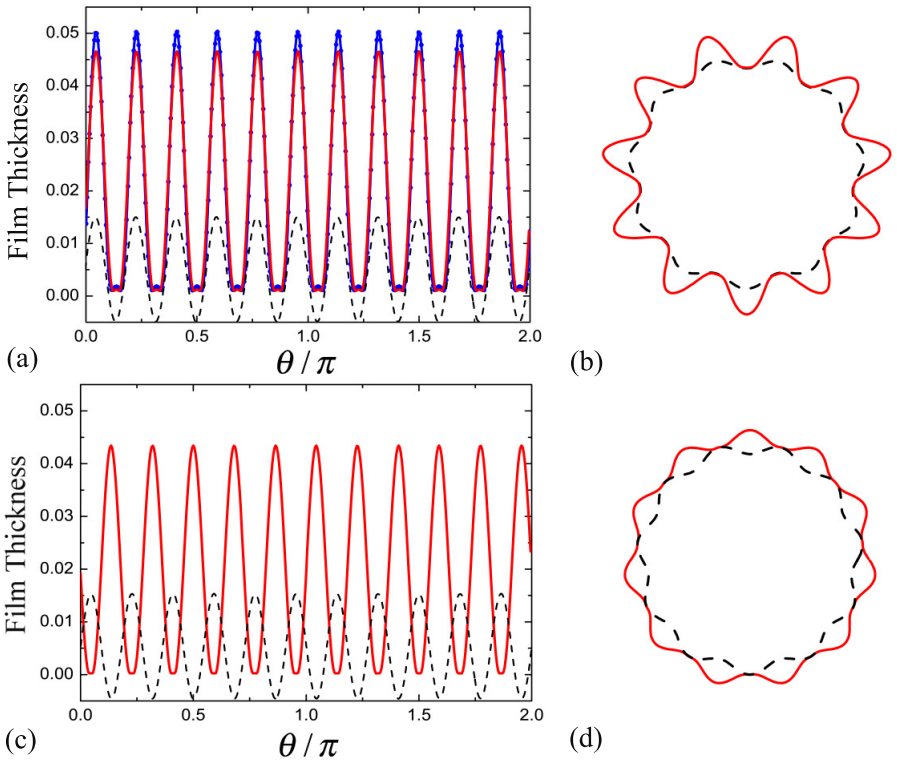

Figure 4.7: Film-thickness profiles (a, c) and free-surface profiles (b, d) obtained with the lubrication model (red solid line) and the 2D model (blue dotted line) at $t = 2000$ with $S = 160$, $\delta = 0.01$, $\omega = 11$, and $h_0 = 0.02$. Initial conditions are films of (a, b) uniform thickness and (c, d) constant radius (Results from the 2D model are only shown in (a)). Dashed lines indicate surface topography. For ease of visualization, in panels (b) and (d) the film thickness and pattern amplitude plotted are five times larger than the actual values.

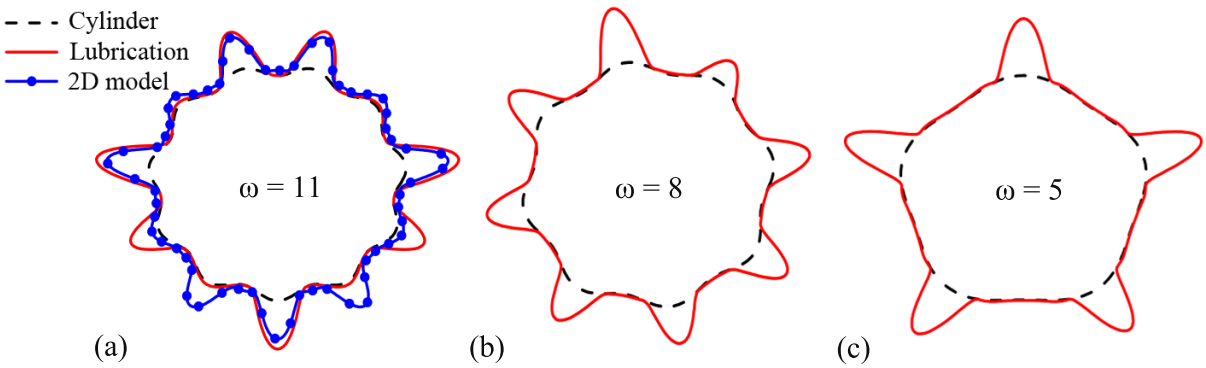

Figure 4.8: Steady free-surface profiles with $S = 160$, $\delta = 0.01$, and $h_0 = 0.02$ for (a) $\omega = 11$, (b) $\omega = 8$, and (c) $\omega = 5$. Initial conditions are films of constant radius and no noise added. For ease of visualization, the film thickness and pattern amplitude plotted are five times larger than the actual values.

For an initial coating of constant radius (red solid line in Fig. 4.6a), the lubrication model predicts that film evolution follows four stages when $S > S_{\text{critical}}$. In stages (i) and (ii), centrifugal forces are stronger on the liquid over the troughs (relative to the liquid on the crests), producing drops over the troughs (similar to what is observed when $S < S_{\text{critical}}$). The film-thickness profile and free-surface profile are shown in Fig. 4.7c and 4.7d. However, these drops are not stable when located over the troughs and tend to shift to the crests in stage (iii). During this shifting process liquid is redistributed, leading to uneven drop sizes.

The coating reaches a steady state in stage (iv), and we plot in Fig. 4.8a the corresponding free-surface profile. The liquid is unevenly distributed on the cylinder, with seven main drops and four smaller drops over the crests, in contrast to the case where the initial condition is a film of uniform thickness (Fig. 4.7b). Note that the total number of drops is equal to the pattern frequency ($\omega = 11$).

The time variation of the maximum film thickness predicted by the 2D model for an initial coating of constant radius is shown in Fig. 4.6b (red solid line). There are marked differences from the result predicted by the lubrication model (red solid line in Fig. 4.6a). Both the 2D model and lubrication model predict that drops form over the troughs initially. But the 2D model predicts that liquid redistribution and a steady state occur much earlier. As can be seen in Fig. 4.8a, the number of main drops and their sizes, but not their location, are in good agreement with those predicted by the

lubrication model.

Although not shown here, both models predict that as the value of S increases, the size of the main drops tends to increase (due to the stronger centrifugal forces). Although the locations of the drops change, the total number of drops (which is equal to the pattern frequency) does not. (The drops also grow more quickly as S increases.) Thus, when $S > S_{\text{critical}}$, the film profile on a patterned cylinder does not appear to be as sensitive to the rotation rate as it does when $S < S_{\text{critical}}$.

To explain the discrepancy between the lubrication and 2D predictions for the constant-radius initial condition, we perform simulations using the lubrication model with an initial coating of constant radius plus a small-amplitude random noise,

$$h(\theta, t = 0) = (h_0 - \delta \sin(\omega\theta))(1 + \alpha[R_\theta - 0.5]),$$

where $\alpha = 10^{-6}$ and R_θ denotes a random number chosen uniformly between 0 and 1. Results are shown in both Fig. 4.6a and 4.6b with blue dashed lines. As can be seen, the steady state is reached more quickly relative to the case where the perturbation is absent (although not as quickly as in the 2D model). Based on this observation, we conjecture that our GFEM scheme has greater discretization error and this acts like random noise.

In practice, dip coating and spray coating are commonly used to coat the initial film [69, 7, 8]. Since an initial film of uniform thickness may be difficult to obtain with these methods, for the rest of this section we only consider the constant-radius initial condition. To show how substrate curvature modifies the liquid distribution, in Figs. 4.8b and 4.8c, we plot the steady free-surface profiles obtained from the lubrication model for $\omega = 8$ and $\omega = 5$. With a decrease in pattern frequency, drop size becomes more uniform (Note that the number of drops is again equal to ω.) The increased uniformity occurs because lower pattern frequency corresponds to larger drop spacing in stage (ii), leading to less interaction (and thus less liquid redistribution) between drops.

Overall, the results from §4.3.1 and §4.3.2 indicate that when the topography amplitude and film thickness are much smaller than the cylinder radius ($\sim$1%), the lubrication model yields predictions that are in quantitative agreement with many of the predictions

of the 2D model. Differences arise in predictions of transient behavior and drop location, especially when $S > S_{\text{critical}}$. In addition, the steady free-surface profiles appear to be very sensitive to the initial film condition when $S > S_{\text{critical}}$.

Finally, we briefly summarize the results of some additional calculations we have performed where the topography is non-uniform. If the topography has frequency ω_1 over some portion of the cylinder and ω_2 over the other, then a critical rotation rate can be associated with each of these frequencies. If the rotation rate is below both critical values, drops form over the troughs at steady state. If it is larger than both critical values, drops form over the crests. If the rotation rate is between the critical values, then drops form over troughs on the portion of the surface where the rotation rate is above the corresponding critical value, and drops form over the crests on the portion where the rotation rate is below the the corresponding critical value. Thus, where the drops are positioned at steady state strongly depends on the local curvature of the surface topography.

4.3.3 Larger pattern amplitude

To examine the case of larger topography amplitude, we set $\delta = 0.1$, which is now an order-of-magnitude larger, and perform simulations with both the 2D and lubrication models. Simulations were performed with $h_0 = 0.02$ first, but the film thickness approached zero almost immediately over the crests in both models and could no longer be resolved numerically. To avoid this, we set $h_0 = 0.13$ instead, which is also an order-of-magnitude larger and comparable to the topography amplitude.

Free-surface profiles for two different values of S are shown in Fig. 4.9. For $S = 90$, which is less than $S_{\text{critical}} = 120$, the lubrication model predicts that a steady state is attained. As shown in Fig. 4.9a, several drops form and are located over pattern troughs, consistent with what was observed in §4.3.1. In contrast, we are unable to find a steady state with the 2D model. Due to the larger film thickness, the drops form more rapidly and highly distorted interface shapes result that are computationally expensive to resolve. For the case shown in Fig. 4.9b, two drops located over pattern crests grow rapidly, and the simulation must be ended before they break off. We have observed similar behavior for even smaller values of S (We note that if S becomes too small, the free-surface perturbations grow very slowly and the computation times

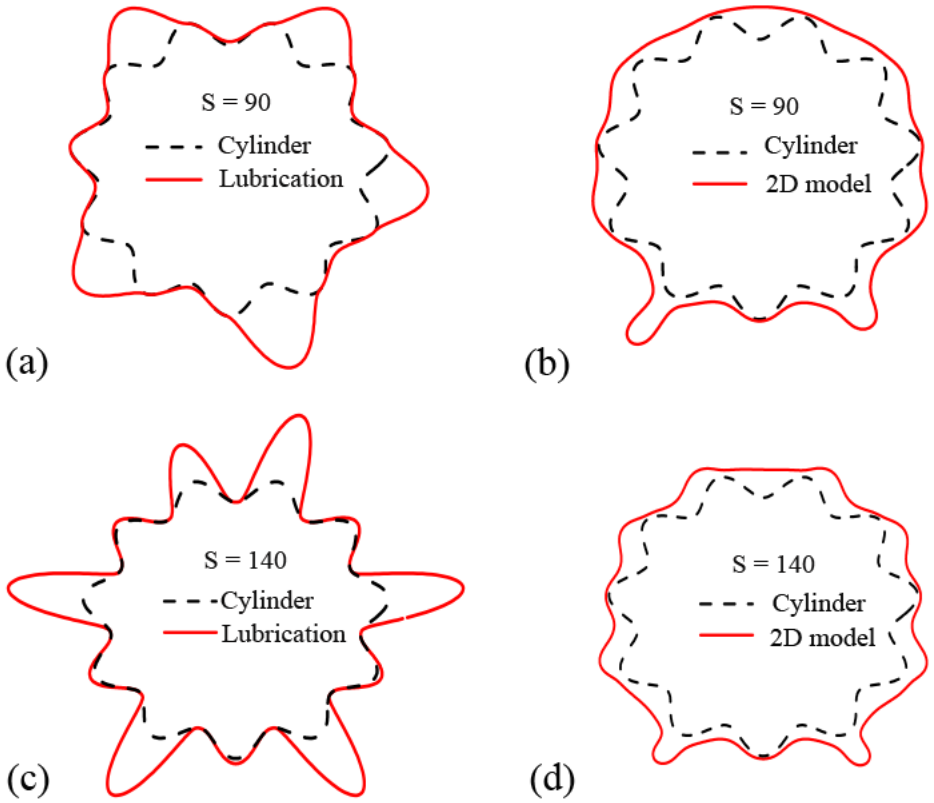

Figure 4.9: (a,c) Steady free-surface profiles obtained with the lubrication model. (b,d) Free-surface profiles just before drop break-off obtained with the 2D model. In (a,b), $S = 90$, and in (c,d), $S = 140$. In both cases, $\delta = 0.1$, $\omega = 11$ and $h_0 = 0.13$. Initial conditions are films of constant radius. Dashed lines indicate surface topography.

become prohibitive.)

For $S = 140$, which is greater than $S_{\text{critical}} = 120$, the lubrication model again predicts that a steady state is attained. As shown in Fig. 4.9c, this time drops form over the pattern crests, consistent with what was observed in §4.3.2. Again we are unable to find a steady state with the 2D model. For the case shown in Fig. 4.9d, drops appear to form over the pattern crests, but two of them grow rapidly and the the simulation is once more ended before they break off.

The results of these calculations indicate that for larger pattern amplitudes (∼10% of the cylinder radius), predictions from the lubrication model are not in good agreement

with those from the 2D model. As pattern amplitude increases, so does the free-surface curvature as the film thins over the topography, making the influence of surface tension more pronounced. Since the lubrication model tends to overestimate the effects of surface tension (as noted earlier), it is perhaps not surprising that it more readily predicts steady states when the pattern amplitude is large. Although not shown here, the lubrication model also predicts that free-surface perturbations grow more slowly, consistent with the overestimation of surface tension in that model.

4.4 Results: Gravity effects

In this section we include the effects of gravity. We first consider small-amplitude topography, then turn to the case of larger-amplitude topography.

4.4.1 Small-amplitude topography

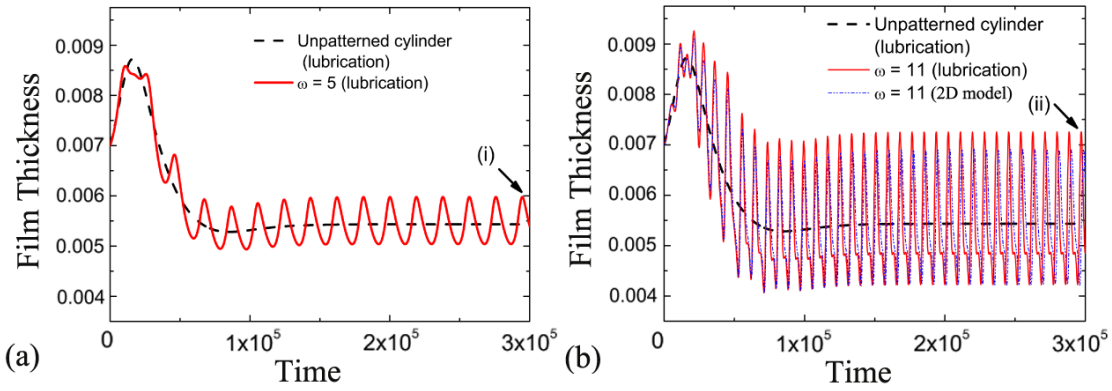

Figure 4.10: Time variation of film thickness at $\theta = 3\pi/2$ with $M = 0.1$, $Bo = 100$, $\delta = 0.01$, $h_0 = 0.007$, $W = 0.0007 < W_c$, and (a) $\omega = 5$ and (b) $\omega = 11$. The corresponding film profiles at time (i) and (ii) are shown in Fig. 4.11.

To study small-amplitude topography, we set $\delta = 0.01$. Following Ref. [42], all simulations shown here are performed with an initial film of uniform thickness $h_0 = 0.007$. Results of other simulations we have performed indicate that the film profiles at later times are independent of the initial film condition when gravity is significant.

The corresponding critical rotation rate, beyond which a smooth coating can be obtained on an unpatterned cylinder, can be calculated from Moffatt's load condition,

$W_c = 2.01h_0^2/M$ [10]. For the physical properties listed in Table 4.1, the dimensionless viscosity is $M = 0.1$, and thus $W_c = 0.001$. Results obtained with the 2D model agree well with those from the lubrication model in the parameter regime of this section, so we only show the former in selected cases.

In Fig. 4.10, we plot the time variation of the film thickness at $\theta = 3\pi/2$ (cylinder bottom) with $W = 0.0007$ ($< W_c$) for $\omega = 0$ (unpatterned cylinder), $\omega = 5$, and $\omega = 11$ at $Bo = 100$. For an unpatterned cylinder with a rotation rate below the critical value, the film thickness reaches a steady state after several revolutions in which a liquid drop forms on the upward-moving side of the cylinder ($3\pi/2 < \theta < 2\pi$) due to gravity-driven drainage [10]. However, when surface topography is present, Fig. 4.10a shows that it triggers a sustained oscillation in film thickness. The coating thus never reaches a true steady state, but rather a quasi-steady state. With an increase in pattern frequency, the oscillation becomes more pronounced with higher frequency and amplitude, shown in Fig. 4.10b. As can be seen, the results from the 2D model agree well with those from the lubrication model.

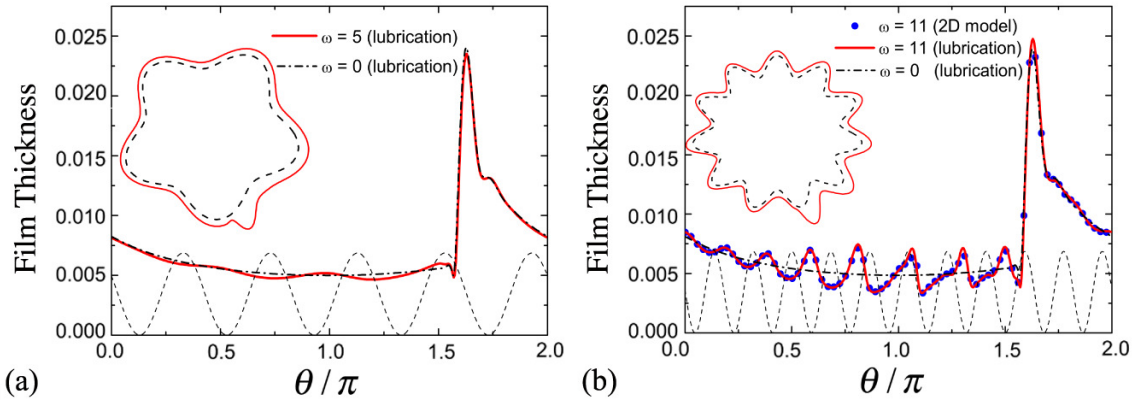

Figure 4.11: Film thickness profiles with $W = 0.0007$ ($< W_c$), $M = 0.1$, $Bo = 100$, $\delta = 0.01$, $h_0 = 0.007$ and (a) $\omega = 5$ at time (i) marked in Fig. 4.10a and (b) $\omega = 11$ at time (ii) marked in Fig. 4.10b. Dashed lines indicate surface topography. Insets: Corresponding free-surface profiles. For ease of visualization, the film thickness and pattern amplitude plotted in the insets are ten times larger than the actual values.

To explain why the oscillation becomes more pronounced with increasing ω, we select two time points during the quasi-steady stage labeled (i) and (ii) in Fig. 4.10a and 4.10b respectively, and plot the corresponding film thickness profiles in Figure

4.11. The steady thickness profile on an unpatterned cylinder is plotted in the same figure for comparison. For relatively low pattern frequency (Fig. 4.11a), the surface topography barely alters the coating thickness, and the film is almost uniform within $0 < \theta < 3\pi/2$. This can be attributed to the fact that surface tension only makes a significant contribution to the flow behavior in the region where free-surface curvature is high [10] (i.e., the vicinity of the drop that hangs near the cylinder bottom). As a result, the effects of surface topography dominate the effects of surface tension within $0 < \theta < 3\pi/2$, creating a free-surface shape that has the impression of the topography.

However, an increase in pattern frequency greatly strengthens the effects of surface tension within $0 < \theta < 3\pi/2$, driving liquid from the pattern crests to the pattern troughs. As a consequence, liquid tends to pool more over the troughs, with very thin films forming over the crests (Fig. 4.11b). This corresponds to a larger variation in film thickness compared to the low-frequency case (Fig. 4.11a), and is consistent with the more pronounced oscillation illustrated in Fig. 4.10b. We have also performed simulations with different values of δ and Bo, and the results show that either increasing δ or decreasing Bo leads to larger oscillation amplitudes due to stronger surface-tension effects.

For an unpatterned cylinder with rotation rate $W > W_c$, a smooth (Moffatt-type) coating is obtained at steady state, with a thicker film on the upward-moving side and a thinner film on the downward-moving side [9]. Such a coating is desirable for many applications, where the goal is to maintain a nearly uniform film thickness. To facilitate comparison with cases where surface topography is present, we plot the steady film thickness profiles on an unpatterned cylinder for two different values of Bo in Fig. 4.12a. This shows that the steady thickness profile is nearly independent of Bo because surface tension only plays a minor role in the free-surface evolution when $W > W_c$ and surface topography is absent [70, 56]. The corresponding free-surface profiles are shown in Fig. 4.13a.

For a patterned cylinder with $W > W_c$, the film thickness never reach a true steady state, but it does reach a quasi-steady state in which surface topography triggers an oscillation in thickness superimposed on the Moffatt-type coating. We plot in Fig. 4.12b and 4.12c the thickness profiles in the quasi-steady state when $Bo = 100$ and $Bo = 10$, respectively. When $Bo = 100$, the oscillation in film thickness is much more pronounced

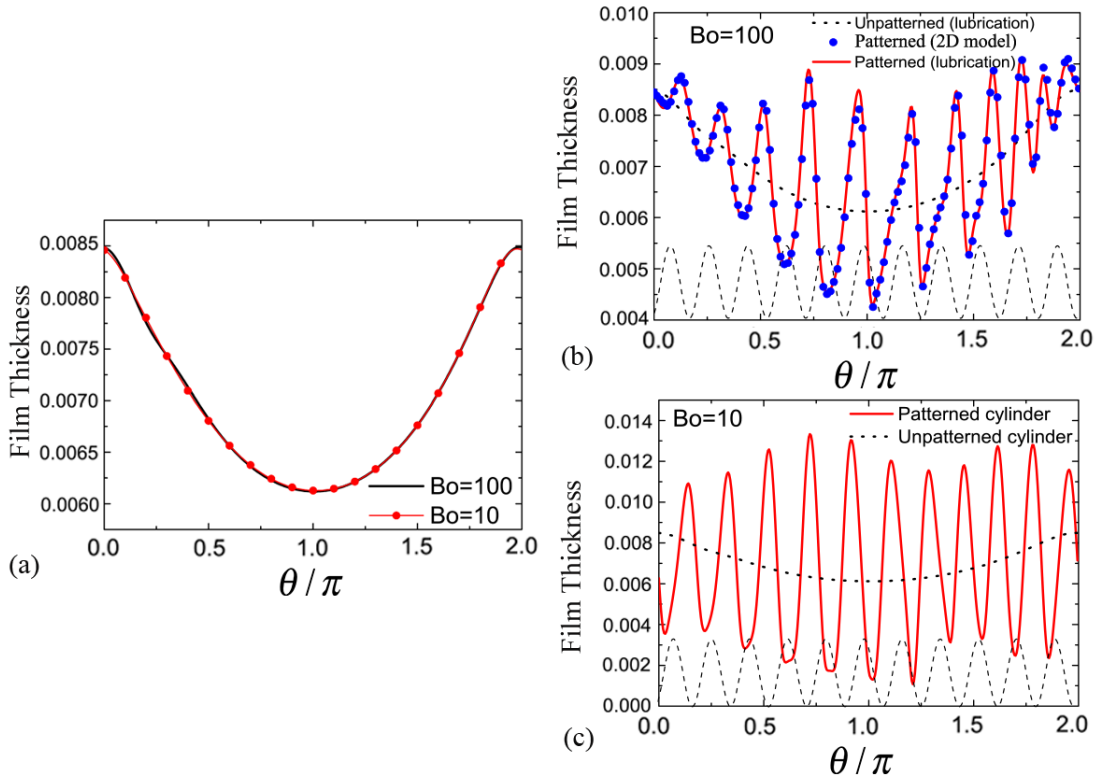

Figure 4.12: Film thickness profiles obtained from the lubrication model at $t = 10^6$ with $W = 0.0012 > W_c$, $M = 0.1$, and $h(\theta, t = 0) = 0.007$. (a) Unpatterned cylinder. (b,c) Patterned cylinder with $\delta = 0.01$ and $\omega = 11$. Results from the 2D model are also shown in (b). Dashed lines at the bottom of panels (b) and (c) indicate surface topography.

on the downward-moving side ($\pi/2 < \theta < 3\pi/2$) than on the upward-moving side. Since the coating is thinner on the downward-moving side, weaker gravitational forces on the liquid on this side are overwhelmed by surface-tension forces, causing more liquid to flow to the troughs on the downward-moving side. This explains the nonuniform oscillation amplitude in film thickness in Fig. 4.12b. Again we see that the predictions of the 2D model agree well with those from the lubrication model.

The corresponding free-surface profile for $Bo = 100$ is shown in Fig. 4.13b. Here, we see that although there are variations in the film thickness, the coating closely conforms to the cylinder surface, a situation that may be desired for many applications. With

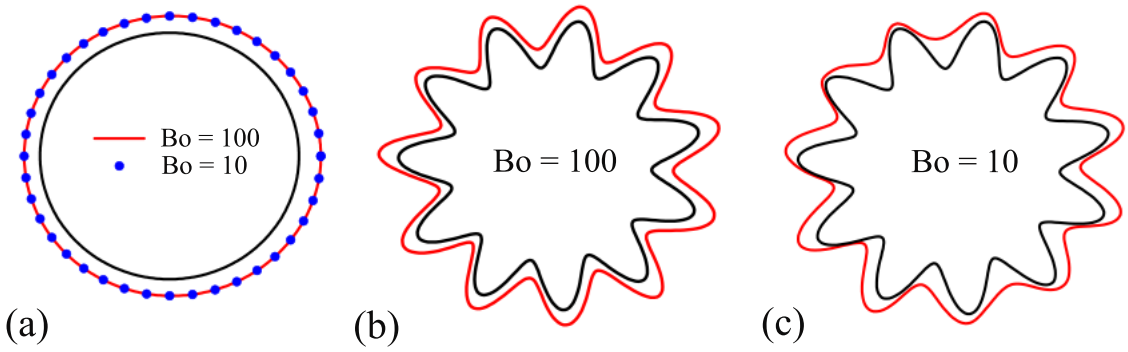

Figure 4.13: Free-surface profiles obtained from the lubrication model corresponding to the cases shown in Fig. 4.12. (a) Unpatterned cylinder (b,c) Patterned cylinders. For ease of visualization, the film thickness and pattern amplitude plotted are twenty times larger than the actual values.

a decrease in Bo to a value of 10, the variation in film thickness becomes much more uniform (Fig. 4.12c), indicating that surface-tension forces start to dominate on the upward-moving side as well. The corresponding free-surface profile in Fig. 4.13c shows that the coating does not conform as well to the cylinder surface. Here, surface-tension forces are stronger than for $Bo = 100$, and the resulting capillary flows tend to flatten the coating.

4.4.2 Larger-amplitude topography

To consider the case where the topography amplitude is larger, we increase δ by an order of magnitude to $\delta = 0.1$. With this amplitude, recirculation regions are observed to form inside the pattern troughs, an important qualitative difference from the small-amplitude case. As noted in §4.1, the presence of recirculation regions can strongly influence mixing, mass transport, and heat transport. We primarily present results from the 2D model; the validity of the lubrication approximation is discussed toward the end of this section.

As in §4.3.4, a larger initial thickness needs to be used relative to the small-amplitude case to avoid rapid film thinning over the crests that causes the 2D numerical scheme to fail. We choose $h_0 = 0.1$ and again take $M = 0.1$. For these parameters, the critical rotation rate calculated from Moffatt's load condition is $W_c = 2.01 h_0^2 M = 0.201$. We

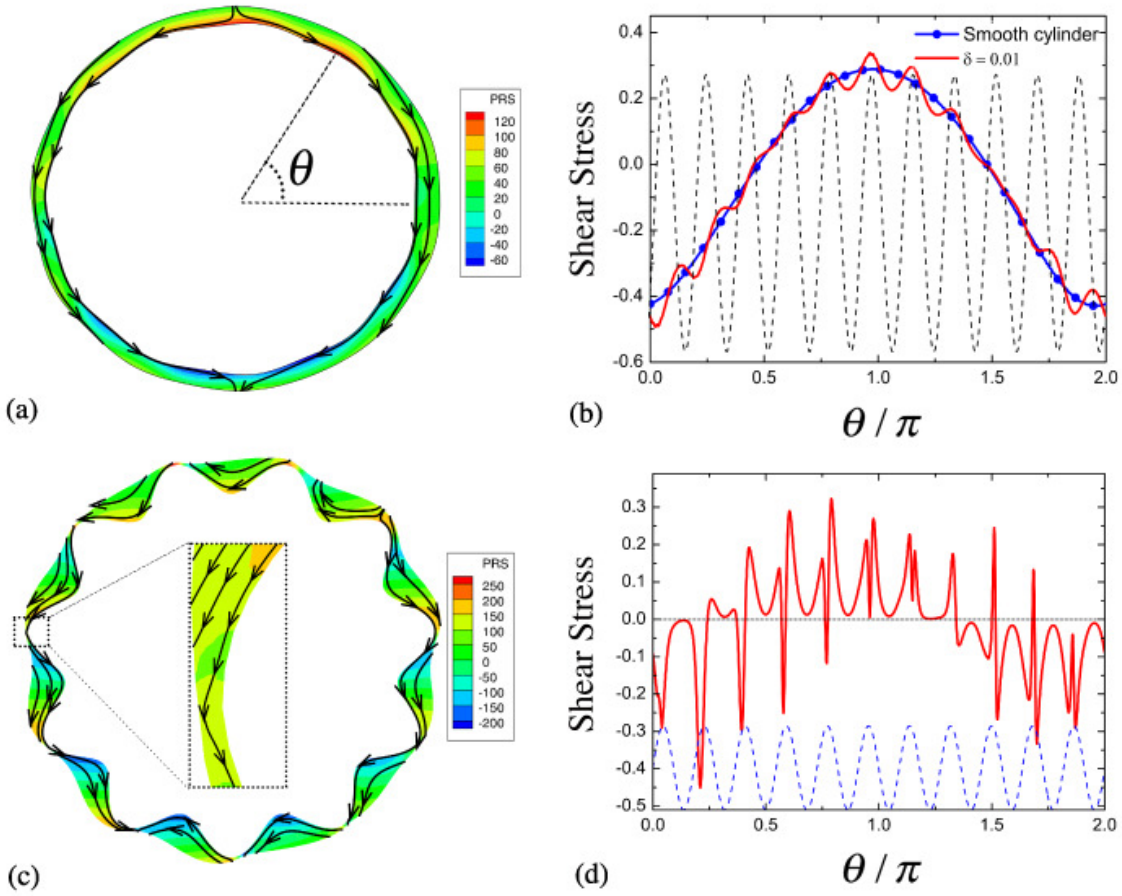

Figure 4.14: Streamline patterns, pressure distributions, and shear stress distributions along the cylinder surface with $h_0 = 0.01$ $W = 0.25$, $M = 0.1$, $\omega = 11$, and $Bo = 25$ at $t = 6545$ (25 revolutions). (a,b) $\delta = 0.01$ and (c,d) $\delta = 0.1$. Dashed lines indicate surface topography.

choose a representative value $W = 0.25 > W_c$ to ensure that the thinner film on the downward-moving side of the cylinder will not break. The case $W < W_c$ leads to the formation of a drop on the cylinder (cf. §4.4.1) and for brevity is not investigated here. We choose a representative value of $Bo = 25$; larger values lead to greater deformation of the free surface (by gravity) that we are not able to resolve computationally.

Fig. 4.14 shows the streamline patterns, pressure distributions, and shear stress distributions along the cylinder surface in the quasi-steady state for two different values of δ. The shear stress is calculated from $\tau = \mathbf{n} \cdot \mathbf{T} \cdot \mathbf{t}$, where $\mathbf{T}$ is the total stress tensor. The small-amplitude case ($\delta = 0.01$) presented in this figure serves to facilitate comparison with the larger-amplitude case. Contributions from rigid body rotation are excluded from the streamline patterns because they do not influence the relative motion of fluid elements or the free-surface shape.

For the small-amplitude pattern ($\delta = 0.01$; Fig. 4.14a), streamlines originate at the free surface on the upper side of the cylinder and end up at the free surface on the lower side. This corresponds to liquid being driven from the top and sides of the cylinder toward the cylinder bottom by gravitational forces. Near $\theta = \pi$, the corresponding absolute value of the shear stress, $|\tau|$ (Fig. 4.14b), decreases over the troughs and increases over the crests. This is due to the deceleration and acceleration of the fluid over the troughs and crests, respectively. Similar behavior was also observed for flows in a wavy channel [71] and over an inclined corrugated wall [35].

For the larger-amplitude pattern ($\delta = 0.1$; Fig. 4.14c),the streamlines originate and terminate at the free surface over each trough. Furthermore, the corresponding shear stress $|\tau|$ (Fig. 4.14d) exhibits local minima over the crests. This is in contrast to the small-amplitude case, and reflects rapid deceleration of fluid over the crests. Because the topography has a larger amplitude, the free-surface curvature is greater, and this tends to drive liquid into the troughs and hinder the gravity-driven drainage.

Since no flow recirculation is observed for $h_0 = 0.1$, simulations starting with a slightly thinner coating ($h_0 = 0.08$) and a thicker coating ($h_0 = 0.13$) are performed to investigate the influence of film thickness (Fig. 4.15). When the mean film thickness is smaller than the pattern amplitude ($h_0 = 0.08$; Fig. 4.15a), reverse flows form over the crests, and their direction is opposite to that of the gravity-driven drainage flow, preventing escape of liquid from the troughs. As a consequence, liquid that initially

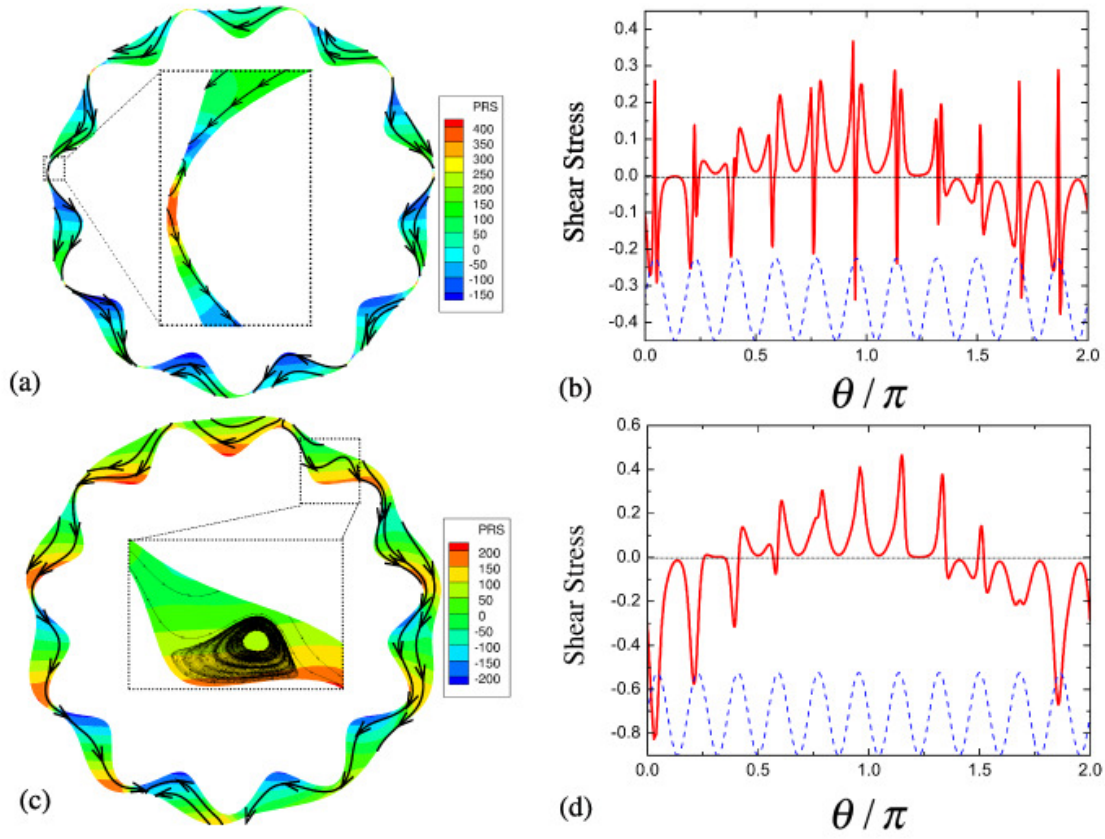

Figure 4.15: Streamline patterns, pressure distributions, and shear stress distributions along the cylinder surface with $W = 0.25$, $M = 0.1$, $\omega = 11$, $\delta = 0.1$, and $Bo = 25$ at $t = 6545$ (25 revolutions). (a, b) $h_0 = 0.08$ and (c, d) $h_0 = 0.13$. Dashed lines indicate surface topography.

accumulates inside a given trough will be kept there as the cylinder rotates. The enlargement of the boxed region in Fig. 4.15a demonstrates that these reverse flows can be attributed to the buildup of capillary pressure over the crests. As shown in Fig. 4.15b, the corresponding shear stress in the high-pressure regions (i.e., pattern crests) changes sign over the crests, indicating the acceleration of the liquid in the direction opposite to that of the gravity-driven drainage.

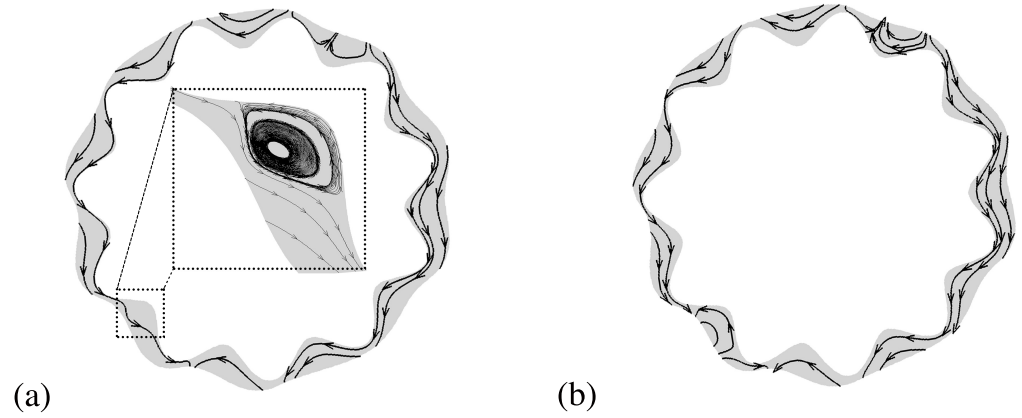

Figure 4.16: Streamline patterns with $W = 0.25$, $M = 0.1$, $\omega = 11$, $\delta = 0.1$, $Bo = 25$, and $h_0 = 0.13$ at (a) $t = 6548$ and (b) $t = 6551$.

When the mean film thickness is larger than the pattern amplitude ($h_0 = 0.13$; Fig. 4.15c), gravitational forces become more significant, which suppresses the flow reversal over the crests. However, a recirculation region now forms inside the trough on the upward-moving side of the cylinder, which may influence the mixing, mass transport, and heat transport in that region [35, 39, 40, 41]. A detailed study of this issue would be valuable but is beyond the scope of the present chapter.

To further characterize the recirculation regions, we plot in Fig. 4.16 the streamline patterns at slightly later times. Note that the three points in time selected in Fig. 4.15c, 4.16a and 4.16b are all within $1/\omega$ of a complete revolution. As the cylinder rotates, the first recirculation region vanishes, while a second one forms on the downward-moving side, as shown in Fig. 4.16a. Both recirculation regions vanish at a later stage (Fig. 4.16b) and will not form again until the coating is restored to the condition shown in Fig. 4.15c.

These phenomena can be understood by considering the variation in the pattern inclination angle. For film flow along an inclined wall with topography, it is known that recirculation regions form inside the troughs only when the film thickness is larger than some critical value. This critical value is highly sensitive to the substrate inclination angle [35, 36, 38]. For a patterned cylinder, the inclination angle of each trough varies constantly as the cylinder rotates, leading to an oscillation in the critical film thickness, and thus formation and vanishing of recirculation regions over time.

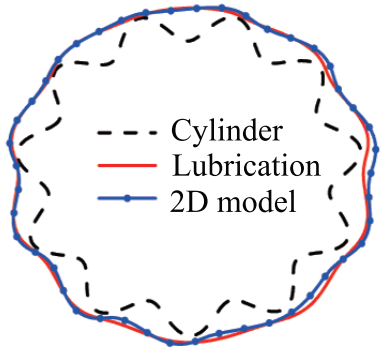

Figure 4.17: Free-surface profiles with $W = 0.25$, $M = 0.1$, $\omega = 11$, $\delta = 0.1$, $Bo = 25$, and $h_0 = 0.13$ at $t = 6545$ (25 revolutions).

To investigate the extent to which the lubrication model is still applicable, we show in Fig. 4.17 the free-surface profiles calculated with both the 2D model and the lubrication model for $\delta = 0.1$, $\omega = 11$, and $h_0 = 0.13$. The profiles show better agreement on the downward-moving side, where surface-tension forces overwhelm gravitational forces due to the smaller film thickness. The same parameter combination of h_0, δ, and ω is considered in the regime where centrifugal forces dominate (Fig. 4.9), and the lubrication model fails to describe the steady free-surface shape. Noting that $S = \rho\Omega^2 R_{\text{mean}}^3/\sigma = W^2 Bo$, we find that $S \sim 1$ for the calculations in Fig. 4.17, meaning that surface-tension forces are comparable to centrifugal forces. In contrast $S = 90$ in Fig. 10, and centrifugal forces dominate. We therefore infer that strengthening surface tension flattens the free surface, and as a result, the validity of the lubrication model improves.

Finally, we briefly summarize the results of some additional runs we have performed in which the topographical pattern has a trapezoidal-like shape. The trapezoidal-like

patterns are steeper than the sinusoidal patterns, and are relevant to the applications such as 3D printing (Fig. 1.4) mentioned in §4.1. Similar patterns have also been used to study thin-film flows on planar substrates [32, 72, 73, 3]. Similar to the planar case, we find that the film can form capillary ridges over the topography 'mounds', and that minima in the film thickness can develop near the mound corners. The sizes of the ridges and minima are non-uniform due to the non-uniformity of gravitational forces around the cylinder. Both the ridges and minima are usually undesired since the former create coating non-uniformity and the latter are especially susceptible to film rupture. As with the planar case, these features become more pronounced as the topographical features become steeper, and the lubrication model does not predict well the detailed free-surface shape near the pattern corners.

4.5 Conclusions

The results of this work demonstrate that even small-amplitude surface topography ($\sim$1% of the cylinder radius) can have a significant influence on thin-film flows on rotating cylinders. Results from a full 2D model agree well with those from a model based on lubrication theory provided that the free-surface curvatures are sufficiently small, an outcome which represents a significant benchmark for the lubrication model. In general, the free-surface curvatures become larger as the topography amplitude increases, and as a result, the accuracy of the lubrication model worsens.

For many practical applications, it is of interest to consider three-dimensional effects that arise due to surface topography or to Rayleigh-Taylor-like or Rayleigh-Plateau-like instabilities (e.g., see Ref. [74]). The lubrication model can readily be extended to 3D [15], and because 3D calculations are much less computationally expensive with the lubrication model, it provides an efficient vehicle for studying axial variations.

For certain applications, it may be desirable to use a coating to planarize a substrate. In other applications, a coating that conforms to the substrate topography is desired. Our results indicate that if gravitational forces become significant, then it should be possible to obtain a coating that closely conforms to the substrate topography due to the interplay between gravity, surface tension, and rotation (§4.4). Rotating the cylinder too quickly will initiate instabilities that result from a competition between surface tension

and centrifugal forces and interact in a complicated way with the surface topography (§4.3). Planarization would likely require a relatively thick initial coating followed by simultaneous rotation and drying to counteract the effects of gravitational drainage. Drying may initiate Marangoni flows [75, 46] due to temperature or composition effects, but the lubrication model can readily be extended to account for these effects.

Chapter 5

Viscous Free-Surface Flows on Rotating Elliptical Cylinders

Abstract - The flow of liquid films on rotating discrete objects having complicated cross-sections is encountered in coating processes for a broad variety of products. To advance fundamental understanding of this problem, we study viscous free-surface flows on rotating elliptical cylinders by solving the governing equations in a rotating reference frame using the Galerkin finite-element method (GFEM). Results of our simulations show that Hunt's maximum-load condition (Numer. Methods Partial Differential Eq. 24 (2008) 1094-1114), obtained in the absence of surface tension and centrifugal forces, is not significantly affected by these forces. The simulations are also used to track the transient behavior of the free surface. For $O(1)$ cylinder aspect ratios, cylinder rotation results in a drop-like liquid bulge hanging on the upward-moving side of the cylinder. This bulge shrinks in size due to surface tension provided that the liquid load is smaller than a critical value, leaving a relatively smooth coating on the cylinder. A decrease in cylinder aspect ratio leads to larger gradients in film thickness, but enhances the rate of bulge shrinkage and thus shortens the time required to obtain a smooth coating. Moreover, with a suitably chosen time-dependent rotation rotation rate, more liquid can be supported by the cylinder relative to the constant-rotation-rate case. For cylinders with even smaller aspect ratios, film rupture and liquid shedding may occur over the cylinder tips, so simultaneous drying and rotation along with the introduction

of Marangoni stresses will likely be especially important for obtaining a smooth coating.[1]

[1] This chapter has been published in [64].

5.1 Introduction

The flow of liquid films on non-flat substrates plays a central role in the manufacturing of products such as biomedical devices, automobiles, and food. These products, which represent non-flat substrates, often require a coating on them for purposes such as protection and appearance. The coating is formed by depositing one or several liquid layers onto the substrate and then solidifying the resulting film through drying. The final film thickness usually needs to lie within a specified range for the product to exhibit desired properties. However, controlling film thickness over a non-flat substrate is a challenging task not only due to surface curvature, but also the possible presence of object rotation.

The most commonly studied model geometry is that of a circular cylinder rotating about its horizontal axis [9, 11]. Moffatt [9] first considered this problem in the thin-film limit in the absence of both surface tension and inertia. In his pioneering work, he provided an analytical expression for the maximum supportable load (A_m^{Circular}) on a rotating cylinder, which can be written as

$$A_m^{\text{Circular}} = 1.057 \left(\frac{4\pi}{3} \right) \gamma^{-1/2}, \tag{5.1}$$

where $\gamma = ga\rho/\mu\Omega$ is the Stokes number, measuring the importance of gravitational forces relative to viscous forces. Here, a is the cylinder radius, ρ is the liquid density, g is the magnitude of the gravitational acceleration, μ is the liquid viscosity, and Ω is the cylinder rotation rate. The maximum load can be interpreted as a maximum mass or volume of liquid per unit length of the cylinder.

For a cylinder having load $A < A_m^{\text{Circular}}$, the cylinder can support the liquid and a so-called Moffatt-type smooth coating can be obtained in which there is a thicker film on the upward-moving side of the cylinder and a thinner film on the downward-moving side of the cylinder. Kelmanson [12] refined Moffatt's maximum load condition (5.1) by selectively retaining some higher-order terms that were not included in Moffatt's work.

For a cylinder having load $A > A_m^{\text{Circular}}$, no analytical solution exists in Moffatt's model since the film tends to sag under the action of gravity. Evans *et al.* [10] have extended Moffatt's model to include surface tension. Numerical solutions of their model show that surface tension tends to support the excess liquid when $A > A_m^{\text{Circular}}$, giving

rise to a drop-like liquid bulge hanging from the underside of the cylinder. Experimental investigations of the maximum supportable load condition have been undertaken by Kelmanson [12] and Preziosi and Joseph [13], and their results are in reasonable agreement with Moffatt's approximate criterion.

In many applications, such as the production of orthopedic implants [43], metal tubes [44], and food bars [45], the objects to be coated do not have a circular cross section. For these products, curvature variations along the circumference may trigger capillary flows that drive liquid from areas of high to low curvature. The resulting phenomena, including film rupture near sharp corners and uneven liquid and solute distribution, have the potential to adversely influence the quality of the final coating. Limited knowledge about the complex interplay between surface tension, gravity, and rotation in liquid-film flow on objects with non-circular cross-sections hinders the design and optimization of coating processes for these objects.

The influence of non-circular cross sections on coating flows on rotating objects was first studied by Hunt [76]. He considered two-dimensional Stokes flow on the exterior of an elliptical cylinder rotating with uniform angular speed about the center of the ellipse. Neglecting the effects of centrifugal forces and surface tension, he solved the full Stokes equations numerically and showed that the maximum amount of liquid that can be supported by an elliptical cylinder ($A_m^{\text{Elliptical}}$) is less than that in the circular case (A_m^{Circular}). In both cases, the maximum load decreases as the Stokes number increases (which corresponds to stronger effects of gravity), with approximately the same power-law dependence. Steady solutions were not found on an elliptical cylinder, in contrast to the circular-cylinder case. However, there exist periodic solutions when $A < A_m^{\text{Elliptical}}$, in which the solution is repeated after one full revolution of the cylinder. The present chapter extends the work of Ref. [76] to incorporate the effects of surface tension as well as centrifugal forces.

The governing equations and solution method are presented in §5.2. Results are presented in §5.3 and §5.4 for elliptical cylinders having $O(1)$ and $O(10^{-1})$ aspect ratios, respectively. We summarize our results and discuss the implications of our findings for coating of discrete objects in §5.5.

5.2 Mathematical model

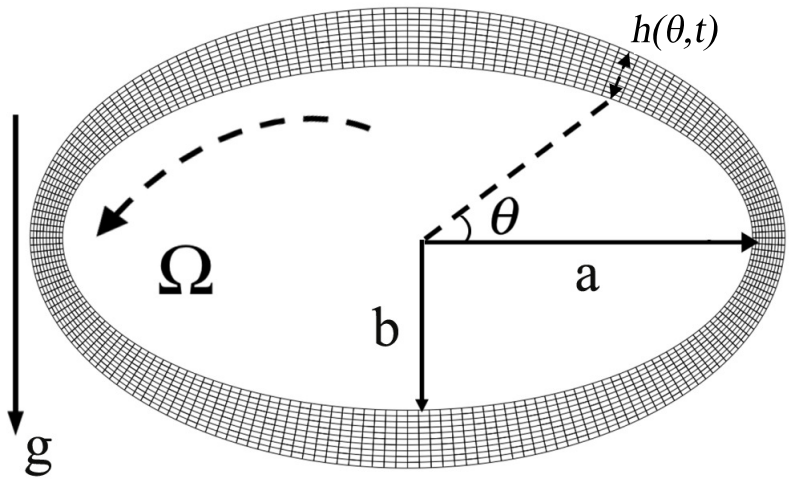

Figure 5.1: Sample finite-element mesh at $t = 0$ for a liquid film on an elliptical cylinder

We consider the free-surface flow of a Newtonian liquid with constant viscosity μ, density ρ, and surface tension σ on a rotating elliptical cylinder (Fig. 5.1). Our focus will be on the film-thickness evolution around the cylinder circumference, so thickness variations in the axial direction are neglected. The cylinder aspect ratio is $\alpha = b/a$, where a and b are the lengths of the semi-major and semi-minor axes, respectively. The cylinder surface $\mathbf{R}(x_0, y_0)$ is located at

$$x_0 = e\cosh\zeta_0\cos\nu, \qquad y_0 = e\sinh\zeta_0\sin\nu, \tag{5.2}$$

where $e = 1/\cosh(\zeta_0)$ is the eccentricity of the ellipse, $\zeta_0 = \frac{1}{2}\ln[(a+b)/(a-b)]$, and $\nu \in [0, 2\pi]$. The cylinder rotates about the center of the ellipse in the anti-clockwise direction at angular speed Ω.

5.2.1 Governing equations

We adopt a reference frame that rotates with the cylinder, and employ a Cartesian coordinate system with unit vectors $\mathbf{e}_x$, $\mathbf{e}_y$, and $\mathbf{e}_z$. The corresponding momentum conservation equation is [66]

$$\rho\left[\mathbf{u}_t + \mathbf{u}\cdot\boldsymbol{\nabla}\mathbf{u}\right] = -\boldsymbol{\nabla}p + \mu\nabla^2\mathbf{u} - \rho\boldsymbol{\Omega}\times(\boldsymbol{\Omega}\times\mathbf{r}) - 2\rho\boldsymbol{\Omega}\times\mathbf{u} - \rho\boldsymbol{\Omega}_t\times\mathbf{r} + \rho\mathbf{g}, \tag{5.3}$$

where p is pressure, $\mathbf{u}$ is the velocity vector, $\mathbf{g} = g\mathbf{e}_g = -g\sin(\Omega t)\mathbf{e}_x - g\cos(\Omega t)\mathbf{e}_y$ is the gravitational acceleration, $\mathbf{\Omega} = \Omega \boldsymbol{e}_z$ is the angular velocity vector, and $\mathbf{r}$ is the position vector of a fluid element.

Inspired by prior work on circular cylinders [10], we scale length with a, velocity with $U = \rho g a^2/\mu$, time with a/U, and pressure with $\mu U/a$. We can define two Reynolds numbers, $Re = \rho^2 g a^3/\mu^2$, based on a gravitational drainage velocity (U), and $Re_\Omega = \rho\Omega a^2/\mu$, based on the cylinder velocity ($a\Omega$). The scaled governing equations for mass and momentum conservation are

$$\boldsymbol{\nabla} \cdot \mathbf{u} = 0, \tag{5.4}$$

$$Re[\mathbf{u}_t + \mathbf{u} \cdot \boldsymbol{\nabla}\mathbf{u}] = -\boldsymbol{\nabla} p + \nabla^2 \mathbf{u} - W^2 \mathbf{r} - Re_\Omega(2\mathbf{e}_z \times \mathbf{u} + \mathbf{e}_z \times \mathbf{r}) + \mathbf{e}_g, \tag{5.5}$$

where $W = \Omega/\sqrt{g/a}$ is the dimensionless rotation rate.

There are three inertia-related terms in Eq. (5.5): the standard inertial term ($Re[\mathbf{u}_t + \mathbf{u}\cdot\boldsymbol{\nabla}\mathbf{u}]$), the Coriolis term ($Re_\Omega(\mathbf{e}_z \times \mathbf{u})$), and the centrifugal term ($W^2\mathbf{r}$). The last of these terms arises from the standard inertial term in a stationary reference frame. Following Refs. [10] and [67], we focus on the effects of centrifugal forces and neglect the other two inertia-related terms. With these simplifications, Eq. (5.5) becomes

$$\mathbf{0} = -\boldsymbol{\nabla} p + \nabla^2 \mathbf{u} - W^2 \mathbf{r} + \mathbf{e}_g. \tag{5.6}$$

The boundary conditions at the cylinder surface, $\mathbf{R}(x_0, y_0)$, are no-slip and no-penetration,

$$\mathbf{t} \cdot \mathbf{u} = 0, \quad \mathbf{n} \cdot \mathbf{u} = 0, \tag{5.7}$$

where $\mathbf{n}$ and $\mathbf{t}$ are the unit outward normal and tangent vectors. At the free surface, $\mathbf{r}_s(x, y)$, we have the kinematic and interfacial-stress boundary conditions,

$$\mathbf{n} \cdot \mathbf{u} = \mathbf{n} \cdot \dot{\mathbf{r}_s}, \tag{5.8}$$

$$\mathbf{n} \cdot \mathbf{T} = -\frac{\kappa}{Bo}\mathbf{n}, \tag{5.9}$$

where $\mathbf{T}$ is the total stress tensor (the components of which are nondimensionalized by $\mu U/a$), $\kappa = \boldsymbol{\nabla} \cdot \mathbf{n}$ is the surface curvature, and $\dot{\mathbf{r}_s}$ is the free-surface velocity. The Bond number, $Bo = \rho g a^2/\sigma$, measures the importance of gravity relative to surface tension.

5.2.2 Solution method

Equations (5.4) and (5.6) with boundary conditions (5.7), (5.8), and (5.9) are solved with the Galerkin finite-element method (GFEM) [68, 63]. Order-of-magnitude estimates for key dimensional quantities are listed in Table 5.1. Details about this method is given in Appendix C.

Following Hunt [76], we perform simulations with an initial coating shown in Fig. 5.1, whose inner surface is described by Eq. (5.2) and outer surface, $\mathbf{r}_s(x, y)$, is given by

$$x = e\cosh(\zeta_0 + \zeta)\cos\nu, \qquad y = e\sinh(\zeta_0 + \zeta)\sin\nu. \tag{5.10}$$

Here, the constant ζ determines the load A_0 of fluid deposited onto the cylinder, which is taken to be the area between the cylinder surface and the free surface [76],

$$A_0 = \int_0^{2\pi} \frac{e^2}{4}\{\sinh\left(2(\zeta_0 + \zeta)\right) - \sinh(2\zeta_0) - 2\zeta\cos(2\nu)\}d\nu. \tag{5.11}$$

For the loads considered in this chapter, the initial film thickness is typically ∼10-20% of the length of the semi-major axis. While in principle the lubrication approximation could be applied to develop a simplified model equation [77], in practice this is cumbersome due to the complicated surface geometry. Our GFEM scheme also has the advantage of being applicable to objects with surfaces for which no analytical description is available.

For our calculations, 2000 elements (200 elements in the axial direction and 10 elements in the radial direction) were found to be sufficient. To ensure conservation of mass, we calculate the percent deviation of the liquid load using $\epsilon = 100(A_{\max} - A_{\min})/A_0$, where $A_{\max}$ and $A_{\min}$ are the maximum and minimum area during the entire calculation. Results of our simulations are considered accurate if $\epsilon < 0.1$ [68].

For a fixed set of problem parameters (W, A_0, Bo, and α), we use the GFEM to numerically solve for the location of the free surface as a function of time. To track the film evolution, we then extract the film thickness, $h(\theta, t)$, as a function of time and the angular position, θ, in a reference frame rotating with the cylinder. The film thickness is measured in the direction normal to the cylinder surface from a point on the cylinder surface whose angular position is θ (Fig. 5.1).

Table 5.1: Order-of-magnitude estimates of dimensional quantities. The viscosity, density, and surface tension are representative of a glycerol-water mixture.

Constants	Typical values
Length of the semi-major axis, a (cm)	1
Cylinder aspect ratio, α,	0.1-1
Film thickness, H (cm),	0.01-0.1
Rotation rate, Ω (rad/s)	10
Viscosity, μ (cP)	300
Density, ρ (g/cm^3)	1
Surface tension, σ (dyn/cm)	100

Table 5.2: Dimensionless problem parameters

Parameter	Representation	Physical meaning	Typical value
M	$\mu/\rho\sqrt{ga^3}$	Dimensionless viscosity	0.1
W	$\Omega/\sqrt{g/a}$	Dimensionless rotation rate	0.1
Bo	$\rho g a^2/\sigma$	Gravitational force/Surface-tension force	10
Re	$\rho^2 g a^3/\mu^2$	Inertia forces/viscous forces	100
Re_Ω	$\rho\Omega a^2/\mu$	Inertia forces/viscous forces	1

5.3 Results: $O(1)$ aspect ratio

In this section, we consider elliptical cylinders with $O(1)$ aspect ratios ($0.5 \leqslant \alpha \leqslant 1$).

5.3.1 Zero-gravity case

We first consider the case where the cylinder rotates rapidly and the effects of gravity can be neglected. In this regime, the drainage rate can no longer be used as the characteristic velocity, so we rescale the governing equations (5.4) and (5.6) using σ/μ and σ/a as the new characteristic velocity and pressure (stress) respectively [63]. The resulting dimensionless governing equations become

$$\boldsymbol{\nabla} \cdot \mathbf{u} = 0, \tag{5.12}$$

$$\mathbf{0} = -\boldsymbol{\nabla} p + \nabla^2 \mathbf{u} - We\mathbf{r}, \tag{5.13}$$

where $We = \rho\Omega^2 a^3/\sigma$ is the Weber number and provides a measure of the strength of centrifugal forces relative to surface-tension forces. Larger We corresponds to faster rotation rates and stronger centrifugal forces acting on the liquid.

For a circular cylinder ($\alpha = 1$), Evans *et al.* [10] showed that small perturbations to an initial film of uniform thickness tend to grow in amplitude under the action of centrifugal forces, leading to the formation of small droplets evenly spaced around the cylinder circumference. For a sufficiently thin initial film, the film will eventually reach a steady state in which the number of droplets, N, is a function of We and has the form

$$N = [\sqrt{(1 + We)/2}], \tag{5.14}$$

where $[x]$ is the greatest integer less than x. The time scale over which the steady state is reached (maximum growth rate) is proportional to $\sigma h_0^3 (1 + We)^2/(3\mu a^4)$, where h_0 is the initial film thickness [10].

To investigate the case of elliptical cylinders, we solve equations (5.12) and (5.13) numerically for different cylinder aspect ratios α. We pick an initial load $A_0 = 0.2$ and a rotation rate $We = 160$ as a representative case. Similar to the circular-cylinder case, a steady state (in the rotating reference frame) is reached; the resulting free-surface

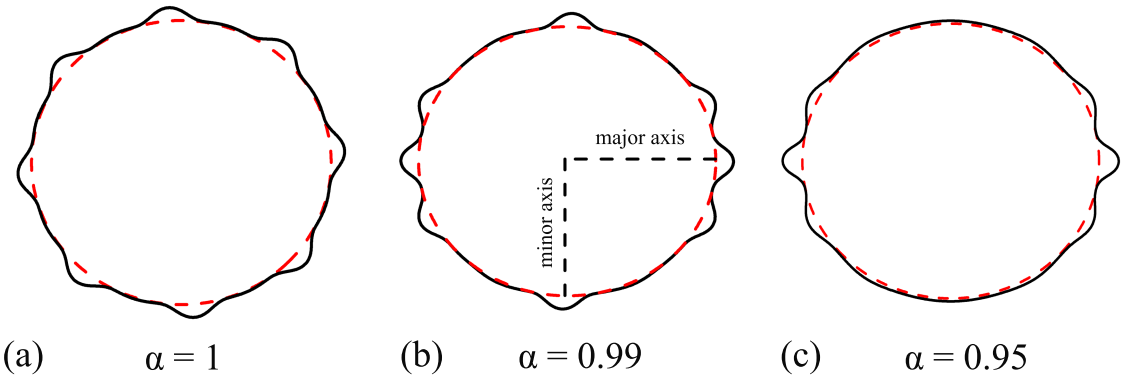

Figure 5.2: Steady free-surface profiles on rotating cylinders with $A_0 = 0.2$ and $We = 160$ ($N = 8$) for three different values of the cylinder aspect ratio. The red dashed lines indicate the cylinder surface.

profiles are shown in Fig. 5.2b and 5.2c for $\alpha = 0.99$ and 0.95. The steady free-surface profile on a circular cylinder is shown in Fig. 5.2a for comparison. Steady stares reported here and elsewhere in this chapter are long-time solutions rather than direct solutions, and so should be regarded as apparent steady states.

For $We = 160$, the corresponding value of N calculated from equation (5.14) is eight. Fig. 5.2a shows that eight droplets of almost the same size develop on the circular cylinder, and they are evenly spaced around the cylinder circumference and connected by very thin films. With a slight decrease in α (Fig. 5.2b), the number of droplets is still eight, but these droplets are unevenly spaced and some of the droplets tend to shift to the cylinder tips. As we further decrease α to a value of 0.95 (Fig. 5.2c), only six droplets develop on the elliptical cylinder, and the two droplets over the cylinder tips are much larger than the rest of the droplets.

Since stronger centrifugal forces acting on the liquid over the tips tend to draw liquid from surrounding areas, droplets are more stable near the tips, causing the uneven spacing between droplets in Figs. 5.2b and 5.2c. A decrease in α strengthens the gradient in centrifugal forces, which produces two main droplets over the tips but greatly suppresses the growth of droplets in the surrounding areas. This explains the uneven droplet sizes and the decrease in the number of droplets in Fig. 5.2c.

For even smaller cylinder aspect ratios ($\alpha < 0.95$), the larger variation in substrate

curvature leads to stronger capillary pressure gradients that tend to drive liquid away from the tips. Because this phenomenon is also seen with cylinders having small aspect ratios ($\alpha < 0.5$), we discuss it in §5.4.1.

5.3.2 Gravity effects

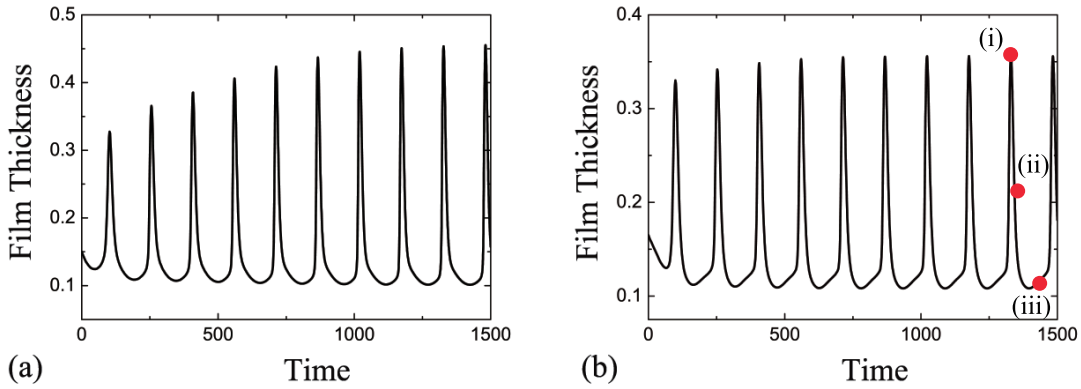

Figure 5.3: Time-variation of film thickness at $\theta = \pi/2$ with $Bo = 12.5$, $M = 0.1$, $W = 0.43$, and (a) $A_0 = 1$ and $\alpha = 1$ (circular cylinder), (b) $A_0 = 0.75$ and $\alpha = 0.5$. The corresponding free-surface profiles at times (i), (ii), and (iii) are shown in Fig. 5.4.

For the case where gravitational effects are significant, Moffatt [9] developed an expression for the maximum load that can be supported on a rotating circular cylinder (equation (5.1)) in the thin-film regime. Kelmanson [12] proposed a refinement to Moffatt's criterion that selectively retains some higher-order terms and provided an explicit expression for the maximum load (equation (4.13) in Ref. [12]). Both Moffatt and Kelmanson neglected the effects of surface tension and inertia in their work.

Evans *et al.* [10] used lubrication theory to derive a nonlinear evolution equation for the film thickness on a rotating circular cylinder in the presence of surface tension and centrifugal forces which was then solved numerically. To confirm Moffatt's criterion, they tracked the time-evolution of the film thickness at a fixed point in space in a fixed reference frame.

For $A > A_m^{\text{Circular}}$ (equation (5.1)), excess liquid drains under the action of gravity and forms a drop-like bulge on the cylinder underside, supported by surface tension. The film thickness there increases monotonically until the coating reaches a steady state

within a few revolutions. For $A < A_m^{\text{Circular}}$, the drop-like bulge rises over the cylinder symmetry plane and is carried around the cylinder in the direction of rotation. The rotation rate of the bulge is less than but comparable to the cylinder rotation rate [10]. Simultaneously, the bulge shrinks in size and the film approaches a Moffatt-type smooth coating (§5.1) with a thicker film on the upward-moving side of the cylinder and a thinner film on the downward-moving side of the cylinder. As a consequence, the film thickness at a given point exhibits a decaying oscillation with roughly constant frequency (Fig. 7 in Ref. [10]).

Similar calculations are performed in this work to approximately determine the maximum load that can be supported by an elliptical cylinder. However, it is more convenient to track the film evolution at a fixed point on the cylinder surface in our model since we consider the problem in a rotating reference frame.

Following Ref. [10], one can define a dimensionless viscosity, $M = \mu/\rho\sqrt{ga^3}$, which controls the time scale of the flow. For the parameter values given in Table 5.1, the dimensionless viscosity and the Bond number are $M = 0.1$ and $Bo = 12.5$ respectively. We choose a dimensionless rotation rate $W = 0.43$ as a representative case; the corresponding maximum supportable load on a circular cylinder calculated from Kelmanson's criterion [12] is $A_m^{\text{Circular}} = 0.96$. The dimensionless rotation period of the cylinder is $2\pi/MW$.

Simulations were performed with $A_0 = 1 > A_m^{\text{Circular}}$ first. For a circular cylinder, we plot in Fig. 5.3a the time-evolution of the film thickness at $\theta = \pi/2$ on the cylinder surface. For an elliptical cylinder with $\alpha = 0.5$, we found that the film thickness at the cylinder bottom grows rapidly and could no longer be resolved numerically after one revolution. To avoid this, we decreased A_0 (initial load) until a periodic state was reached where the coating restores its shape after every half-revolution. This occurred when $A_0 = 0.75$, and we show in Fig. 5.3b the time-evolution of the film thickness at $\theta = \pi/2$.

For both the circular cylinder (Fig. 5.3a) and elliptical cylinder (Fig. 5.3b), the film thickness at $\theta = \pi/2$ oscillates with a fixed frequency. The amplitudes of the oscillations increase monotonically until they reach steady values at later times. Oscillations in both cases can be attributed to the formation of a liquid bulge, so we focus on the elliptical cylinder in the following discussion. We have selected several times during the later

stage of the time-evolution in Fig. 5.3b and plot the corresponding free-surface profiles in Fig. 5.4.

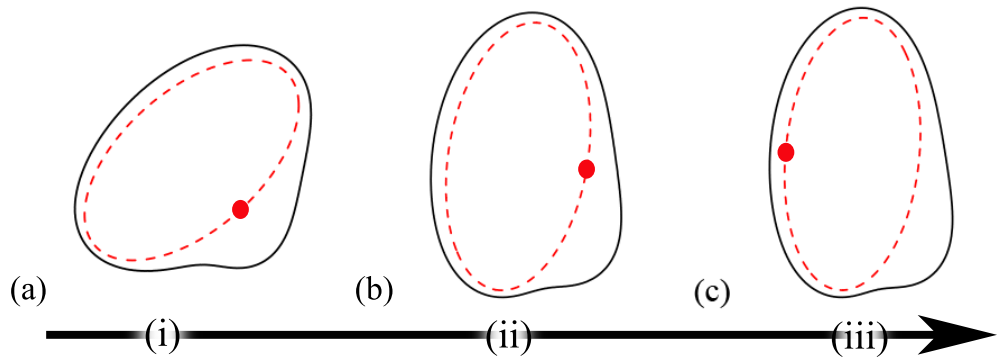

Figure 5.4: Free-surface profiles on an elliptical cylinder at three given times (marked in Fig. 5.3b). The red dots indicate the $\theta = \pi/2$ point on the cylinder surface.

As seen in Fig. 5.4, excess liquid forms a drop-like bulge, supported by surface tension, near the underside of the cylinder. As a result, the film thickness over $\theta = \pi/2$ reaches its maximum when this point rotates into the bulge area (Fig. 5.4a). As more liquid is driven into the bulge due to gravity, it grows in size, which explains the increasing amplitude in Fig. 5.3b. The coating reaches a quasi-steady state where the free-surface shape changes periodically due to the variation in the cylinder orientation. The free-surface tends to restore its shape after every half-revolution as shown in Figs. 5.4b and 5.4c.

To investigate the regime where the load A_0 is relatively low, we plot in Fig. 5.5 the time-evolution of the film thickness at $\theta = \pi/2$ with $W = 0.43$ and $A_0 = 0.72 < A_m^{\text{Circular}}$ for three different values of α. For all of these three values, the film thickness at $\theta = \pi/2$ oscillates with a fixed frequency similar to the larger-load case (shown in Fig. 5.3). However, the oscillation amplitude does not grow monotonically with time, in contrast to the case where $A_0 > A_m^{\text{Elliptical}}$ (Fig. 5.3; note that $0.72 < A_m^{\text{Elliptical}} < 0.75$). For $\alpha = 1$ (Fig. 5.5a) and $\alpha = 0.8$ (Fig. 5.5b), the corresponding upper-envelope functions oscillate with decaying amplitudes, while for $\alpha = 0.5$ (Fig. 5.5c), the upper-envelope function decays almost monotonically, and the film reaches a quasi-steady state at a much earlier time. These three cases are discussed below in more detail.

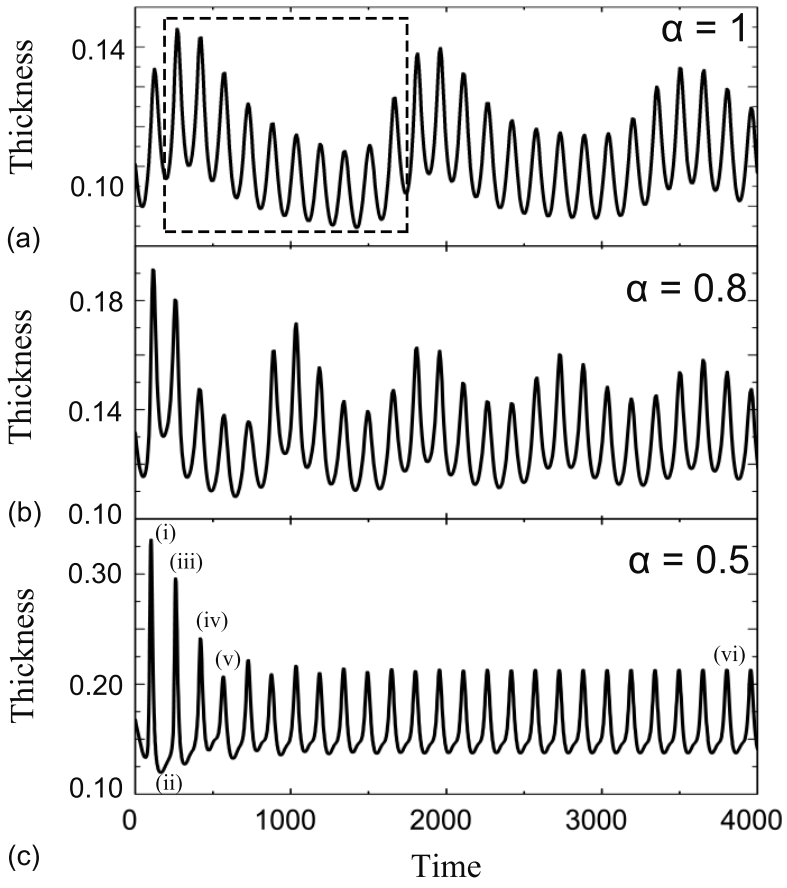

Figure 5.5: Time-variation of film thickness at $\theta = \pi/2$ with $Bo = 12.5$, $M = 0.1$, $W = 0.43$, and $A = 0.72$ for three different values of α. The enlargement of the region marked in panel (a) is shown in Fig. 5.6. The corresponding free-surface profiles at times (i)-(vi) marked in panel (c) are shown in Fig. 5.7.

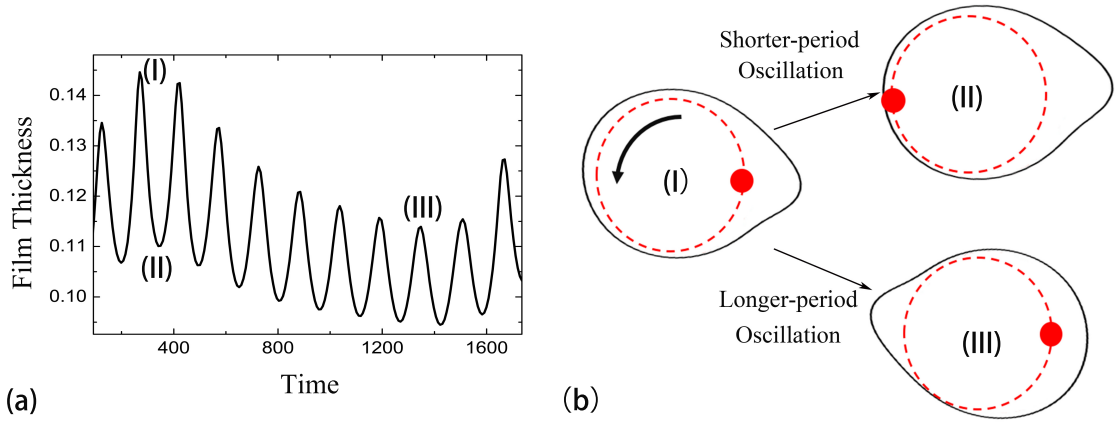

Figure 5.6: (a) Enlargement of the region marked in Fig. 5.5a. (b) Schematics of the free-surface profiles at times (I), (II), and (III) marked in panel (a). The red dots indicate the $\theta = \pi/2$ point on the cylinder surface (red dashed line).

For a circular cylinder, the superposition of a shorter-period oscillation and a longer-period oscillation results in the time-evolution of film thickness plotted in Fig. 5.5a. To gain deeper insight, we show in Fig. 5.6a the enlargement of the boxed region in Fig. 5.5a. Schematics of the free-surface profiles at three times (marked (I)-(III) in Fig. 5.6a) are shown in Fig. 5.6b to explain the mechanisms behind the shorter-period oscillation and the longer-period oscillation. Since the film-thickness variation at a fixed point is small relative to the thickness of the film, schematics rather than actual free-surface profiles are shown for ease of visualization.

Due to the effects of rotation and gravity, a coating on a rotating circular cylinder is thicker on the upward-moving side and thinner on the downward-moving side [9]. As a consequence, the film thickness at $\theta = \pi/2$ decreases as the $\theta = \pi/2$ point on the cylinder surface (red dots in Fig. 5.6b) rotates from the upward-moving side to the downward-moving side (from time (I) to time (II) in Fig. 5.6b) and increases as the $\theta = \pi/2$ point rotates back to the upward-moving side. This is the origin of the shorter-period oscillation in film thickness. The oscillation period equals the time required for the cylinder to complete one revolution. A similar mechanism is also responsible for the time-evolution of film thickness shown in Fig. 5.3a, where the load is too large to obtain a Moffatt-type smooth coating.

Due to gravity-driven drainage, excess liquid forms a bulge near the underside of

the cylinder. When $A_0 < A_m^{\text{Circular}}$, this bulge is carried around the cylinder in the direction of rotation with a speed that is slower than the speed of cylinder rotation, and the bulge shrinks in size with time [10]. The rotation of the bulge causes an oscillation in film thickness at $\theta = \pi/2$ (time (I) and time (III) in Fig. 5.6b) with a decaying amplitude and a longer period relative to the oscillation triggered by a nonuniform liquid distribution (time (I) and time (II) in Fig. 5.6b). The resulting longer-period oscillation is superimposed on the shorter-period oscillation, causing the transient behavior shown in Fig. 5.5a to be different from that in the high-load case (Fig. 5.3a), where the bulge stays on the upward-moving side of the cylinder.

A similar time-evolution of film thickness is also observed in the case where $\alpha = 0.8$ (Fig. 5.5b). However, both the initial oscillation amplitude and the frequency of the longer-period oscillation are larger compared to the circular-cylinder case (Fig. 5.5a). As will be shown later in this section, a smaller cylinder aspect ratio means that less liquid can be supported on the cylinder. As a consequence, a larger bulge will form at early times, and this explains the larger oscillation amplitude. Since a decrease in the cylinder aspect ratio also shortens the circumference of the cylinder, less time is required for the bulge to complete one revolution around an elliptical cylinder, which leads to a higher frequency of the longer-period oscillation in Fig. 5.5b.

With a further decrease in α to a value of 0.5 (Fig. 5.5c), the oscillation amplitude decays almost monotonically, in contrast to the larger-aspect-ratio cases (Figs. 5.5a and 5.5b). The coating reaches a quasi-steady state within just ten revolutions, indicating a different mechanism underlying the shrinkage of the bulge. To investigate this, we select five times during the early transient stage (labeled (i)-(v) in Fig. 5.5c) and one time point during the quasi-steady stage (labeled (vi) in Fig. 5.5c), and plot the corresponding film-thickness profiles and free-surface profiles in Fig. 5.7.

Figs. 5.7a and 5.7b show that a liquid bulge forms on the upward-moving side of the cylinder due to gravity-driven drainage. The shape of the bulge varies to accommodate the variation in the cylinder orientation, but the bulge stays on the upward-moving side of the cylinder. Film thickness profiles at four times within the first four revolutions are shown in Fig. 5.7c; the times are chosen so that the orientation of the cylinder is the same. The film thickness takes on its maximum value in the bulge ($\theta = \pi/2$), which decreases monotonically in size after each revolution. This indicates that the liquid bulge

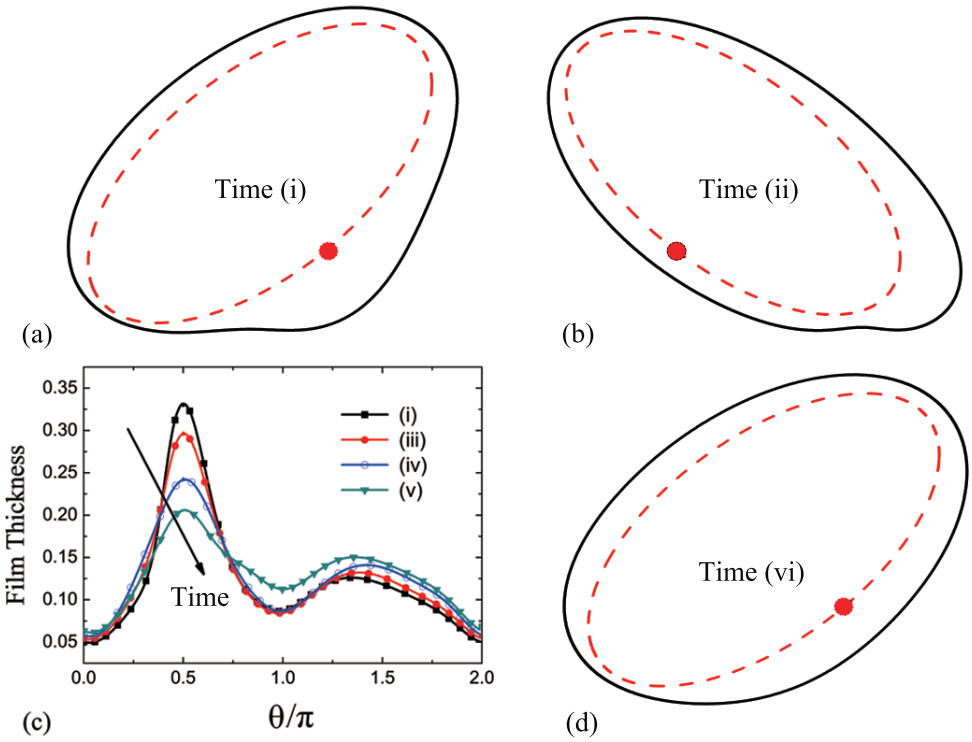

Figure 5.7: (a, b, d) Free-surface profiles at three given times (marked in Fig. 5.5c). (c) Film-thickness profiles in a rotating frame of reference at four given times (marked in Fig. 5.5c) with $\alpha = 0.5$, $Bo = 12.5$, $M = 0.1$, $W = 0.43$, and $A_0 = 0.72$. The red dots indicate the $\theta = \pi/2$ point on the cylinder surface.

on an elliptical cylinder can shrink in size even without rotating around the cylinder, in contrast to the circular-cylinder case. The mechanism underlying this phenomenon is discussed below. A comparison between Figs. 5.7a and 5.7d shows that liquid keeps being driven away from the bulge to the downward-moving side of the cylinder. As a consequence, a coating with relatively small variation in free-surface curvature (i.e. a smooth coating) can be obtained at a later time (Fig. 5.7d).

To understand the driving force behind the bulge shrinkage shown in Fig. 5.7c, we plot in Fig. 5.8b the time-evolution of film thickness at $\theta = \pi/2$ on an elliptical cylinder with $\alpha = 0.5$ for two different values of Bo. The time-evolution of the film thickness on an elliptical cylinder with $\alpha = 0.8$ is shown in Fig. 5.8a for comparison. For $\alpha = 0.8$, varying Bo barely influences the coating evolution. This can be attributed to the fact

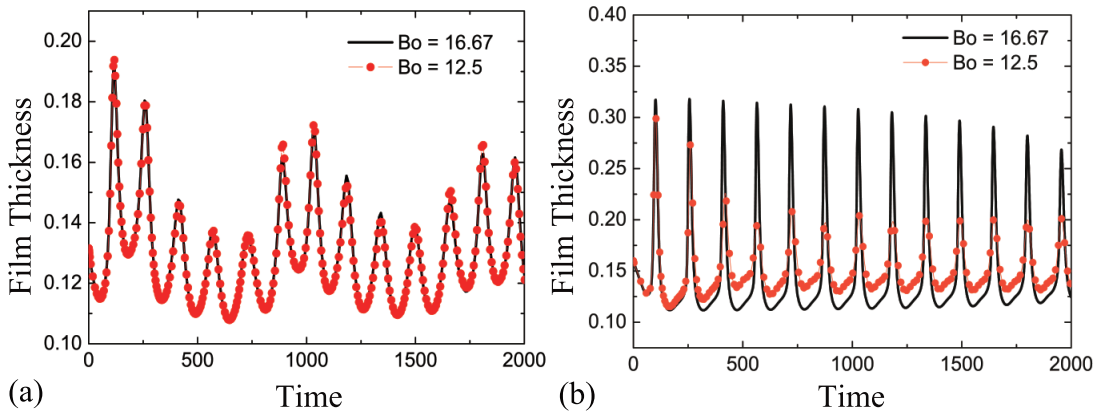

Figure 5.8: Time-variation of film thickness at $\theta = \pi/2$ for two different values of Bo with $M = 0.1$, $W = 0.43$, $A_0 = 0.72$ and (a) $\alpha = 0.8$ and (b) $\alpha = 0.5$.

that liquid bulge shrinks in size due to the rotation of the bulge, which redistributes liquid around cylinder, and surface tension plays a minor role in this process.

With a decrease in α to a value of 0.5 (Fig. 5.8b), the oscillation in film thickness becomes more pronounced (much larger oscillation amplitude), which indicates a larger liquid bulge forming during the early stages. In addition, the film-thickness evolution is highly sensitive to the value of Bo; a larger value of Bo leads to a smaller decay rate. Due to the increase in the bulge size, the viscous dragging caused by cylinder rotation is not strong enough to cause significant motion of the bulge when α is sufficiently small, so it stays on the upward-moving side of the cylinder (Figs. 5.7a and 5.7b). Since surface tension makes a significant contribution to the film-thickness evolution only in regions where large variations in free-surface curvature occur [10] (i.e., the vicinity of the bulge), it tends to drive liquid away from the bulge, which eventually leads to a relatively smooth coating (Fig. 5.7d). For this reason, a decrease in Bo, which corresponds to stronger surface-tension forces, enhances the damping of oscillations in film thickness (Fig. 5.8b), and thus shortens the time required to obtain the smooth coating.

A comparison between Fig. 5.4 ($A_0 = 0.72$) and Fig. 5.7d ($A_0 = 0.75$) shows that there exists a maximum load, $A_m^{\text{Elliptical}}$, such that for $A_0 < A_m^{\text{Elliptical}}$ a relatively smooth coating can be obtained on an elliptical cylinder. Since such coatings may be desired for many applications, it is important to characterize the behavior of the maximum load. To do so, we perform simulations by varying A_0 for given values of W, α, Bo, and

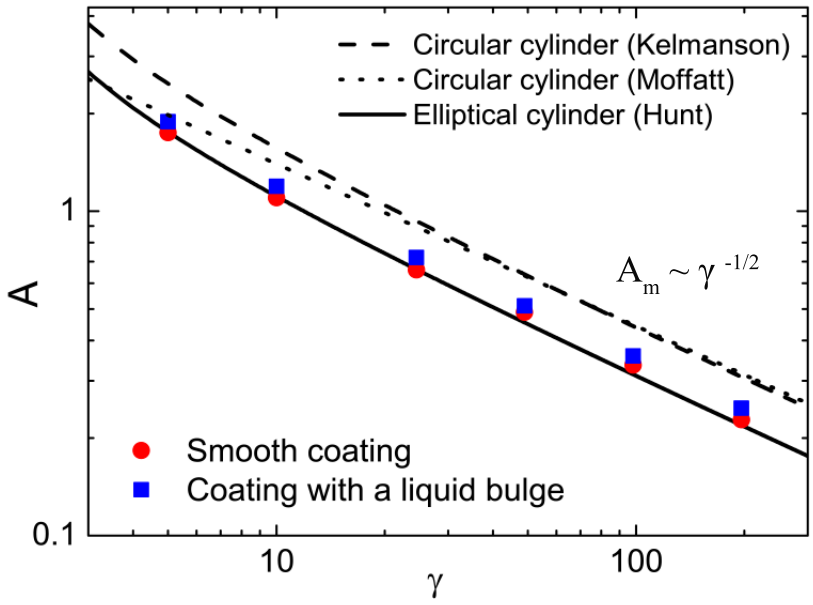

Figure 5.9: Maximum load on an elliptical cylinder with $\alpha = 0.5$ and $Bo = 12.5$. Results of Moffatt [9], Kelmanson [12] and Hunt [76] are indicated by a dashed line, a dotted line, and a solid line, respectively.

M using initial condition (5.10). Oscillations in film thickness in the small-load cases should decay in amplitude (Fig. 5.5), while oscillations in the large-load cases should grow (Fig. 5.3).

For a circular cylinder, Moffatt [9] reported that there is a power-law relationship between the maximum load and the Stokes number, $A_m^{\text{Circular}} \sim \gamma^{-1/2}$, where $\gamma = 1/MW$ is the Stokes number (equation (5.1)). Kelmanson [12] pointed out that this power-law dependence only holds when γ is sufficiently large, and that Moffatt's criterion increasingly underestimates the maximum load with a decrease in γ. For elliptical cylinders, a similar power-law dependence is reported by Hunt [76] in the regime where surface-tension and centrifugal forces are negligible.

Inspired by the above works, we plot the load, A, as a function of γ in Fig. 5.9 for $\alpha = 0.5$. The lower points (red circles) indicate the largest load that will result in a relatively smooth coating, and the upper points (blue squares) indicate the smallest load that will cause the growth of the liquid bulge. Results of Moffatt [9], Kelmanson [12], and Hunt [76] are shown in the same figure for comparison. As can be seen, our

results agree well with those of Hunt.

For both a circular cylinder and an elliptical cylinder, Fig. 5.9 shows that increasing the Stokes number, which corresponds to stronger gravity-driven drainage, leads to a smaller maximum load. For a given value of γ, the maximum load on an elliptical cylinder is always smaller than that on a circular cylinder, but their ratio, $A_m^{\text{Elliptical}}/A_m^{\text{Circular}}$, is fairly constant (0.71) for $\alpha = 0.5$ over the range of γ investigated [76]. Both the circular and elliptical cylinders, there is approximately the same power-law dependence between the maximum load and γ, $A_m \sim \gamma^{-1/2}$.

The decrease in A_m can be rationalized by noticing that the liquid drainage rate is highly dependent on the orientation of the cylinder and the length of the minor axis, b. When the minor axis is perpendicular to the gravity vector, $\mathbf{g}$ (defined in §5.2.1), the liquid drainage rate takes on its maximum, and the maximum value itself increases with decreasing b. For a given value of cylinder rotation rate, a smaller cylinder aspect ratio, $\alpha = b/a$, gives rise to a larger mean rate of liquid drainage, and for this reason, less liquid can be supported on the cylinder.

In Fig. 5.9, results from Hunt's model and our model are in good agreement, despite the fact that effects of surface tension and centrifugal forces are neglected in Hunt's model. Good agreement is also observed in the case where $\alpha = 0.8$, but the results are not shown here for brevity. Based on these observations, we infer that surface tension does not significantly influence the maximum load below which a relatively smooth coating can be obtained on an elliptical cylinder, but it does significantly influence the time needed to obtain such a coating (Fig. 5.8b).

5.3.3 Time-dependent cylinder rotation rate

When $A > A_m^{\text{Elliptical}}$, liquid tends to accumulate near the underside of the cylinder due to gravity-driven drainage, and the rate of liquid drainage is highly dependent on the orientation of the cylinder (Fig. 5.4). We show in this section that varying the cylinder rotation rate based on cylinder orientation can allow us to obtain a relatively smooth coating with a mean rotation rate that is smaller than the critical value shown in Fig. 5.9.

For brevity, we consider the simplest case where the rotation rate, W, varies periodically as cylinder rotates,

$$W(t) = W_m - \delta \cos(2W_m M t), \tag{5.15}$$

where W_m is a constant mean rotation rate and δ is a constant that sets the oscillation amplitude. This sinusoidal function basically ensures that the rotation rate takes on its minima ($W_m - \delta$) when the major axis is perpendicular to $\mathbf{g}$ and its maxima ($W_m + \delta$) when the major axis is parallel to $\mathbf{g}$.

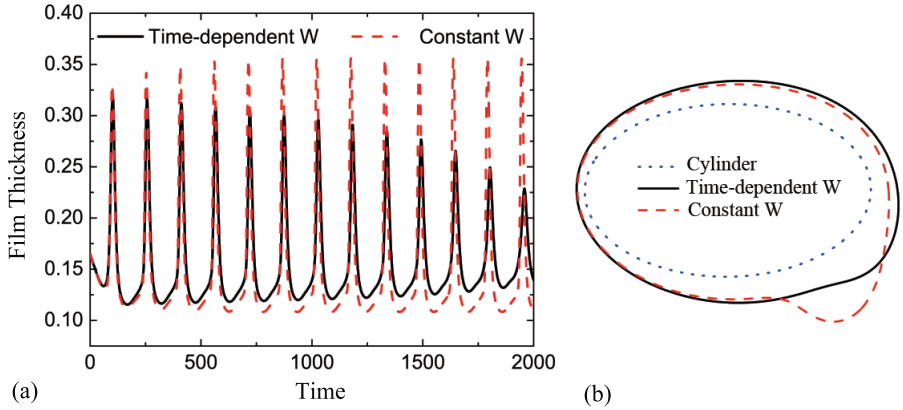

Figure 5.10: (a) Time-variation of film thickness at $\theta = \pi/2$ and (b) free-surface profiles at $t = 2000$ with $\alpha = 0.5$, $Bo = 12.5$, $M = 0.1$, $A_0 = 0.75$, and $W = 0.43$ (red dashed line) and $W = 0.43 - 3.6\cos(2 \times 0.043t)$ (black solid line).

To facilitate comparison with results obtained in the fixed-rotation-rate case when $\alpha = 0.5$ (Fig. 5.3b), we set $W_m = 0.43$ and $A_0 = 0.75$ ($> A_m^{\text{Elliptical}}$). Simulations were performed with different δ and it was found that the liquid bulge will shrink in size when δ is sufficiently large. We pick $\delta = 0.11$ as a representative case, and plot in Figs. 5.10a and 5.10b the time-evolution of film thickness at the $\theta = \pi/2$ point on the cylinder surface and the free-surface profile in the quasi-steady regime, respectively. Results from the constant-rotation case ($\delta = 0$) are shown in these two figures for comparison.

For $\delta = 0$ (red dashed line in Fig. 5.10a), the amplitude of the oscillation in film thickness increases with time until the coating reaches a quasi-steady state in which a liquid bulge hangs from the underside of the cylinder (red dashed line in Fig. 5.10b). For $\delta = 0.11$ (black solid line in Fig. 5.10a), the oscillation in film thickness decays

in amplitude despite the fact that the given load is still larger than the critical value. The corresponding coating (black solid line in Fig. 5.10b) is close to a Moffatt-type smooth coating with a thicker film on the upward-moving side and thinner film on the downward-moving side. Simulations with even larger values of δ are beyond the capability of our simulations because extremely small time-step sizes are required. For this reason, whether there exits an upper limit for δ above which the bulge will grow is unknown.

5.4 Results: Small aspect ratio

To consider the case where the cylinder aspect ratio is small (slender cylinder), we decrease α to a value of 0.2. With this aspect ratio, gradients in both centrifugal forces and substrate curvature become more significant relative to the $O(1)$-aspect-ratio case, and can adversely influence coating smoothness. As in the previous section, we first treat the case of a rapidly spinning cylinder where the effects of gravity can be neglected, and then consider the influence of gravitational forces.

5.4.1 Zero-gravity case

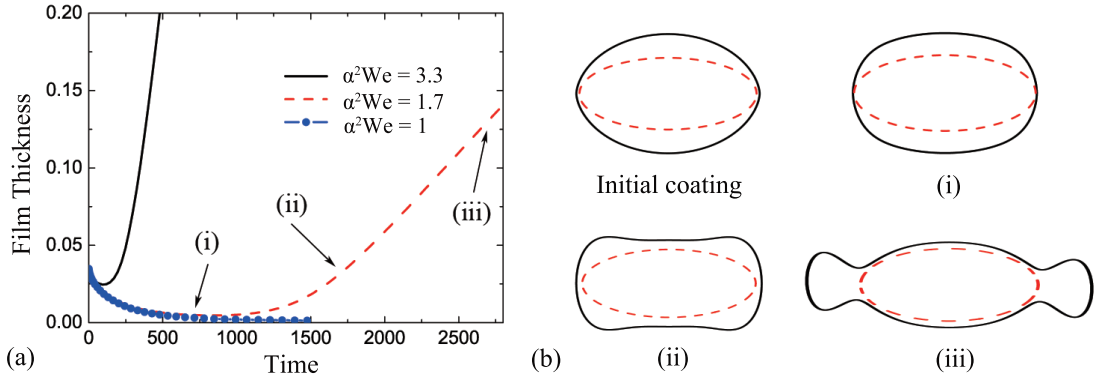

Figure 5.11: (a) Time-variation of film thickness at $\theta = 0$ (cylinder tip) with $A = 0.56$ for three different values of $\alpha^2 We$ ($\alpha = 0.2$). (b) Initial coating and free-surface profiles at three given times (marked in panel (a)) with $\alpha^2 We = 1.7$.

For an elliptical cylinder whose surface is described by Eq. (5.2), the substrate

curvature reaches its maxima at the cylinder tips, $\kappa = \boldsymbol{\nabla} \cdot \mathbf{n} = a/b^2$. An order-of-magnitude estimate of the strength of surface-tension forces is then $F_\sigma = \sigma a/b^2$. Liquid also experiences the strongest centrifugal forces over the cylinder tips, and an order-of-magnitude estimate of the strength of these forces is $F_\Omega = \rho\Omega^2 a^2$. Based on these observations, we characterize the strength of the centrifugal forces relative to surface-tension forces with the parameter $\alpha^2 We = F_\Omega/F_\sigma = \rho\Omega^2 ab^2/\sigma$. For $O(1)$ values of the aspect ratio, $\alpha^2 We \sim We$, which was the parameter used in §5.3.1. But for small aspect ratios, $\alpha^2 We$ provides a better estimate of this force ratio.

For three different values of $\alpha^2 We$, simulations are performed with a moderate initial load, $A_0 = 0.56$, to ensure that film rupture (small A_0) and liquid shedding (large A_0) will not occur too early. The resulting time-evolution of the film thickness at $\theta = 0$ (cylinder tip) is shown in Fig. 5.11a.

For a moderate value of $\alpha^2 We$, the film thickness over the cylinder tip tends to decrease at early times but increase at later times, which we show in Fig. 5.11a with a red dashed line using $\alpha^2 We = 1.7$ as a representative case. To gain deeper insight into the evolution of the coating, we select three times (marked (i)-(iii) in Fig. 5.11a), and plot the corresponding free-surface profiles in Fig. 5.11b.

During relatively early times, surface-tension forces are stronger than centrifugal forces, and drive liquid away from the cylinder tips, which causes the decrease in the film thickness there. The resulting coating (time (i) in Fig. 5.11b) is thicker and almost flat on the top and bottom of the cylinder, but the free surface is still smooth. At later times, centrifugal forces dominate surface-tension forces in the thick-film region (i.e. the top and bottom of the cylinder in Fig. 5.11b), and tend to drive liquid back to the tips. This gives rise to four small liquid bulges located near the tips (time (ii) in Fig. 5.11b). These small bulges are not stable and tend to merge to form two large bulges over the tips (time (iii) in Fig. 5.11b). The resulting highly distorted interface shape significantly increases computational costs, and the simulation must be ended before the bulges would presumably break off.

A decrease in $\alpha^2 We$ to a value of 1 (blue dotted line in Fig. 5.11a) strengthens surface-tension forces, so the film thickness over the tips decreases monotonically until it reaches zero. Film rupture is likely to occur in this case, leaving a bare substrate over the tips. With an increase in $\alpha^2 We$ to a value of 3.3 (black solid line in Fig. 5.11a),

stronger centrifugal forces on the liquid over the tips draw liquid from surrounding areas, which causes the film thickness to increase almost monotonically. As a result, liquid shedding may occur over the tips at a much earlier time relative to the case where $\alpha^2 We = 1.7$. As noted in §5.3.1, similar phenomena are also observed for values of α as large as 0.95.

The results shown in §5.3.1 and §5.4.1 indicate that for a rapidly rotating cylinder, the evolution of a thin-film coating can be highly sensitive to the value of $\alpha^2 We$. High values of $\alpha^2 We$ may lead to film rupture over the tips, while low values of $\alpha^2 We$ may result in liquid shedding. It is possible to obtain a smooth coating on a slender cylinder with moderate $\alpha^2 We$ (time (ii) in Fig. 5.11b), but the liquid film would need to be solidified fast enough before small liquid bulges start to grow near the tips.

5.4.2 Gravity effects

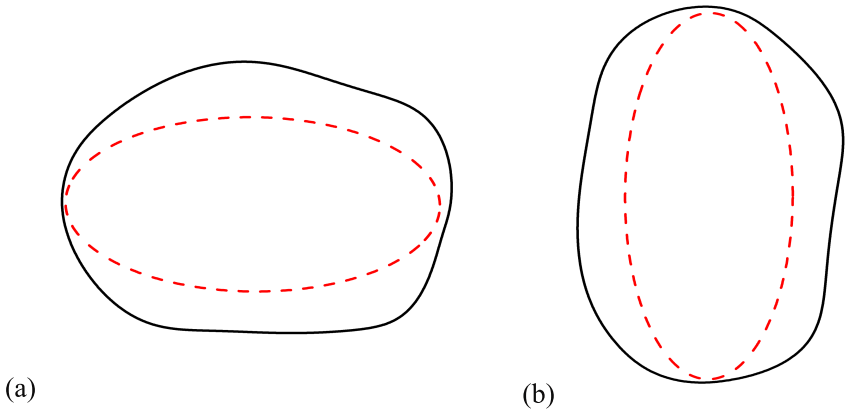

Figure 5.12: (a) Time-variation of film thickness at $\theta = \pi/2$ with $\alpha^2 Bo = 2.5$, $W = 0.43$, $M = 0.1$, and $A_0 = 0.56 < A_m$. Corresponding free-surface profiles at (b) $t = 3323$ and (c) $t = 3531$.

We now include the effects of gravity and consider the constant-rotation-rate case first. An estimate of the importance of gravitational forces, F_g, relative to surface-tension forces, F_σ, is given by $\alpha^2 Bo$, which can be written as

$$\alpha^2 Bo = \frac{F_g}{F_\sigma} = \frac{\rho g a}{\sigma a / b^2} = \frac{\rho g b^2}{\sigma}. \tag{5.16}$$

In our simulations, we set $M = 0.1$, $W = 0.43$, and $A_0 = 0.56 < A_m$, where $A_m = 0.57$ is the maximum load predicted by Hunt [76]. For these parameters, which characterize a rotating small-aspect ratio elliptical cylinder, we were unable to find quasi-steady solutions regardless of the value of $\alpha^2 Bo$. For $\alpha^2 Bo \gg 1$, liquid shedding is likely to occur at the cylinder bottom due to gravity-driven drainage, whereas for $\alpha^2 Bo \ll 1$, film rupture is likely to occur at the cylinder tips due to the strong effects of surface tension.

For $\alpha^2 Bo \sim 1$, where gravitational forces and surface-tension forces are in balance, the shape of the coating varies constantly as cylinder rotates and does not settle down to a Moffatt-type profile, in contrast to the $O(1)$-aspect-ratio case. We show in Fig. 5.12a the time-evolution of the film thickness at the $\theta = \pi/2$ point on the cylinder surface. Free-surface profiles at two relatively late times when the major axis is perpendicular to **g** and parallel to **g** are shown in Fig. 5.12b and Fig. 5.12c. Small liquid bulges form due to the combined effect of gravity (Fig. 5.7a) and surface tension (time (ii) in Fig. 5.11b). These bulges rotate together with the cylinder and do not shrink in size during the time period we studied. Such bulges adversely impact coating smoothness and may be undesired for applications.

In the case where the cylinder rotation rate is time-dependent, high computational costs prevented us from running simulations with a high enough value of δ (variation in the rotation rate, equation (5.15)) to overcome gravity-driven drainage and obtain a smooth coating. To obtain a smooth coating on a small-aspect-ratio cylinder, one possible solution is to use a surfactant-laden liquid. In practice, surfactants are often present in coating liquids to control liquid wettability and surface tension. Since surfactant-induced Marangoni flow tends to weaken both gravity-driven drainage [31] and capillary flows [46], it is reasonable to expect that surfactant-induced Marangoni forces will drive liquid away from the bulges, leading to a smoother coating. For similar reasons, localized heating that drives a Marangoni flow from high- to low-temperature areas may also lead to a smoother coating.

5.5 Conclusions

The results of this work demonstrate that, in general, it is more difficult to obtain a relatively smooth coating on a rotating elliptical cylinder compared to a rotating circular cylinder. Curvature gradients on the cylinder surface lead to gradients in capillary pressure and centrifugal forces that make liquid distribution non-uniform. At relatively high rotation rates where the influence of gravity is negligible, even slight levels of cylinder eccentricity can significantly change the liquid distribution. For slender cylinders, coating evolution is very sensitive to the ratio of centrifugal and surface-tension forces. If this ratio is too small, film rupture will tend to occur at the cylinder tips, whereas if it is too large, liquid shedding will tend to occur there.

When the effects of gravity are significant, we have shown that the maximum load for which a relatively smooth coating can be obtained is smaller for elliptical cylinders (with $O(1)$ aspect ratios) compared to circular cylinders. In both cases, the maximum load decreases as the Stokes number increases with approximately the same power-law dependence. Our results represent an important extension of the work of Hunt [76] to account for the influence of surface tension (and centrifugal forces). While surface tension does not significantly affect the maximum load condition for an elliptical cylinder, it does significantly influence the time required to obtain a relatively smooth coating. Moreover, we also show that by applying a suitably chosen time-dependent rotation rate, more liquid can be supported on the cylinder than the maximum load predicted for constant rotation rates.

For slender cylinders (i.e., those with small aspect ratios) obtaining a relatively smooth coating is considerably more challenging due to the high interfacial curvature near the cylinder tips. Here, it may be beneficial to introduce Marangoni stresses (via surfactants or temperature differences) to obtain a more uniform liquid distribution. Drying or solidifying the coating while simultaneously rotating the cylinder may also be an especially important strategy for obtaining a smooth coating.

Chapter 6

Conclusion and future directions

In this thesis, we have studied liquid-film coating on discrete objects. We have chosen cylinders that rotate about their horizontal axes as model discrete objects and developed both lubrication-theory-based models and 2D models to gain physical insights into fluid dynamics on these cylinders. In this chapter we summarize our key findings and discuss future research directions.

6.1 Summary

We have considered four model problems which are highly relevant to industrial coating processes for rotating discrete objects in chapters $2-5$. In each of these model problems, a systematic analysis of the complex interplay among viscous forces, gravitational forces, centrifugal forces, surface-tension forces, and Marangoni forces has been conducted to reveal the critical condition in which a smooth liquid layer can be maintained on a rotating cylinder.

In Chapters 2 and 3, we investigated surfactant effects on the flow of thin liquid films on rotating cylinders. Lubrication theory has been applied to derive highly coupled nonlinear evolution equations to describe the variation of the film thickness and surfactant concentration as a function of time, the angular coordinate, and the axial coordinate. In Chapter 2, our focus is on characterizing liquid distribution around the circumference of the cylinder, so any axial flows were neglected. In the absence of gravitational effects, using linear stability analysis, we found that Marangoni stresses suppress the growth

rate of instabilities driven by centrifugal forces and hinder the leveling of perturbations to the film thickness. When gravitational effects are present, we pointed out that Marangoni stresses lower the critical rotation rate needed to cause motion of a liquid lobe around the cylinder. These stresses can also lead to faster damping of oscillations in the film thickness at relatively short times, but if strong enough, it can increase the oscillation amplitude at longer times.

We took axial flows into consideration and focused on the stability of thin-film flow in Chapter 3. Inspired by the finding of Evans *et al.* [15] that there appears to be a range of rotation rates (i.e. the stable speed window) in which axial instabilities have no tendencies to grow into defects in the absence of surfactant, we tracked the time evolution of the thin-film flows via our lubrication-theory-based model in the stable speed region and unstable speed region respectively. A comparison between them revealed that capillary forces arising due to an axial gradient in the angular curvature $(h_{\theta\theta})_y$ is responsible for suppressing the onset of both the Rayleigh-Taylor instability triggered by gravitational forces and the Rayleigh-Plateau instability triggered by centrifugal forces in the stable window, and thus causing the liquid film to remain axially uniform. In the case where an insoluble surfactant is present, we found that the stable speed window vanishes. The resulting surfactant-induced Marangoni stresses considerably enhance the growth rate of the RT instability, while suppress the growth rate of the RP instability. Flow visualization experiments have also been performed, results of which are in qualitative agreement with the theoretical predications.

To start to understand the influence of surface topography on coating smoothness, we have taken liquid-film flow on rotating cylinders patterned with sinusoidal and trapezoidal topographical features as a model problem in Chapter 4. The Stokes equations, augmented with a term accounting for centrifugal forces, are solved in a rotating reference frame using GFEM. A nonlinear evolution equation for the film thickness based on lubrication theory is also solved numerically and its predictions are compared to those from the GFEM calculations. When gravitational effects are negligible and the rotation rate is sufficiently low, we show that liquid tends to accumulate over the pattern troughs before merging to form multiple larger drops whose number at steady state depends on the topography wavelength and rotation rate. When the rotation rate is sufficiently high, similar merging events occur, but liquid accumulates over the pattern crests at

steady state. When gravitational forces become significant, we have pointed that it is possible to obtain a coating that closely conforms to the surface topography. The GFEM calculations are in agreement with predictions from the lubrication model provided the free-surface curvatures are sufficiently small. For sufficiently large pattern amplitude and film thickness, the GFEM calculations show that recirculation regions inside the troughs can appear and vanish as the cylinder rotates due to the variation of gravitational forces around the cylinder surface. This phenomenon, along with flow reversal over the crests, may strongly influence mixing, mass transport, and heat transport.

In Chapter 5, we have studied liquid films on rotating ellipitcal cylinders as a model problem to investigate the influence of a non-circular cross section on the maximum load that can be supported on a discrete object. Results of our GFEM simulations show that Hunt's maximum-load condition [76], obtained in the absence of surface tension and centrifugal forces, is not significantly affected by these forces. We have also used the simulations to track the transient behavior of the free surface. For $O(1)$ cylinder aspect ratios, cylinder rotation results in a drop-like liquid bulge hanging on the upward-moving side of the cylinder. This bulge shrinks in size due to surface tension provided that the liquid load is smaller than a critical value, leaving a relatively smooth coating on the cylinder. A decrease in cylinder aspect ratio leads to larger gradients in film thickness, but enhances the rate of bulge shrinkage and thus shortens the time required to obtain a smooth coating. Moreover, with a suitably chosen time-dependent rotation rate, more liquid can be supported by the cylinder relative to the constant-rotation-rate case. For cylinders with even smaller aspect ratios, we pointed out that film rupture and liquid shedding may occur over the cylinder tips, so simultaneous drying and rotation along with the introduction of Marangoni stresses will likely be especially important for obtaining a smooth coating.

6.2 Future Research Directions

In this thesis, we have investigated the influence of surfactants, surface topography, and non-circular cross sections on the flow of liquid film on discrete objects using four model problems. The computational and experimental methods developed in these model problems provide us a framework for studying many other important factors

encountered in industrial coating processes that may influence coating uniformity. The following briefly introduces several future directions for this work.

6.2.1 Evaporation and Rheology

Throughout this work, we have only considered simple Newtonian liquids with constant viscosity and no evaporation from the free surface. In practice, coating flows often include solutions with non-Newtonian characteristics [78] and need to be solidified via drying ("Film Solidification" in Fig. 1.2) while the object to be coated is being rotated for a specific purpose ("Rotating Objects" in Fig. 1.2) [27]. Viscoelasticity may give rise to additional stresses that can greatly alter the local force balance in the flow, and liquid evaporation can trigger a large gradient in bulk surfactant concentration, which as a result, influences the strength of Marangoni stresses. Although both non-Newtonian effects and evaporation effects on thin-film behavior on planar substrates have been extensively studied in the literature [3, 27, 78], little is known about how they influence the liquid-film flow on rotating discrete objects such as cylinders, and for this reason, it would be useful to extend the present work in these two directions.

Both the lubrication-theory-based simplified model and the 2D model used in chapters 2-5 can be augmented in order to study more complex behavior. More specifically, for the non-Newtonian behavior, both models allow for non-Newtonian constitutive equations to be used, and for liquid evaporation, we just need to add several extra terms in the normal stress balance equation to take mass flux normal to the free surface into consideration. Solving the lubrication-theory-based model using the ADI scheme and 2D model using the GFEM scheme would help us build a fundamental understanding on coating of discrete objects with complex coating liquids.

6.2.2 Flow Visualization Experiments

Works that are reported in Chapters 4 (topographically patterned cylinder) and 5 (elliptical cylinder) would benefit from experimental validation. In both chapters, we have pointed out that there exist regions of the problem parameter space where a coating that closely conforms to the cylinder surface can be obtained. Since such types of coatings

are desired for many applications (e.g., coating of stents and contact lenses), experimental validation of critical coating conditions and visualization of the coating shapes around cylinder circumference and also along cylinder axis would greatly improve our understanding on liquid dynamics on rotating three-dimensional objects having complex shapes.

We have already reported in Chapter 3 experimental studies in which a right circular cylinder is used to investigate the onset of coating instabilities in cases where surfactant is absent and present. The experimental apparatus shown in Fig. 3.12 is designed to be flexible, allowing cylinders with more complex surface geometry to be rotated for a wide range of rotation rates. In addition, cylinders required in our experiments can be printed directly via 3D printing, through which we can accurately manipulate the aspect ratio (for elliptical cylinders) and pattern frequency and amplitude (for patterned cylinders).

6.3 Final Note

As the demands on thickness uniformity and coating-process productivity continue to increase in the coating industry, the demand for a solid fundamental understanding of liquid flow over substrates having complex surface geometry will increase with it. In this thesis work, we have developed various computational models and also a new experimental apparatus to fundamentally investigate how important factors, including surfactants, surface topography, and non-circular cross section, influence coating uniformity and stability. We hope that computational and experimental results from our work can serve as a basis for the development of coating maps that identify regions of the problem parameter space where high-quality coatings can be obtained on a given substrate.

References

[1] R. J. Stokes and D. F. Evans, *Fundamentals of Interfacial Engineering*, John Wiley & Sons, 1997.

[2] X. Zhu,, T. Cheng, and C. W Liu. Ga content and thickness inhomogeneity effects on Cu (In, Ga) Se2. *Electronic Materials Letters*, 12: 506-511, 2016.

[3] R. V. Craster and O. K. Matar, Dynamics and stability of thin liquid films. *Rviews of Modern Physics*, 81:1131–1198, 2009.

[4] A. Thomas, Patterned chocolate coatings, methods, and apparatus for preparing same. *U.S. Patent no. 6251455*, 2003.

[5] P. Narayanan, G. H. Llanos, D. Cook, and J. Leidner, Device and process for coating stents, *U.S. Patent no. 6723373*, 2004.

[6] W. L. McKown and P. K. Zietlow, Process for sugar coating ready-to-eat cereal, *U.S. Patent no. 3615676*, 1971.

[7] T. Yamamoto, T. Takeo, K. Ichinose, S. Ozawa, K. Fujii, S. Fujii, M. Enomoto, I. Ishibashi, and J. Murayama, Method for uniformly painting an object with moving spray guns spaced a constant distance from the surface of the object, *U.S. Patent no. 5240745*, 1993.

[8] J. Biteau, C. Ford, and A. Glacet, Method of dip-coating a lens, *U.S. Patent no. 20130022739*, 2013.

[9] H. K. Moffatt. Behaviour of a viscous film on the outer surface of a rotating cylinder. *Journal de Mcanique*, 16:651–673, 1977.

[10] P. L. Evans, L. W. Schwartz, and R. V. Roy. Steady and unsteady solutions for coating flow on a rotating horizontal cylinder: Two-dimensional theoretical and numerical modeling. *Physics of Fluids*, 16:2742–2756, 2004.

[11] V. V. Pukhnachev. Motion of a liquid film on the surface of a rotating cylinder in a gravitational field. *Journal of Applied Mechanics and Technical Physics*, 18:344–351, 1977.

[12] M. A. Kelmanson. Theoretical and experimetal analyses of the maximum-suppotable fluid load on a rotating cylinder. *Journal of engineering mathematics*, 29:271–285, 1995.

[13] L. Preziosi, and D. D. Joseph. The run-off condition for coating and rimming flows. *Journal of fluid mechanics*, 187:99–113, 1988.

[14] R. C. Peterson, P. K. Jimack, and M. A. Kelmanson. On the stability of viscous freesurface flow supported by a rotating cylinder. *Proceedings of the Royal Society of London. Series A: Mathematical, Physical and Engineering Sciences*, 457:1427–1445, 2001.

[15] P. L. Evans, L. W. Schwartz, and R. V. Roy. Three-dimensional solutions for coating flow on a rotating horizontal cylinder: Theory and experiment. *Physics of Fluids*, 17:072102, 2005.

[16] J. R. de Bruyn. Crossover between surface tension and gravity-driven instabilities of a thin fluid layer on a horizontal cylinder. *Physics of Fluids* 9:1599–1605, 1997.

[17] O. H. Campanella and R. L. Cerro Viscous flow on the outside of a horizontal rotating cylinder: The roll coating regime with a single fluid. *Chemical Engineering Science*, 39: 1443-1449,1984.

[18] B. R. Duffy and S. K. Wilson. Thin-film and curtain flows on the outside of a rotating horizontal cylinder. *Journal of Fluid Mechanics*, 394: 29–49 1999.

[19] G. A. Leslie, S. K. Wilson, and B. R. Duffy. Three-dimensional coating and rimming flow: a ring of fluid on a rotating horizontal cylinder. *Journal of Fluid Mechanics*, 716:51–82, 2013.

[20] D. E. Weidner, L. W. Schwartz, and M. H. Eres. Simulation of coating layer evolution and drop formation on horizontal cylinders. *Journal of Colloid and Interface Science* 187: 243–258, 1997.

[21] C. Yih and J. F. C. Kingman. Instability of a rotating liquid film with a free surface. *Proceedings of the Royal Society of London A: Mathematical, Physical and Engineering Sciences*, 258: 63–89, 1960.

[22] J. P. Kovac and R. T. Balmer. Experimental studies of external hygrocysts. *Journal of Fluids Engineering* 102: 226–230, 1980.

[23] W. J. Knox. Photographic surfactant compositions, May 26 1970. US Patent 3,514,293.

[24] S. Kramer and S. Meikle. Reduction of surface roughness during chemical mechanical planarization (cmp), December 5 2002. US Patent App. 10/209,035.

[25] O. K. Matar. and R. V. Craster Models for Marangoni drying. *Physics of Fluids*, 13:1869–1883, 2001.

[26] P. R. Schunk and L. E. Scriven. Surfactant effects in coating processes. In S. F. Kistler and P. M. Schweizer, editors, *Liquid Film Coating*, chapter 14, pp. 495–536. Springer Netherlands, 1997.

[27] A. Oron, S. H. Davis, and S. G. Bankoff. Long-scale evolution of thin liquid films. *Reviews of Modern Physics*, 69:931–980, 1997.

[28] A. K. Sahu and S. Kumar. Thin-liquid-film flow on a topographically patterned rotating cylinder. *Physics of Fluids*, 26:042102, 2014.

[29] O. E. Jensen and J. B. Grotberg. Insoluble surfactant spreading on a thin viscous film: shock evolution and film rupture. *Journal of Fluid Mechanics*, 240: 259–288, 1992.

[30] M. R.E. Warner, R. V. CRASTER, and O. K. Matar. Fingering phenomena associated with insoluble surfactant spreading on thin liquid films. *Journal of Fluid Mechanics*, 510: 169–200, 2004.

[31] D. E. Weidner. Suppression and reversal of drop formation on horizontal cylinders due to surfactant convection. *Physics of Fluids* 25: 082110, 2013.

[32] L. E. Stillwagon and R. G. Larson, Fundamentals of topographic substrate leveling. *Journal of Applied Physics*, 63:5251–5258, 1988.

[33] D. Perizzolo, W. R. Lacefield, and D. M. Brunette. Interaction between topography and coating in the formation of bone nodules in culture for hydroxyapatiteand titaniumcoated micromachined surfaces. *Journal of Biomedical Materials Research*, 56:494-503, 2001.

[34] J. Zhu, J. L. Chen, R. K. Lade Jr., W. J. Suszynski, and L. F. Francis. Water-based coatings for 3D printed parts. *Journal of Coatings Technology and Research*, 12:889–897, 2015.

[35] C. Pozrikidis. The flow of a liquid film along a periodic wall. *Journal of Fluid Mechanics*, 188:275–300, 1988.

[36] A. Wierschem, M. Scholle, and N. Aksel. Vortices in film flow over strongly undulated bottom profiles at low Reynolds numbers. *Physics of Fluids*, 15:426–435, 2003.

[37] M. Scholle, A. Wierschem, and N. Aksel. Creeping films with vortices over strongly undulated bottoms. *Acta Mechanica*, 168:167–193, 2004.

[38] M. Scholle, A. Haas, N. Aksel, M. C. T. Wilson, H. M. Thompson, and P. H. Gaskell. Competing geometric and inertial effects on local flow structure in thick gravity-driven fluid films. *Physics of Fluids*, 20:123101, 2008.

[39] A. Wierschem and N. Aksel. Influence of inertia on eddies created in films creeping over strongly undulated substrates. *Physics of Fluids*, 16:4566–4574, 2004.

[40] M. Scholle, A. Haas, N. Aksel, H. M. Thompson, R. W. Hewson, and P. H. Gaskell. The effect of locally induced flow structure on global heat transfer for plane laminar shear flow. *International Journal of Heat and Mass Transfer*, 30:175–185, 2009.

[41] J. Nam, L. E. Scriven, and M. S. Carvalho. Tracking birth of vortex in flows. *Journal of Computational Physics*, 228:4549–4567, 2009.

[42] A. K. Sahu and S. Kumar. Thin-liquid-film flow on a topographically patterned rotating cylinder. *Physics of Fluids*, 26:042102, 2014.

[43] B. G. Zhang, D. E. Myers, G. G. Wallace, M. Brandt, and P. F. Choong, Bioactive coatings for orthopaedic implants-recent trends in development of implant coatings. *International Journal of Molecular Science*, 15:11878-11921, 2014.

[44] Y. Maeda, S. Miyoshi, and T. Yamaguchi, Oval cross section metal tube producing device and producing method, February 5, 2007. U.S. Patent No.7,219,522.

[45] A. Thomas, Patterned chocolate coatings, methods, and apparatus for preparing same, June 26, 2001. U.S. Patent No. 6251455

[46] W. Li and S. Kumar. Thin-film coating of surfactant-laden liquids on rotating cylinders. *Physics of Fluids*, 27:072106, 2015.

[47] P. Narayanan, G. H. Llanos, D. Cook, and J. Leidner. Device and process for coating stents, April 20 2004. US Patent 6,723,373.

[48] A. Thomas. Patterned chocolate coatings, methods, and apparatus for preparing same, June 26 2001. US Patent 6,251,455.

[49] O. E. Jensen and J. B. Grotberg. The spreading of heat or soluble surfactant along a thin liquid film. *Physics of Fluids A: Fluid Dynamics*, 5:58, 1993.

[50] D. M. Campana and F. A. Saita. Numerical analysis of the Rayleigh instability in capillary tubes: The influence of surfactant solubility. *Physics of Fluids*, 18:22104, 1996.

[51] N. J. Alvarez, L. M. Walker, and S. L. Anna Diffusion-limited adsorption to a spherical geometry: The impact of curvature and competitive time scales. *Physical Review E*, 82:011604,2010

[52] B. Tsai, M. S. Carvalho, and S. Kumar. Leveling of thin films of colloidal suspensions. *Journal of Colloid and Interface Science*, 343:306–313, 2010.

[53] P. L. Evans. *Mathematical and numerical investigations of coating flows.* PhD thesis, University of Delaware, 2000.

[54] L. W. Schwartz, D. E. Weidner, and R. R. Eley. An analysis of the effect of surfactant on the leveling behavior of a thin liquid coating layer. *Langmuir*, 11:3690–3693, 1995.

[55] L. W. Schwartz, R. A. Cairncross, and D. E. Weidner. Anomalous behavior during leveling of thin coating layers with surfactant. *Physics of Fluids*, 8:1693–1695, 1996.

[56] E. J. Hinch, and M. A. Kelmanson. On the decay and drift of free-surface perturbations in viscous thin-film flow exterior to a rotating cylinder. *Proceedings of the Royal Society of London. Series A: Mathematical, Physical and Engineering Sciences*, 459: 1193–1213, 2003.

[57] D. Garg and P. N. Dyer. Tungsten carbide erosion resistant coating for aerospace components. *MRS Online Proceedings Library Archive*, 168, 1989.

[58] P. Narayanan, G. H. Llanos, D. Cook, and J. Leidner Device and process for coating stents, April 20 2004. US Patent 6,723,373

[59] A. Marmur and M. D. Lelah The spreading of aqueous surfactant solutions on glass *Chemical Engineering Communications*, 13: 133-143, 1981.

[60] M. R. E. Warner, R. V. Craster, and O. K. Matar Unstable van der Waals driven line rupture in Marangoni driven thin viscous films. *Physics of Fluids*, 14:1641–1654, 2002.

[61] T. M. Witelski and M. Bowen. ADI schemes for higher-order nonlinear diffusion equations. *Applied Numerical Mathematics*, 45: 331–351, 2003.

[62] M. R. Mata, and A. L. Bertozzi. A numerical scheme for particle-laden thin film flow in two dimensions. *Journal of Computational Physics*, 230: 6334–6353, 2011.

[63] W. Li and S. Kumar Liquid-film coating on topographically patterned rotating cylinders. *Physical Review Fluids*, 2: 024001, 2017.

[64] W. Li, M. S. Carvalho, and S. Kumar Viscous free-surface flows on rotating elliptical cylinders. *Physical Review Fluids*, 2: 094005, 2017.

[65] S. K. Wilson, R. Hunt, and B. R. Duffy. On the critical solutions in coating and rimming flow on a uniformly rotating horizontal cylinder. *The Quarterly Journal of Mechanics and Applied Mathematics*, 55 357–383, 2002.

[66] G. K. Batchelor. *An introduction to fluid dynamics.* (Cambridge University Press, Cambridge, UK. 1967)

[67] M. A. Kelmanson. On inertial effects in the MoffattPukhnachov coating-flow problem. *Journal of Fluid Mechanics*, 633:327–353, 2009.

[68] S. Dodds, M. da Silveira Carvalho, and S. Kumar. Stretching and slipping of liquid bridges near plates and cavities. *Physics of Fluids*, 21:092103, 2009.

[69] W. L. Mckown and P. K. Zietlow. Process for sugar coating ready-to-eat cereal, October 26 1971. US Patent 3615676.

[70] E. B. Hansen and M. A. Kelmanson. Steady, viscous, free-surface flow on a rotating cylinder. *Journal of Fluid Mechanics*, 272:91–108, 1994.

[71] C. Pozrikidis. Creeping flow in two-dimensional channels. *Journal of Fluid Mechanics*, 180:495-514,1987.

[72] S. Kalliadasis, C. Bielarz, and G. M. Homsy. Steady free-surface thin film flows over topography. *Physics of Fluids*, 12:1889–1898, 2000.

[73] S. Kalliadasis and G. M. Homsy. Stability of free-surface thin-film flows over topography. *Journal of Fluid Mechanics*, 448:387–410, 2001.

[74] J. R. Lister, J. M. Rallison, A. A. King, L. J. Cummings, and O. E. Jensen. Capillary drainage of an annular film: the dynamics of collars and lobes. *Journal of Fluid Mechanics*, 552:311-343, 2006.

[75] C. Pozrikidis. Effect of surfactants on film flow down a periodic wall. *Journal of Fluid Mechanics*, 496:105–127, 2003.

[76] R. Hunt, Numerical solution of the free-surface viscous flow on a horizontal rotating elliptical cylinder. *Numerical Methods for Partial Differential Equations*, 24:1094–1114, 2008.

[77] R. V. Roy, A. J. Roberts, and M. E. Simpson, A lubrication model of coating flows over a curved substrate in space. *Journal of Fluid Mechanics*, 454:235–261, 2002.

[78] J. E. Glass and R. K. Prudhomme. Coating rheology: component influence on the rheological response and performance of water-borne coatings in roll applications. In S. F. Kistler and P. M. Schweizer, editors, *Liquid Film Coating*, chapter 5, pp. 137–182. Springer Netherlands, 1997.

[79] M. R. E. Warner, R. V. Craster, and O. K. Matar, Surface patterning via evaporation of ultrathin films containing nanoparticles. *Journal of Colloid and Interface Science* 267:92–110, 2003.

[80] P. H. Gaskell, P. K. Jimack, M. Sellier, and H. M. Thompson, Flow of evaporating, gravity-driven thin liquid films over topography. *Physics of Fluids*, 18:013601, 2006.

[81] J. Reddy. An Introduction to the Finite Element Method. McGraw-Hill, 2005.

[82] K. N. Christodoulou and L. E. Scriven. Discretization of free surface flows and other moving boundary problems. *Journal of Computational Physics*, 99: 39-55, 1992.

[83] N. Chatzidai, A. Giannousakis, T. Dimakopoulos, and J. Tsamopoulos On the elliptic mesh generation in domains containing multiple inclusions and undergoing large deformations. *Journal of Computational Physics*, 228:1980–2011, 2009.

[84] P. M. Gresho, R. L. Lee, and R. L. Sani. On the time-dependent solution of the incompressible Navier-Stokes equations in two and three dimensions. In: Taylor, C., Morgan, K. (Eds.), Recent Advances in Numerical Methods in Fluids. Pineridge Press, Swansea, UK, pp. 27-79.

[85] M. Luskin, R. Rannacher, and W. Wendland. On the smoothing property of the Crank-Nicolson scheme. *Applicable Analysis*, 14:117–135, 1982.

Appendix A

Derivation of 3D evolution equations

We summarize here the derivation of the evolution equations (3.12) and (3.13). After introducing the scalings (3.11), governing equations (3.4) and (3.5) become (tildes dropped)

$$\frac{\partial}{\partial z}(rw) + \frac{\partial u}{\partial \theta} + r\frac{\partial v}{\partial y} = 0, \tag{A.1}$$

$$-W^2(1+\epsilon z) = -\frac{\partial p}{\partial z} + \epsilon\frac{\partial^2 w}{\partial^2 z} - \sin\theta, \tag{A.2}$$

$$0 = -\epsilon\frac{\partial p}{\partial \theta} + \frac{\partial^2 u}{\partial^2 z} + \epsilon\frac{\partial u}{\partial z} - \cos\theta, \tag{A.3}$$

$$0 = -\epsilon\frac{\partial p}{\partial y} + \left(\frac{\partial^2}{\partial z^2} + \epsilon\frac{\partial}{\partial z}\right)v, \tag{A.4}$$

where $W = \Omega/\sqrt{g/R}$ is the dimensionless rotation rate. Note that terms of $O(\epsilon^2)$ are neglected in above equations and those below. As a consequence, the Reynolds numbers $Re = \rho^2 g H^2 R/\mu^2$ and $Re_\Omega = \rho\Omega R^2/\mu$ can be no larger than $O(1)$ [10, 15].

The simplified tangential stress boundary conditions in θ- and y-directions are

$$\frac{\partial u}{\partial z} - \epsilon u = \epsilon Ma\frac{\partial \sigma}{\partial \theta}, \tag{A.5}$$

$$\frac{\partial v}{\partial z} = \epsilon Ma\frac{\partial \sigma}{\partial y}, \tag{A.6}$$

where the Marangoni number $Ma = \varphi/\mu U$ measures the strength of surface-tension-gradient forces relative to viscous forces. For dilute concentrations of surfactant such that $\varphi/\sigma_m \sim \epsilon$, the normal stress boundary condition (3.7) becomes

$$-p + 2\epsilon(\mathbf{n}\cdot\boldsymbol{\tau}\cdot\mathbf{n}) = -\frac{1}{\epsilon Bo}\kappa + \epsilon Ma\sigma. \tag{A.7}$$

The Bond number, $Bo = \rho g R^2/\sigma_m$, measures the importance of surface-tension forces relative to gravitational forces. The outward unit normal $\mathbf{n}$, surface curvature κ, and rate-of-strain tensor $\boldsymbol{\tau}$ (nondimensionlized by U/R) are given by

$$\mathbf{n} = \mathbf{e}_r - \mathbf{e}_\theta \frac{\epsilon}{r}\frac{\partial h}{\partial \theta} - \mathbf{e}_y \frac{\partial h}{\partial y}, \tag{A.8}$$

$$\kappa = 1 - \epsilon h - \epsilon \overline{\nabla}^2 h, \tag{A.9}$$

$$\tau_{rr} = \frac{\partial w}{\partial z}, \tag{A.10}$$

$$\tau_{\theta\theta} = \frac{1}{r}\frac{\partial u}{\partial \theta} + \epsilon\frac{w}{r}, \tag{A.11}$$

$$\tau_{yy} = \frac{\partial v}{\partial y} \tag{A.12}$$

$$2\tau_{r\theta} = 2\tau_{\theta r} = \frac{1}{\epsilon}\frac{\partial u}{\partial z} - \frac{u}{r} + \frac{\epsilon}{r}\frac{\partial w}{\partial \theta}, \tag{A.13}$$

$$2\tau_{\theta y} = 2\tau_{y\theta} = \frac{1}{r}\frac{\partial v}{\partial \theta} + \frac{\partial u}{\partial y} \tag{A.14}$$

$$2\tau_{yr} = 2\tau_{ry} = \frac{1}{\epsilon}\frac{\partial v}{\partial z} + \epsilon\frac{\partial w}{\partial y}, \tag{A.15}$$

where $\overline{\nabla}^2 = \partial^2/\partial\theta^2 + \partial^2/\partial y^2$.

At the free surface, the kinematic condition (3.9) takes the form

$$\frac{\partial h}{\partial t} + \frac{r\Omega + u}{r}\frac{\partial h}{\partial \theta} + v\frac{\partial h}{\partial y} - w = 0. \tag{A.16}$$

At the cylinder surface, the dimensionless no-slip and no-penetration boundary conditions are

$$u = w = v = 0, \tag{A.17}$$

where u, v, and w are velocity components defined in Eq. (3.2).

Following Refs [10, 15, 46], we apply a perturbation expansion in the small parameter $\epsilon = H/R \ll 1$ to solve Eqs. (A.1)-(A.4) subject to boundary conditions (A.5)-(A.7) and

(A.16)-(A.17). The variables are expanded in powers of ϵ as

$$\begin{aligned} u &= u^{(0)} + \epsilon u^{(1)} + ..., \\ w &= w^{(0)} + \epsilon w^{(1)} + ..., \\ v &= v^{(0)} + \epsilon v^{(1)} + ..., \\ p &= \epsilon^{-1} p_0 + p^{(0)} + \epsilon p^{(1)} + ..., \end{aligned} \tag{A.18}$$

where the additional pressure $p_0 = Bo^{-1}$ arises due to the film being forced to take the shape of the cylinder with curvature $1/R$ [10].

We substitute above expansions into Eqs. (A.1)-(A.4) and solve for the leading-order pressure and velocity components:

$$p^{(0)} = -\frac{1}{Bo}(h + \overline{\nabla}^2 h) + (W^2 - \sin\theta)(z - h), \tag{A.19}$$

$$u^{(0)} = \cos\theta \left(\frac{1}{2}z^2 - hz\right), \tag{A.20}$$

$$w^{(0)} = \sin\theta \left(\frac{1}{6}z^3 - \frac{1}{2}hz^2\right) + \frac{1}{2}\cos\theta \frac{\partial h}{\partial \theta} z^2, \tag{A.21}$$

$$v^{(0)} = 0. \tag{A.22}$$

Note that gravity has no influence on the axial component of the velocity at leading order ($v^{(0)} = 0$), but gives rise to a parabolic profile in the angular direction due to gravity-driven drainage.

At the next order, it turns out that we only need $u^{(1)}$ and $v^{(1)}$, which are given by

$$\begin{aligned} u^{(1)} = &- \cos\theta \left(\frac{1}{3}z^3 - hz^2 + \frac{3}{2}h^2 z\right) - \left[\frac{1}{Bo}\frac{\partial}{\partial\theta}\left(h + \overline{\nabla}^2 h\right)\right. \\ &\left. + (W^2 - \sin\theta)\frac{\partial h}{\partial\theta}\right]\left(\frac{1}{2}z^2 - hz^2\right) - Maz\frac{\partial \Gamma}{\partial\theta}. \end{aligned} \tag{A.23}$$

$$v^{(1)} = -\left[\frac{1}{Bo}\frac{\partial}{\partial y}\left(h + \overline{\nabla}^2 h\right) + (W^2 - \sin\theta)\frac{\partial h}{\partial y}\right]\left(\frac{1}{2}z^2 - hz^2\right) - Maz\frac{\partial \Gamma}{\partial y}. \tag{A.24}$$

The Marangoni terms become significant in regions where the concentration gradients are large (large $\partial\Gamma/\partial\theta$ or $\partial\Gamma/\partial y$), and the resulting forces drive flow from areas of high concentration to low concentration.

After integrating the continuity equation (A.1) from $z = 0$ to $z = h$ and then substituting the result into Eq. (A.16), we obtain the evolution equation for the film thickness,

$$\begin{aligned}(1+\epsilon h)\frac{\partial h}{\partial t} =& -\left(\frac{MW}{\epsilon^2}\right)\frac{\partial}{\partial\theta}\left(h+\epsilon\frac{h^2}{2}\right)+\frac{\partial}{\partial\theta}\left[\left(\frac{h^3}{3}+\epsilon\frac{h^4}{2}\right)\cos\theta\right]\\ &-\epsilon\overline{\boldsymbol{\nabla}}\cdot\left[\frac{h^3}{3Bo}\overline{\boldsymbol{\nabla}}(h+\overline{\nabla}^2 h)+\frac{h^3}{3}(W^2-\sin\theta)\overline{\boldsymbol{\nabla}}h-\frac{1}{2}Mah^2\overline{\boldsymbol{\nabla}}\Gamma\right],\end{aligned} \tag{A.25}$$

where $\overline{\boldsymbol{\nabla}} = \mathbf{e}_\theta\frac{\partial}{\partial\theta}+\mathbf{e}_y\frac{\partial}{\partial y}$. The first term on the right-hand side arises due to the solid-body rotation, in which $M = \mu/\rho\sqrt{gR^3}$ is a dimensionless viscosity and MW/ϵ^2 gives the ratio of the cylinder surface speed to the characteristic velocity. This constant is assumed to be $O(1)$ or smaller to ensure that surface tension plays an important role in supporting excess liquid near the underside of the cylinder. For further details of the derivation, we refer the reader to Refs. [10] and [15].

Following the scaling and expansion procedure described above, the surfactant transport equation (3.10) becomes

$$r\frac{\partial\Gamma}{\partial t}+\frac{\partial}{\partial\theta}\left(r\frac{MW}{\epsilon^2}\Gamma+u_s\Gamma\right)+\frac{\partial}{\partial y}\left[\Gamma v_s\right]+\epsilon\frac{\partial h}{\partial t}\Gamma=\frac{1}{Pe}\frac{\partial}{\partial\theta}\left(\frac{1}{r}\frac{\partial\Gamma}{\partial\theta}\right)+\frac{1}{Pe}\frac{\partial}{\partial y}\left(r\frac{\partial\Gamma}{\partial y}\right), \tag{A.26}$$

where the Pélet number, $Pe = UR/D$, measures the strength of surfactant convection relative to diffusion. The surface velocity, $(u_s, v_s) = (u, v)|_{z=h}$, is given by

$$\begin{aligned}u_s =& -\frac{1}{2}h^2\cos\theta-\epsilon\frac{5}{6}h^3\cos\theta-\epsilon Mah\frac{\partial\Gamma}{\partial\theta}\\ &+\epsilon\frac{1}{2}\left\{\frac{h^2}{Bo}\frac{\partial}{\partial\theta}\left(h+\overline{\nabla}^2 h\right)+h^2(W^2-\sin\theta)\frac{\partial h}{\partial\theta}\right\}.\\ v_s =& \epsilon\frac{1}{2}\left\{\frac{h^2}{Bo}\frac{\partial}{\partial y}\left(h+\overline{\nabla}^2 h\right)+h^2(W^2-\sin\theta)\frac{\partial h}{\partial y}\right\}-\epsilon Mah\frac{\partial\Gamma}{\partial y}.\end{aligned} \tag{A.27}$$

Further details of the derivation can be found in Ref. [31].

Appendix B

Effects of insoluble surfactants on the Rayleigh-Plateau instability and the Rayleigh-Taylor instability

In this appendix, we provide some details of the linear stability analyses that were carried out to investigate the influence of insoluble surfactant on the Rayleigh-Plateau (RP) instability and the Rayleigh-Taylor (RT) instability.

B.1 Rayleigh-Plateau instability

In the case where the cylinder is spinning so rapidly that gravitational forces are negligible, Eqs. (3.16) and (3.17) in §3.3 are the two coupled evolution equations that describe the variation of the film thickness and surfactant concentration. To gain insight into the growth of the axisymmetric RP instability, we neglect angular variations in film thickness and set $\partial h/\partial\theta = \partial^3 h/\theta^3\theta = 0$. With this assumption, Eqs. (3.16) and (3.17)

become

$$(1+h)\frac{\partial h}{\partial t} = -\frac{1}{3}\frac{\partial}{\partial y}\left\{h^3\frac{\partial}{\partial y}\left(h+\frac{\partial^2 h}{\partial^2 y}\right)+h^3 S\frac{\partial h}{\partial y}\right\}+\frac{1}{2}Ma\frac{\partial}{\partial y}\left(h^2\frac{\partial h}{\partial y}\right), \tag{B.1}$$

$$r\frac{\partial \Gamma}{\partial t}+\frac{\partial}{\partial y}\left[\Gamma v_s\right] = \frac{1}{Pe}\frac{\partial}{\partial y}\left(r\frac{\partial \Gamma}{\partial y}\right), \tag{B.2}$$

where the surface velocity in the axial direction, v_s, is given by

$$v_s = \frac{1}{2}\left\{h^2\frac{\partial}{\partial y}\left(h+\frac{\partial^2 h}{\partial y}\right)+Sh^2\frac{\partial h}{\partial y}\right\}-Mah\frac{\partial \Gamma}{\partial y}. \tag{B.3}$$

In the case where surfactant has no influence on film evolution ($Ma = 0$), Eq. (B.1) reduces to that obtained by Evans *et al.* [15] for a surfactant-free axisymmetric film.

A standard normal mode decomposition is used for h and Γ,

$$\begin{aligned} h(x,y,t) &= H_b + H_0\exp(ik_y y + st),\\ \Gamma(x,y,t) &= \Gamma_b + \Gamma_0\exp(ik_y y + st), \end{aligned} \tag{B.4}$$

Substitution of the above equations into Eqs. (B.1) and (B.2) leads to an eigenvalue problem of the form

$$\mathbf{A}\begin{pmatrix} H_0 \\ \Gamma_0 \end{pmatrix} = s\begin{pmatrix} H_0 \\ \Gamma_0 \end{pmatrix}, \tag{B.5}$$

where

$$\mathbf{A} = \begin{pmatrix} \frac{H_b^3}{3r_b}k_y^2[(1+S)-k_y^2] & -\frac{1}{2r_b}Mak_y^2H_b^2 \\ \frac{1}{2r_b}H_b^2\Gamma_b k_y^2[(1+S)-k_y^2] & -\frac{1}{r_b}\left(MaH_b\Gamma_b k_y^2+\frac{1}{Pe_s}r_b k_y^2\right) \end{pmatrix}. \tag{B.6}$$

It is found that both roots are purely real, and only one of the roots becomes positive; it is this root shown in the results below.

As an example, we consider the case where $S = W^2Bo = 0.09$, $H_b = 0.03162$, $\Gamma_b = 1$, and $Pe = 10^5$. We solve matrix equation (B.5) for three different values of Ma to yield growth rates of the RP instability, s_{RP}, as a function of wavenumber k_y. Results are shown in Fig. B.1a.

Fig. B.1a shows that the growth rate of the RP instability is positive over a range of wavenumbers (unstable region) and negative beyond the cutoff wavenumber (stable region). With an increase in the value of Ma, which corresponds to stronger Marangoni stresses, the value of s_{RP} decreases in the unstable region but increases in the stable region. This indicates that Marangoni stresses tend to suppress the growth rate of the

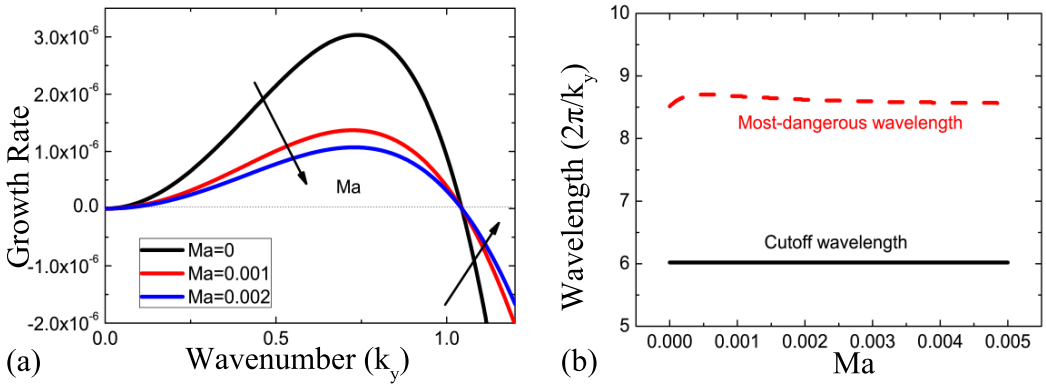

Figure B.1: (a) Growth rates of the RP instability versus wavenumber for three different values of Ma with $S = 0.09$, $H_b = 0.03162$, $\Gamma_b = 1$, and $Pe = 10^5$. The arrows indicate the direction of increasing Marangoni number. (b) Corresponding most-dangerous wavelength (red dashed line) and cutoff wavelength (black solid line) of the RP instability versus Marangoni number.

RT instability, but hinder the leveling of perturbations to the film thickness. Similar behavior is also observed in the case where axial variations are neglected and perturbations can only grow in the angular direction [46]. The physical mechanisms responsible for the behavior observed in Fig. B.1a are the same as those at play when purely angular perturbations are present [46].

We now investigate the evolution of the most-dangerous wavelength, $\lambda^{\star}_{\text{ring}} = 2\pi/k_y^{\max}$, for which the perturbation has the largest growth rate, and the cutoff wavelength, $\lambda_{\text{ring}} = 2\pi/k_y^{\text{cutoff}}$, for which the perturbation has a growth rate of zero. Here, $k_y^{\max}$ and k_y^{cutoff} are the corresponding most-dangerous wavenumber and cutoff wavenumber defined in §3.3. Results are shown in Fig. B.1b for $0 \leq Ma \leq 0.3$. In the surfactant-free case, the cutoff wavelength and the most-dangerous wavelength are $\lambda_{\text{ring}} = 2\pi/\sqrt{1+S} = 6.02$ and $\lambda^{\star}_{\text{ring}} = 2\sqrt{2}\pi/\sqrt{1+S} = 8.51$, respectively. Marangoni stresses have no influence on the cutoff wavelength (black solid line in Fig. B.1b), and this is because at the cutoff wavelength, centrifugal forces are balanced by capillary forces and no Marangoni flows are present [46]. Marangoni stresses give rise to a slight increase (about 2%) in the value of the most-dangerous wavelength (red dashed line in Fig. B.1b) in a small region near $Ma = 0$. However, with an increase in Ma (i.e.,

stronger Marangoni stresses), the value of $\lambda^{\star}_{\text{ring}}$ drops back to its value in the surfactant-free case. Similar behavior is observed for other parameter values.

B.2 Rayleigh-Taylor instability

In the case where the cylinder is stationary, the film on the cylinder tends to sag under the action of gravity, forming a ridge of liquid aligned with the cylinder axis at the cylinder bottom [20]. This ridge is unstable to gravity-induced axial perturbations, which is analogous to the Rayleigh-Taylor instability of a liquid layer underneath a horizontal flat plate.

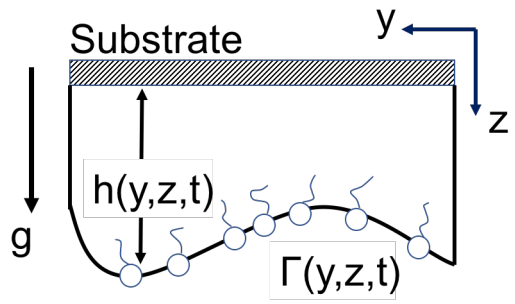

Figure B.2: Schematic of problem geometry

To gain insight into the effects of surfactant on the RT instability, we consider a two-dimensional thin film of a Newtonian liquid laden with an insoluble surfactant underneath a horizontal plate (Fig. B.2). Applying the lubrication approximation yields the following dimensional evolution equations for the film thickness and surfactant surface concentration, respectively [15, 54]:

$$\frac{\partial h}{\partial t} = -\frac{\partial}{\partial y}\left\{\frac{h^3}{3\mu}\left[\frac{\partial}{\partial y}\left(\sigma\frac{\partial^2 h}{\partial y^2}\right) + \rho g\frac{\partial h}{\partial y}\right] - \varphi\frac{h^2}{2\mu}\frac{\partial \Gamma}{\partial y}\right\}, \tag{B.7}$$

$$\Gamma_t + (u_s\Gamma)_y = D\Gamma_{yy}, \tag{B.8}$$

where φ is the spreading pressure defined in §3.2.2 and u_s is the surface velocity at $z = h(y,z,t)$,

$$u_s = \frac{h^2}{2\mu}\frac{\partial}{\partial y}\left\{\sigma\frac{\partial^2 h}{\partial y^2} + \rho g h\right\} - \varphi\frac{h}{\mu}\frac{\partial \Gamma}{\partial y}. \tag{B.9}$$

To be consistent with Eqs. (B.1) and (B.2), we scale all lengths by R which can also be considered as the characteristic length scale along the film (y-direction). The resulting dimensionless evolution equations are

$$\frac{\partial h}{\partial t} = -\frac{\partial}{\partial y}\left\{\frac{h^3}{3}\left[Bo^{-1}\frac{\partial}{\partial y}\left(\frac{\partial^2 h}{\partial y^2}\right)+\frac{\partial h}{\partial y}\right]-Ma\frac{h^2}{2}\frac{\partial \Gamma}{\partial y}\right\}, \tag{B.10}$$

$$\Gamma_t + (u_s\Gamma)_y = Pe^{-1}\Gamma_{yy}, \tag{B.11}$$

where dimensionless constants Bo, Ma, and Pe are defined in Table 3.2.

After using a standard normal mode decomposition for h and Γ, we obtain a new matrix equation

$$\mathbf{A}\begin{pmatrix} H_0 \\ \Gamma_0 \end{pmatrix} = s\begin{pmatrix} H_0 \\ \Gamma_0 \end{pmatrix}, \tag{B.12}$$

where

$$\mathbf{A} = \begin{pmatrix} \frac{1}{3}H_b^3[\frac{k^2}{Bo}-k^4] & -\frac{1}{2}MaH_b^2k^2 \\ \frac{1}{2}H_b^2\Gamma_b[\frac{k^2}{Bo}-k^4] & -(Ma\Gamma_b+\frac{1}{Pe})k^2 \end{pmatrix}. \tag{B.13}$$

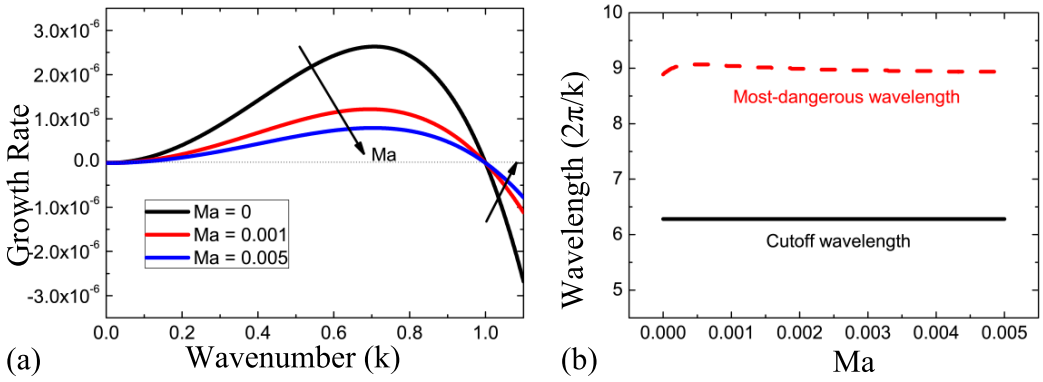

Figure B.3: (a) Growth rates of the RT instability versus wavenumber for three different values of Ma with $Bo = 1$, $H_b = 0.03162$, $\Gamma_b = 1$, and $Pe = 10^5$. The arrows indicate the direction of increasing Marangoni number. (b) Corresponding most-dangerous wavelength (red dashed line) and cutoff wavelength (black solid line) of the RT instability versus Marangoni number

As before, both roots are purely real, and only one of the roots becomes positive; it is this root shown in the results below.

As an example, we consider the case where $Bo = 0.01$, $H_b = 0.03162$, $\Gamma_b = 1$, and $Pe = 10^5$. We solve for growth rates of the RT instability, s_{RT}, as a function of wavenumber k. Results are shown in Fig. B.3a for three different values of Ma. The most-dangerous wavelength, $\lambda^{\star}_{\text{drop}}$, and the cutoff wavelength, λ_{drop}, as functions of Ma are shown in Fig. B.3b. We briefly summarize our findings.

Marangoni stresses tend to suppress the growth rate of the RT instability (Fig. B.3a), similar to the RP-instability (Fig. B.1a). With the presence of surfactant, the cutoff wavelength remains constant, $\lambda_{\text{drop}} = 2\pi/\sqrt{Bo} = 6.28$ (black solid line in Fig. B.3b), while the value of the most-dangerous wavelength, $\lambda^{\star}_{\text{drop}}$, increases slightly (by about 2%) in a small region near $Ma = 0$ and drops back to its value in the surfactant-free case ($\lambda^{\star}_{\text{drop}} = 2\sqrt{2}\pi/\sqrt{Bo} = 8.89$) with an increase in Ma (red dashed line in Fig. B.3b). Similar behavior is observed for other parameter values.

Appendix C

Finite element method

This appendix illustrates the Galerkin finite-element method (GFEM) used in §4 and §5 to solve the full 2D time-dependent flow problems in a rotating frame of reference.

C.1 Governing equations

In §2 and §3, lubrication theory is used to simplify the governing equations; however, it is limited in accuracy due to geometrical constraints on the thickness of liquid films, pattern amplitude, etc. To overcome these restrictions, we used the finite element method in §4 and §5 to numerically solve the 2D governing equations on topographically patterned cylinders and elliptical cylinders, respectively. The sample finite-element meshes at $t = 0$ are shown in Figs. 4.1 and 5.1.

The dimensionless governing equations for both geometries are given by

$$\mathbf{0} = -\boldsymbol{\nabla} p + \nabla^2 \mathbf{u} - W^2 \mathbf{r} + \mathbf{e}_g, \tag{C.1}$$

where $W = \Omega/\sqrt{g/a}$ is the dimensionless rotation rate.

At the cylinder surface, $\mathbf{R}(x_0, y_0)$, no-slip and no-penetration boundary conditions are applied

$$\mathbf{t} \cdot \mathbf{u} = 0, \quad \mathbf{n} \cdot \mathbf{u} = 0, \tag{C.2}$$

where $\mathbf{n}$ and $\mathbf{t}$ are the unit outward normal and tangent vectors.

At the free surface, $\mathbf{r}_s(x, y)$, we have the kinematic and interfacial-stress boundary conditions,

$$\mathbf{n} \cdot \mathbf{u} = \mathbf{n} \cdot \dot{\mathbf{r}_s}, \tag{C.3}$$

$$\mathbf{n} \cdot \mathbf{T} = -\frac{\kappa}{Bo}\mathbf{n}, \tag{C.4}$$

where $\mathbf{T}$ is the total stress tensor, $\kappa = \boldsymbol{\nabla} \cdot \mathbf{n}$ is the surface curvature, $\dot{\mathbf{r}_s}$ is the free-surface velocity, and $Bo = \rho g a^2/\sigma$, is Bond number.

In a typical finite element method, the solution of the governing equations is approximated by a finite set of basis functions multiplied by unknown nodal coefficients. The unknowns of interest are velocity, pressure, and mesh displacement in this thesis. Residual equations are first obtained by substituting a series of trial functions into the governing differential equations in place of the continuous solution. These residual equations are then multiplied by weight functions and integrated over the domain to obtain a set of non-linear algebraic equations for the nodal unknowns. These unknowns are found such that the weighted residual equations are approximately zero. More details on this method can be found in Ref. [81].

Since the model problems discussed in this thesis involve time-dependant free-surface flows, special numerical schemes are required for locating free surface and performing time-integration. We summarize these schemes below.

C.2 Elliptic mesh generation

To track the moving interface, we applied the elliptic mesh generation technique developed by Christodoulou and Scriven [82]. The main advantages of this technique are its high numerical stability and accuracy and the fact that large deformations can be simulated with minimum or even without remeshing cycles [83], compared to other schemes such as the Lagrangian-Eulerian method. In this technique, the moving interface is tracked by solving a set of diffusion equations which map the physical coordinates (x, y) of the mesh onto a square computational domain with coordinates (ξ, η):

$$\boldsymbol{\nabla} \cdot (D_\xi \boldsymbol{\nabla} \xi) = 0, \quad \boldsymbol{\nabla} \cdot (D_\eta \boldsymbol{\nabla} \eta) = 0, \tag{C.5}$$

where D_ξ and D_η are mesh diffusion coefficients used to distribute elements within the physical domain and $\boldsymbol{\nabla}$ is gradient operator taken with respect to the physical

coordinates.

In the computational domain, the velocity, pressure, and position unknowns are expanded in terms of the basis sets $\Phi^i(\xi,\eta)$ and $\Psi^k(\xi,\eta)$:

$$\mathbf{u}(t) = \sum_i \mathbf{u}(t)_i \Phi^i(\xi,\eta), \tag{C.6}$$

$$\mathbf{x}(t) = \sum_i \mathbf{x}(t)_i \Phi^i(\xi,\eta), \tag{C.7}$$

$$\mathrm{p}(t) = \sum_k \mathrm{p}(t)_k \Psi^k(\xi,\eta). \tag{C.8}$$

The computational domain is partitioned by means of quadrilateral elements. Each element contains nine nodes, each having four degrees of freedom (x and y coordinates and velocity in both directions) except for the middle node that presents three additional degrees: the pressure. The corresponding basis functions are nine-node biquadratics for Φ^i (Q_2) and three-node linear discontinuous for Ψ^k (P_{-1}).

C.3 Time integration

Time integration is performed using the second-order adaptive time-stepping algorithm outlined by Gresho *et al.* [84]. In the first three fixed time steps, a first-order Euler forward-difference predictor and a first-order Euler backward-difference corrector are used to alleviate spurious oscillations in the solution; this improves the convergence rate in subsequent simulations [85]. A second-order Adams-Bashforth predictor is used with the trapezoid rule as a corrector in the following time steps to evaluate the local time truncation errors $||d_n||$. This truncation error is utilized to compute the next time step size, via

$$\Delta t_{\mathrm{new}} = \Delta t_{\mathrm{old}} (\epsilon / ||d_n||)^{1/3}, \tag{C.9}$$

where $\epsilon = 10^{-5}$ is the input maximum permissible value of the relative error in a single time step.

With these numerical schemes, we then solve the weak (Galerkin) form of Eqs. (C.1) and (C.5) in the computational domain:

$$\mathbf{R}_M^i = \int_A \Phi^i \left(-\boldsymbol{\nabla} p + \nabla^2 \mathbf{u} - W^2 \mathbf{r} + \mathbf{e}_g\right) dA = 0, \tag{C.10}$$

$$\mathrm{R}_C^k = \int_A \Psi^k \left(\boldsymbol{\nabla} \cdot \mathbf{u}\right) dA = 0, \tag{C.11}$$

$$\mathrm{R}_K^i = \int_{\partial A} \mathbf{n} \cdot (\mathbf{u} - \dot{\mathbf{r}_s}) \Phi^i ds = 0, \tag{C.12}$$

$$\mathrm{R}_\xi^i = \int_A \Phi^i (\boldsymbol{\nabla} \cdot (D_\xi \boldsymbol{\nabla} \xi)) dA = 0, \tag{C.13}$$

$$\mathrm{R}_\eta^i = \int_A \Phi^i (\boldsymbol{\nabla} \cdot (D_\eta \boldsymbol{\nabla} \eta)) dA = 0, \tag{C.14}$$

where M, C, and K denote momentum, continuity, and kinematic residuals; A denotes the computational domain, ∂A its free-surface boundaries.

This equation set is highly nonlinear because the interface is unknown, and we therefore use the Newton-Raphson method to obtain a linear matrix problem of the form:

$$\left(\frac{1}{\Delta t}\mathbf{M} + \mathbf{J}\right)\Big|_{\delta^n} \left(\delta^{n+1} - \delta^n\right) = -\mathbf{R}|_{\delta^n}, \tag{C.15}$$

where δ^n is the solution vector containing the velocity, pressure and position unknowns at the n^{th} iteration in the Newton-Raphson scheme, $\mathbf{R}$ is the residual vector, $\mathbf{J}$ is the Jacobian matrix, and $\mathbf{M}$ is the mass matrix. Gaussian quadrature is used to evaluate all integrals in the assembly of $\mathbf{R}$, $\mathbf{J}$, and $\mathbf{M}$. This iterative process is finished when the norm of the difference between two consecutive residuals is smaller than 10^{-5}. Solving Eq. (C.15) yields coating shape at any given time.

Appendix D

Infinite Marangoni number

In §2 and §3, we assumed dilute concentrations of surfactant such that $\phi/\sigma_m = O(\epsilon)$ ($Ma \sim O(\epsilon)$, see Tables 2.1 and 3.1) to simplify the governing equations. Here, ϕ is the spreading pressure and σ_m is the mean surface tension. In this appendix, we test the validity of this assumption by using the Galerkin finite element scheme described in Appendix C.

The evolution of surfactant concentration at the liquid-air interface is governed by a convection-diffusion equation with the form

$$\Gamma_t + \boldsymbol{\nabla}_s \cdot (\mathbf{u}_s \Gamma) + (\boldsymbol{\nabla}_s \cdot \mathbf{n})\Gamma(\mathbf{n} \cdot \mathbf{u}) = D_s \boldsymbol{\nabla}_s^2 \Gamma, \tag{D.1}$$

where D_s is a surface diffusion coefficient, which is assumed to be a constant, Γ is the surfactant concentration, and $\mathbf{u}_s$ is the surface velocity. This equation is solved simultaneously with Eqs. (C.1) and (C.5) to yield the concentration profile as a function of time. Note that the third term on the left-hand side arises due to surface stretching and it does not appear in the leading-order evolution equation (Eq. (2.49)) in the lubrication model.

We first consider the limiting case where the cylinder is stationary ($W = 0$) and the presence of surfactant has no influence on film evolution ($Ma = 0$). We use this sample problem to show that the surface-stretching term can become significant in regions where large variations in film thickness occur. The rotating-cylinder case with a nonzero Marangoni number will also be discussed.

D.1 Stationary cylinders

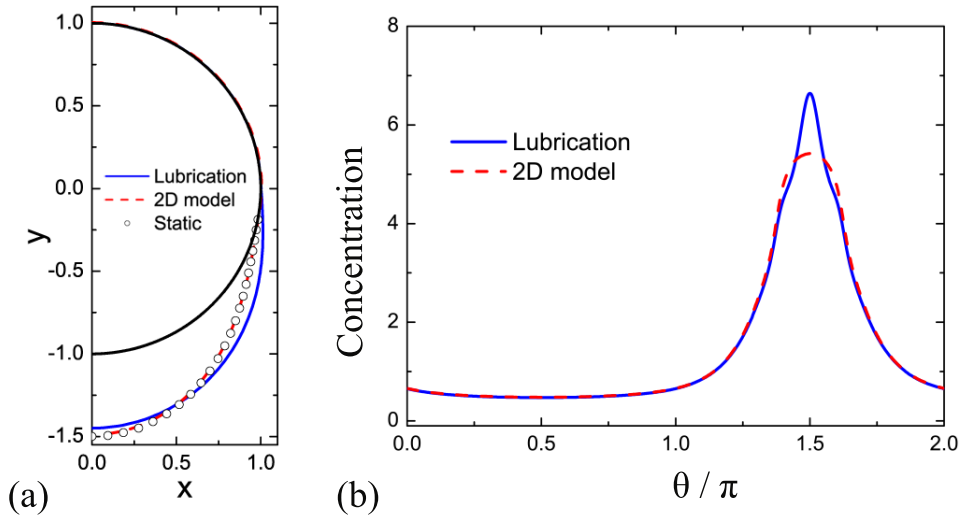

Figure D.1: (a) Free-surface profiles and (b) concentration profiles with $W = 0$, $M = 0.02$, $Bo = 1$, $\Gamma_0 = 1$, $Ma = 0$, $Pe = 10^3$, and $h_0 = 0.1443$. Black solid line in panel (a) indicates cylinder surface.

Consider the hypothetical situation of a static drop hanging beneath a stationary cylinder ($W = 0$), with no variation along the cylinder axis. In the case where $Ma = 0$, the static free-surface profile can be predicted directly by solving the following ODE using a shooting method (see Ref. [10]),

$$r''(\theta) = r\left(1 + 2\left(\frac{r'}{r}\right)^2\right) - r^2(\kappa_0 - R - h_0 - r\sin\theta)\left(1 + \left(\frac{r'}{r}\right)^2\right)^{3/2}, \qquad \text{(D.2)}$$

where κ_0 is curvature at the lowest point of the droplet, R is cylinder radius, and h_0 is initial film thickness.

Following Evans *et al.* [10], we solve the above equation with $R = l_c$ ($Bo = 1$) and $h_0 = 0.1443$. The resulting static drop shape on one side of the cylinder is shown in Fig. D.1a with open circles. In our lubrication model and 2D flow model, a coating with the same initial thickness is allowed to drain until the thickness at the cylinder top is less than $h = 0.0001$. Results are also shown in Fig. D.1 for comparison.

The static solution (open circles in Fig. D.1a) indicates that the maximum film thickness (at the cylinder bottom) is about the same as the cylinder radius, way beyond the thin-film approximation. In this thick-film regime, results of the 2D model (red dashed line) are in good agreement with the static solution, while the lubrication model (blue solid line) underestimates the maximum film thickness. This discrepancy arises due to the simplified curvature used in the lubrication model (see §4).

The corresponding concentration profiles obtained from the 2D model (red dashed line) and the lubrication model (blue solid line) are shown in Fig. D.1b. Due to the initial convective flow, surfactant tends to accumulate at the cylinder bottom, and for this reason, concentration reaches its maximum at $\theta = 1.5\pi$. In the thin-film region (i.e., cylinder top $0 < \theta < \pi$), results from the two mathematical models are in good agreement. In the thick-film region (i.e., cylinder bottom $\pi < \theta < 2\pi$), the lubrication model predicts the existence of a relatively sharp peak at $\theta = 1.5\pi$ (blue solid line in Fig. D.1b), while the 2D model predicts a much smoother concentration peak and a much smaller maximum value (red dashed line in Fig. D.1b). This discrepancy can be explained by noticing that the surface stretching term in Eq. D.1 causes surfactant concentration to decrease in regions where a significant increase in surface area occurs (i.e., cylinder bottom). In the 2D model, this stretching term, together with the diffusion term, balance out the convective term when the drop becomes sufficiently large, leading to a smoother concentration profile relative to that in the lubrication model.

Due to the concentration peak, lubrication model greatly overestimates surfactant-induced Marangoni effects once we set $Ma \neq 0$, which tend to suppress liquid drainage and therefore lead to a smaller pendant drop compared to the 2D model. Results are not shown in this appendix for brevity. For all the cases investigated in §2, the maximum film thickness is always much smaller than the cylinder radius ($h/R = O(\epsilon^2)$), so the stretching term is negligible and no sharp concentration peak is observed in our simulations. We discuss below the validity of the dilute-concentration assumption ($Ma = O(\epsilon)$) in the thin-film regime.

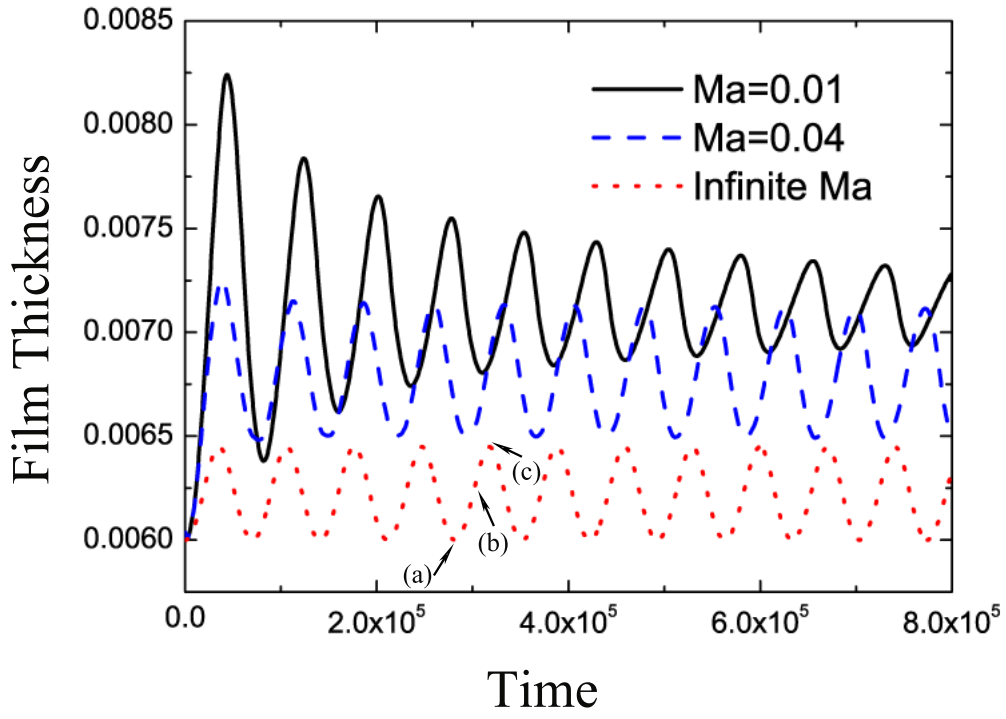

Figure D.2: (a) Time variations of film thickness obtained from the lubrication model at $\theta = 0$ with $W = 0.005$, $M = 0.02$, $Bo = 25$, $\Gamma_0 = 1$, $Pe = 10^6$, and $h_0 = 0.006$. The corresponding schematics of the free-surface profiles at times (a), (b), and (c) are shown in Fig. D.3.

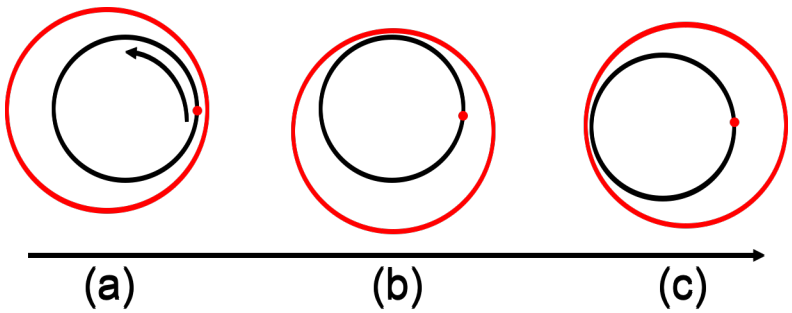

Figure D.3: Schematics of the free-surface profiles at time (a), (b), and (c) marked in Fig. D.2. Red dots indicate the positions of $\theta = 0$.

D.2 Rotating cylinders

§2 illustrates that Marangoni stresses can lead to fast damping of oscillations in the film thickness at relatively short times, but if strong enough can increase the oscillation amplitude at longer times (Fig. 2.10). Such a phenomenon is also shown in Fig. D.2 with a black solid line and a blue dashed line.

To further understand the influence of Marangoni stresses, we consider a limiting case in which $Ma \to \infty$. Dividing Eq. (2.19) by Ma and letting $Ma \to \infty$ results in $\partial\Gamma/\partial\theta = 0$, which indicates that the surfactants are uniformly distributed along the free surface. Substituting this result into Eq. (2.49) yields $u_s = 0$, corresponding to an immobile free surface. Based on this new boundary condition, we are able to solve for a new evolution equation for the film thickness,

$$\frac{\partial h}{\partial t} = -MW\frac{\partial h}{\partial \theta} + \frac{\partial}{\partial \theta}\left(\frac{h^3}{3}\cos\theta\right) - \frac{\partial}{\partial \theta}\left[\frac{h^3}{12Bo}\frac{\partial}{\partial \theta}(h + \frac{\partial^2 h}{\partial^2 \theta}) + \frac{h^3}{12}(W^2 - \sin\theta)\frac{\partial h}{\partial \theta}\right]. \tag{D.3}$$

The time-variation of the film thickness obtained by solving the above equation is shown in Fig. D.2 with a red dotted line. We also show in Fig. D.3 the schematics of the free-surface profiles at three times (marked (a)-(c) in Fig. D.2) to gain insight into the coating behavior. Since the film-thickness variation at a fixed point is small relative to the thickness of the film, schematics rather than actual free-surface profiles are shown for ease of visualization.

In the case where $Ma \to \infty$, we observed a "hula-hoop" type behavior, in which the coating rotates around the cylinder like a "hula hoop" with almost no deformation from its initial shape (Fig. D.3) and the resulting oscillation in film thickness never decay or grow (red dotted line in Fig. D.2) as cylinder rotates. This "hula-hoop" behavior arises due to the immobile-free-surface boundary condition ($u_s = 0$), since strong Marangoni stresses greatly hinder the deformation of the free surface.

We then test the validity of the phenomena shown in Fig. D.2 using our 2D model. Since Ma cannot be set as $+\infty$ in this model, we pick $Ma = 0.1$ instead. This is already the maximum value we can investigate due to the computational limit, since larger Ma corresponds to higher oscillation frequency (Fig. D.2) and thus smaller time steps. Results obtained from the 2D model and the lubrication model for $Ma = 0.0048$ (used in §2) and $Ma = 0.1$ are shown in Fig. D.4 for comparison.

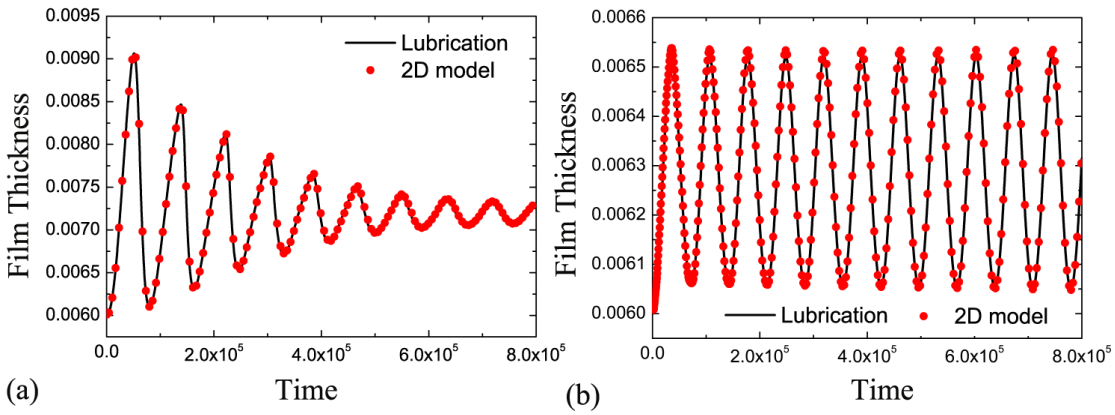

Figure D.4: Time variation of film thickness obtained at $\theta = 0$ with $W = 0.005$, $M = 0.02$, $Bo = 25$, $\Gamma_0 = 1$, $Pe = 10^6$, $h_0 = 0.006$, and (a) $Ma = 0.0048$ and (b) $Ma = 0.1$.

Figs. D.4a and D.4b illustrate that these two models are in good agreement even when the value of Ma is far beyond our assumption that $Ma = O(\epsilon)$. Furthermore, the 2D model also predicts the existence of a "hula-hoop" type behavior when Ma is sufficiently large (Fig. D.4b). Results from both the rotating-cylinder case and the stationary-cylinder case (Fig. D.1) indicate that the lubrication model can still be valid for $Ma = O(100\epsilon)$ provided that surface stretching is not significant during the evolution of the coating.

We also briefly investigated surfactant-induced Marangoni effects in both the elliptical-cylinder case and the topographically-patterned case by using our finite element scheme for the parameter regime where gravitational forces play an important role. We briefly summarize our observations. For both cases, surface-tension forces tend to drive liquid away from the high-curvature regions, leading to a significant decrease in film thickness over the pattern crests (Fig. 4.13) or the cylinder tips (Fig. 5.7). Since these high-curvature regions also appear to be the low-concentration regions, the resulting Marangoni stresses tend to draw liquid back, and thus give rise to a more uniform liquid distribution around a rotating cylinder with complex surface geometry relative to the surfactant-free case. Surfactant-induced Marangoni effects should be further explored in the context of film drying. As the film dries, viscous forces increase in magnitude and

weaken the effects of Marangoni forces. However, if the Marangoni forces are strong enough at early times, they could still be beneficial for producing a more uniform liquid distribution.